

Spring 4-2016

## A Hybrid Vortex Solution for Surge Margin Enhancement in Axial Compressors

Daniel Port  
*Embry-Riddle Aeronautical University*

Follow this and additional works at: <https://commons.erau.edu/edt>



Part of the [Aerospace Engineering Commons](#)

---

### Scholarly Commons Citation

Port, Daniel, "A Hybrid Vortex Solution for Surge Margin Enhancement in Axial Compressors" (2016).  
*Doctoral Dissertations and Master's Theses*. 233.  
<https://commons.erau.edu/edt/233>

This Thesis - Open Access is brought to you for free and open access by Scholarly Commons. It has been accepted for inclusion in Doctoral Dissertations and Master's Theses by an authorized administrator of Scholarly Commons. For more information, please contact [commons@erau.edu](mailto:commons@erau.edu).

A HYBRID VORTEX SOLUTION FOR SURGE MARGIN  
ENHANCEMENT IN AXIAL COMPRESSORS

A Thesis

Submitted to the Faculty

of

Embry-Riddle Aeronautical University

by

Daniel Port

In Partial Fulfillment of the

Requirements for the Degree

of

Master of Science in Aerospace Engineering

April 2016

Embry-Riddle Aeronautical University

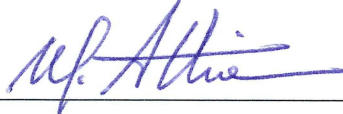
Daytona Beach, Florida

A HYBRID VORTEX SOLUTION FOR SURGE MARGIN ENHANCEMENT IN  
AXIAL COMPRESSORS

by  
Daniel Port

A Thesis prepared under the direction of the candidate's committee chairman, Dr. Magdy Attia, Department of Aerospace Engineering, and has been approved by the members of the thesis committee. It was submitted to the School of Graduate Studies and Research and was accepted in partial fulfillment of the requirements for the degree of Master of Science in Aerospace Engineering.

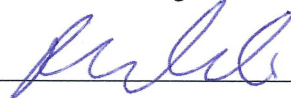
THESIS COMMITTEE



Chairman, Dr. Magdy Attia



Member, Dr. William Engblom



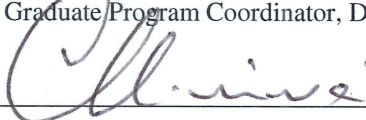
Member, Dr. Reda Mankbadi



Department Chair, Dr. Anastasios Lyrintzis  
or Graduate Program Coordinator, Dr. Eric Perrell

5 Apr 2016

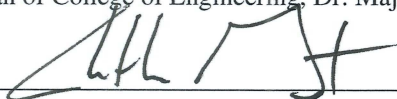
Date



Dean of College of Engineering, Dr. Maj Mirmirani

04/06/16

Date



Vice Chancellor, Academic Support, Dr. Christopher Grant

4/5/16

Date

## ACKNOWLEDGMENTS

I would like to express my appreciation to my advisor, Dr. Magdy Attia, for his guidance and support throughout this thesis. The knowledge I have gained from Dr. Attia's classes and personal discussions has proven invaluable. Without his influence and advice, I would not have pursued my Master's degree and for that, I cannot thank him enough.

None of my education would have been possible without the love and support of my parents who have been by my side (although halfway across the world) through every moment in my college career. Through every positive moment and especially through the many lows experienced throughout my degrees, they were always there to get me through each hurdle and ensure my success. For that support, I will never be able to repay them enough.

I would like to also extend my greatest appreciation to my fellow colleagues in the Gas Turbine Lab who have always been there through the late nights in the lab to participate in discussions and lighten the mood during stressful times. To Darrell Stevens, for his incomprehensible bank of knowledge that has been a regular resource to me through my thesis and regular classwork. I would like to specifically thank Alex Rozendaal for his never-ending help and expertise in CFD. Without his guidance and frequent discussions, my understanding of CFD would not be half of what it is today.

Finally, I would like to acknowledge and thank my grandfather, Geoff, who ignited the spark of aviation within me at the age of 13. Since then, he has helped that spark grow into the passion that drives me every day. Without him, I would not be where I am today.

## TABLE OF CONTENTS

LIST OF TABLES .....	vi
LIST OF FIGURES .....	vii
NOMENCLATURE .....	x
ABSTRACT.....	xiii
1. Introduction.....	1
1.1. Axial Compressor Design Methodologies.....	3
1.1.1. Preliminary Design.....	4
1.1.2. Throughflow .....	4
1.1.3. 2D Blade Design.....	5
1.1.4. 3D Blade Design.....	7
1.2. Current Design Stalemate .....	8
1.3. Compressor Stall/Surge.....	9
1.3.1. Compressor Map .....	10
1.4. Problem Statement .....	12
2. Literature Survey .....	13
2.1. Radial Equilibrium .....	13
2.2. Simple Radial Equilibrium Equation .....	14
2.3. Improvements Following the SREE .....	16
2.4. Modifications to the SREE .....	17
3. Hybrid Vortex Concept and Derivation .....	18
3.1. Concept .....	18
3.2. Equation Derivation .....	20
3.3. Hybrid Vortex Implementation .....	21
4. Blade Design and Methodology .....	23
4.1. Meanline Design.....	23
4.1.1. Hybrid Vortex Design Cases .....	24
4.2. 2D Design and CFD .....	25
4.2.1. 2D Meshing and Independency .....	27
4.3. 3D Design and CFD .....	29
4.3.1. 3D Meshing .....	29
4.3.2. Simulation Setup .....	32
5. Results.....	34
5.1. Baseline Case – Free Vortex.....	34
5.1.1. Meanline.....	34
5.1.2. 2D Design .....	35
5.1.3. 3D Performance and Observations.....	37
5.2. Hybrid Vortex 2D Design Loop.....	40
5.2.1. Meanline Design.....	42

5.2.2.	Airfoil Design .....	44
5.3.	Hybrid Vortex 3D Design Loop.....	48
5.3.1.	Final Hybrid Vortex Case Selection.....	48
5.3.2.	Axial Velocity Convergence Loop.....	50
5.3.3.	3D Blade Optimization .....	55
5.4.	Observed Flow Features .....	59
5.4.1.	Off-Design Behavior .....	62
6.	Conclusion .....	67
7.	Recommendations.....	69
	REFERENCES .....	71
A.	Radial Equilibrium Derivations .....	73
B.	Hybrid Vortex Derivation.....	76
C.	Meanline Aerodynamics .....	78
D.	Free Vortex Geometric Trends .....	80
E.	NASA GRAPE Sample Input.....	81
F.	NASA RVCQ3D Sample Input.....	82
G.	2D Blade Design.....	83
H.	Sample CFX® Inlet Velocity Profile File .....	88
I.	3D Meshing and Independency .....	89
J.	Hybrid Vortex 3D Design.....	91
K.	BladeGen™-to-RVCQ3D flow automation .....	92
L.	CFX® Definition File Generation Code.....	95

## LIST OF TABLES

Table 4.1 Meanline design choices .....	23
Table 4.2 Hybrid Vortex TE design cases. ....	24
Table 4.3 2D mesh independence total node count. ....	27
Table 4.4 Mesh sizing for independent study .....	31
Table 4.5 Convergence criteria. ....	33
Table 5.1 Aerodynamic health properties of baseline blade. ....	34
Table 5.2 Baseline performance parameters. ....	37
Table 5.3 Final design point values for all 2D design cases. ....	46
Table 5.4 Final performance parameters of optimized HV blade. ....	58
Table 5.5 Relative metal and flow angles at the TE, 2% span. ....	62
Table 5.6 Mass flow operating range comparison between the FV and HV blades. ....	63
Table 5.7 Hypothetical Surge Margin comparison. ....	65
Table A.1 Vortex solutions (Horlock, 1958) .....	75

## LIST OF FIGURES

Figure 1.1 Gas turbine components (Altuntas, 2014).....	1
Figure 1.2 Compressor design stages (Molinari & Dawes, 2006).....	3
Figure 1.3 Stream surfaces through cascade (Wu C.-H. , 1952). ....	5
Figure 1.4 Typical compressor cascade displaying some design parameters.....	6
Figure 1.5 Example of a modern transonic fan showing 3D features (Rolls-Royce plc, 2014). ....	8
Figure 1.6 Basic compressor map features. ....	11
Figure 1.7 Compressor maps comparing soft (a) and hard (b) characteristic slopes.....	12
Figure 2.1 Radial equilibrium conditions at the entry and exit of the blade row (Dixon & Hall, 2010). ....	13
Figure 2.2 Fluid element (Dixon & Hall, 2010). ....	14
Figure 3.1 Resulting composite boundary layer (Coles, 1969). ....	18
Figure 3.2 Design vs. actual axial velocity distribution.....	19
Figure 3.3 Free Vortex design flowchart.....	21
Figure 3.4 Hybrid Vortex design process flowchart.....	22
Figure 4.1 Meridional view of compressor annulus. ....	24
Figure 4.2 Ideal (a) and achieved (b) Mach profile for a compressor blade.....	26
Figure 4.3 2D mesh independence study results.....	28
Figure 4.4 Sample of the final mesh at 25% span.....	28
Figure 4.5 Free Vortex airfoil sections stacked to form the 3D blade.....	29
Figure 4.6 Topology sample displaying the final refined mesh.....	30
Figure 4.7 Final medium mesh with LE refinement magnified.....	31
Figure 5.1 Comparison between circular (a) and elliptic (b) LE design at 25% span. ....	35
Figure 5.2 LE Mach spike comparison of circular (a) and elliptic (b) LE at 25% span...	36
Figure 5.3 2D airfoil sections of the Free Vortex stacked on their centroids. ....	37
Figure 5.4 Velocity streamlines (a) and contour (b) of the LE at 2% span for the FV blade.....	38
Figure 5.5 Pressure contour at 50% span.....	39
Figure 5.6 Hub streamlines of the Free Vortex blade at the design point. ....	39
Figure 5.7 Hybrid Vortex equation fitting for the LE.....	40
Figure 5.8 Hybrid Vortex equation fitting for the TE.....	41



Figure 5.9 Circumferential velocity profiles for the LE (a) and TE (b). .....	41
Figure 5.10 Velocity triangle comparison at 2% span for the LE (a) and TE (b).....	42
Figure 5.11 LE relative flow angle comparison between the FV and HV blades. ....	43
Figure 5.12 TE relative flow angle comparison between the FV and HV blades. ....	43
Figure 5.13 Normalized Mach distribution for all four designs at the 50% span. ....	45
Figure 5.14 Airfoil sections of all four design cases at 2% span.....	47
Figure 5.15 Airfoil sections of all four design cases at 25% span.....	47
Figure 5.16 Axial velocity distributions at TE following 2D design.....	49
Figure 5.17 Turbulent kinetic energy distribution along the blade span. ....	50
Figure 5.18 Initial axial velocity distribution from 2D design. ....	51
Figure 5.19 Impact of stagger variation at 2% span. ....	52
Figure 5.20 Axial velocity distribution of the closest three iterations.....	53
Figure 5.21 Isosurface at $M_r = 1.0$ for design iteration ‘p’ .....	54
Figure 5.22 P-Mass residual monitor.....	55
Figure 5.23 LE incidence comparison before (a) and after (b) 3D design at 25% span..	56
Figure 5.24 Redesigned HV airfoil section at 25% span.....	56
Figure 5.25 LE incidence comparison before (a) and after (b) 3D design at 50% span..	57
Figure 5.26 Redesigned HV airfoil section at 50% span.....	57
Figure 5.27 Turbulent kinetic energy trends at the TE before and after optimization.....	58
Figure 5.28 Hub streamlines observed from the TE of the HV blade. ....	59
Figure 5.29 Surface streamlines on the hub, suction surface of the FV (a) and HV (b)...	60
Figure 5.30 Radial velocity comparison at the TE of the HV and baseline blades. ....	61
Figure 5.31 Design rotor speed characteristics for the FV and HV blades.....	62
Figure 5.32 Isentropic efficiency for the FV and HV blades.....	63
Figure 5.33 Hypothetical Hybrid Vortex characteristic following redesign.....	64
Figure G.1 Mach distribution for 2% span, all four designs.....	83
Figure G.2 Mach distribution for 25% span, all four designs.....	83
Figure G.3 Mach distribution for 75% span, all four designs.....	84
Figure G.4 Mach distribution for 98% span, all four designs.....	84
Figure G.5 Airfoil sections at 50% span.....	85
Figure G.6 Airfoil sections at 75% span.....	86
Figure G.7 Airfoil sections at 98% span.....	86
Figure G.8 Hybrid Vortex 2D sections on their stacking lines for design Case #1 (a), #2	

(b), and #3 (c).....	87
Figure I.1 Tip gap refinement for the medium mesh (2.5M elements).....	89
Figure I.2 Y+ contour of the medium mesh (2.5M elements). ....	89
Figure I.3 Sample of mesh refinements used for independence study. ....	90
Figure J.1 Airfoil comparison between the 2D and 3D designed Hybrid Vortex blades. ....	91

## NOMENCLATURE

### Acronyms

2D	Two-Dimensional
3D	Three-Dimensional
CFD	Computational Fluid Dynamics
CPU	Central Processing Unit
DCA	Double Circular Arc
DF	Diffusion Factor
DH	DeHaller Number
FV	Free Vortex
GRAPE	GRids about Airfoils using Poisson's Equation
H/T	Hub-to-Tip Ratio
HV	Hybrid Vortex
I/O	Input/Output
KE	Kinetic Energy
LE	Leading Edge
NACA	National Advisory Committee for Aeronautics
NASA	National Aeronautics and Space Administration
NoB	Number of Blades
RM	Reattachment Modification
RPM	Revolutions Per Minute
RVCQ3D	Rotor Viscous Quasi-3D
SM	Surge Margin
SREE	Simple Radial Equilibrium Equation
SST	Shear-Stress-Transport
T.M.	Turbomachinery
TE	Trailing Edge

## Subscripts and Superscripts

0	Total/Stagnation Conditions
choke	Choke Point
corr	Corrected
design	Design Point
FV	Free Vortex
h	Hub
HV	Hybrid Vortex
LE	Leading Edge
m	Mean/Mid Span
max	Maximum
op	Operating range
r	Relative
surge	Surge Point
t	Tip
TE	Trailing Edge
tt	Total-to-Total
u	Tangential/Circumferential
z	Axial direction

## Units and Variables

°C	Degrees Celsius
°F	Degrees Fahrenheit
c	Chord
ft	foot
i	Incidence
kg	Kilogram
m	Meter
M	Mach number
P	Pressure
Pa	Pascal
r	Radius
s	Second
S	Pitch
t	Thickness
U	Tangential /Circumferential velocity
V	Absolute velocity
W	Relative velocity
x	Distance

## Greek Letters

$\alpha$	Absolute Flow Angle
$\beta$	Relative Flow Angle
$\gamma$	Specific Heat Ratio
$\Delta$	Change
$\sigma$	Solidity
$\sigma_s$	Stagger
$\delta$	deviation
$\eta$	Efficiency
$\pi$	Pressure Ratio
$\rho$	Density
$\Phi$	Flow Coefficient
$\lambda$	Work Coefficient

## ABSTRACT

**Author:** Daniel F. Port

**Title:** A Hybrid Vortex Solution for Surge Margin Enhancement in Axial Compressors

**Institution:** Embry-Riddle Aeronautical University, Daytona Beach

**Degree:** Master of Science in Aerospace Engineering

**Date:** March, 2016

A new vortex solution to the Simple Radial Equilibrium Equation (SREE) is presented that incorporates endwall effects into the preliminary design stage of a single stage, low pressure compressor with a hub-to-tip ratio of 0.4 and non-axial inlet flow. This vortex solution is proposed to overcome the rapidly approaching asymptotic peak in compressor performance in the industry today. The Hybrid Vortex theory incorporates a versatile, higher-order solution to the SREE, resulting in more accurate preliminary designs requiring less manipulation in the final design stages. This new solution results in significant changes in hub geometry with the stagger of the hub changing up to  $20^\circ$ . A numerical study was conducted, evaluating the new Hybrid Vortex method in comparison to the well-known Free Vortex design method. The study revealed the Hybrid Vortex solution not only shows improved flow features at the hub, but has great potential for increasing the surge margin of a compressor. It also demonstrated an 11% increase in the mass flow operational range over that of the baseline blade during off-design conditions.

## 1. Introduction

Gas turbines have existed in concept since 1791 when the first patent for a gas turbine engine was filed by John Barber (even though his design was never built). Two decades after the first successful powered flight, Sir Frank Whittle in England and Dr. Hans von Ohain in Germany led design groups seeking to implement gas turbine engines as jet propulsion systems in aircraft. Von Ohain was the first of the two to successfully equip and fly a jet-powered aircraft in August, 1939 (Ward, 2010). Since these early aircraft jet engines, the overall layout has remained the same with the basic components shown in Figure 1.1.

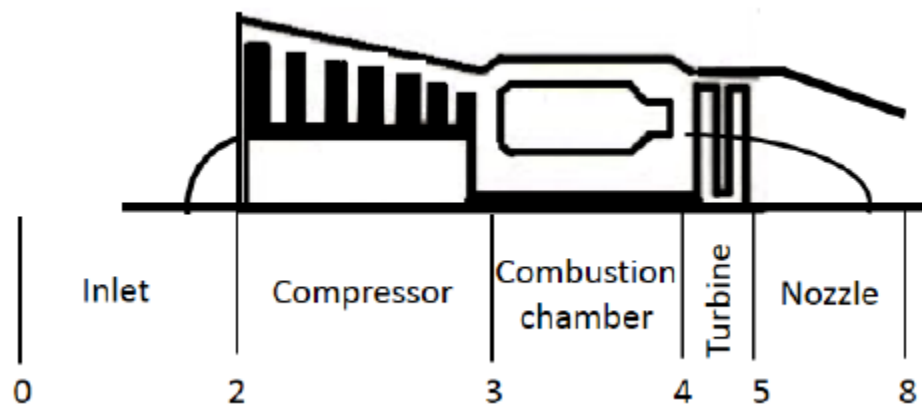


Figure 1.1 Gas turbine components (Altuntas, 2014).

Of these components, the most aerodynamically challenging is the compressor. The complicated flow conditions through the compressor are still not fully understood by designers. With an adverse pressure gradient, secondary flows, viscous effects and tip leakages, flow separation on the airfoil surfaces is a common occurrence during operation. These complicated flow features are nearly impossible to accurately model during the design phase, requiring simplifications and assumptions of the flow physics to be made

(Gallimore, 1999).

The compressor type depicted in Figure 1.1 is an axial compressor. This is the most common compressor type found in modern aircraft engines due to its ability to handle large mass flows. Centrifugal compressors, where the resulting flow is travelling radially outwards away from the rotating axis of the engine, are considerably more bulky. The flow through an axial compressor faces large adverse pressure gradients where the low-pressure flow from the inlet is compressed through successive stages and pushed through the engine into the combustion chamber. This adverse pressure gradient induces flow instabilities that highly influence flow separation, leading to compressor stall or surge. Due to these limitations, each stage of an axial compressor is restricted to small pressure ratios, requiring many stages to obtain the required overall pressure ratio for the cycle.

The demand for higher performance and greater efficiency has increased dramatically over the past few decades, especially in the commercial airline market with fuel demanding nearly 20% of an airliner's operating cost (Smallen, 2015). The demand for higher fuel efficiency has led to many innovative design solutions within the gas turbine industry. From radical engine architecture changes such as the Unducted Fan, to weight saving attempts through advanced material research, engine manufacturers have continued to push the limits of engine efficiency.

To decrease weight and cost of manufacturing, compressors have seen a steady rise in stage loading in order to reduce the total number of stages. As a consequence, the operational envelope of the compressor becomes more restricted, reducing the safety margin between normal operation and compressor stall/surge. How exactly this occurs will be discussed later in this report.



## 1.1. Axial Compressor Design Methodologies

Axial compressor design methods have evolved through many phases since their inception, with exponential advancements made since the introduction of computational design and analysis programs. Early developments in compressor design relied heavily on empirical test data to correlate the theoretical 2D and 3D designs to the experimental resulting flow through the compressors (Molinari & Dawes, 2006). Theoretical and experimental data began to correlate more closely following improvements in cascade theory, wind tunnel design and measurement methods, which helped designers better comprehend the physics of complex fluid flow through turbomachinery.

The introduction of computers into the design process during the 1960's allowed more sophisticated theories to be used in the design process, accounting for basic viscosity and boundary layer effects. These improvements led in turn to throughflow design, first proposed by Wu (1952). Following the advent of computer aided design, the design process became heavily reliant on computer based design tools. These design tools are still the main method of design today with constant improvements in computational power and Computational Fluid Dynamics (CFD) programs being made. However, CFD programs are used exclusively as analysis programs, requiring other methods to obtain the initial compressor geometry (Molinari & Dawes, 2006).

There are still a plethora of methodologies of how to approach compressor design. A simplification of the full design method was discussed by Gallimore (1999) and summarized by Molinari & Dawes (2006) where the process was broken into four steps.

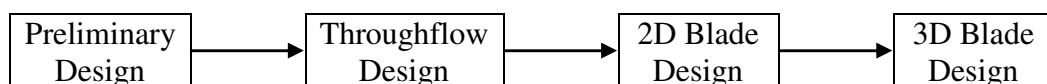


Figure 1.2 Compressor design stages (Molinari & Dawes, 2006).

### **1.1.1. Preliminary Design**

Preliminary design is commonly agreed upon as being the most significant point in the overall design cycle. Preliminary design is where the largest changes in the overall compressor architecture take place. It is where the main requirements for the overall compressor size, shape and stage loadings are set. At this point in the design, the flow is considered to be steady, inviscid, and one-dimensional, with designers using correlations from past compressors to account for losses due to viscous effects (Gallimore, 1999). Preliminary design is conducted through meanline design where flow parameters are calculated at the mean radius using averaged thermodynamic conditions at the inlet and exit of each blade row. This assumption simplifies the calculation of flow conditions and performance characteristics to drastically reduce the complexity of the design problem.

The overall compressor geometry and aerodynamic coefficients are set at this point in the design (these will change slightly later in the design process). Important characteristics such as the loading per stage, annulus shape and overall number of stages are all decided upon based on past experience and compressor knowledge. It is also at this point that simplified off-design performance can be calculated to obtain a basic operating envelope for the compressor.

### **1.1.2. Throughflow**

Throughflow takes the design process into a quasi-3D analysis with steady, axisymmetric flow. This method was first proposed by Wu (1952) where flow through a cascade was simplified into two stream surfaces: one in the blade-to-blade (S1) direction, and the other in the hub-tip (S2) direction (Oates, 1988). These are shown in Figure 1.3.

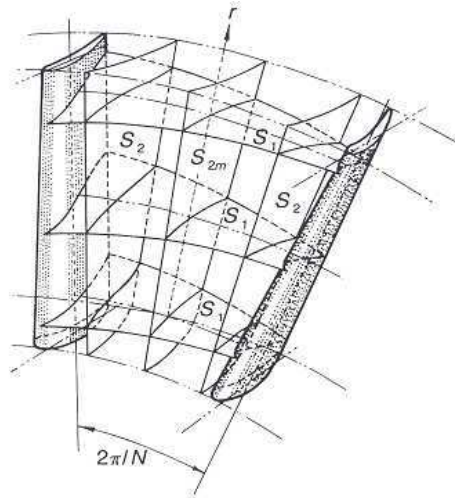


Figure 1.3 Stream surfaces through cascade (Wu C.-H. , 1952).

Throughflow adds the radial dimension to the design process by including the effects of radial variations of the streamlines in the calculations. Radial variations are not captured by the simple radial equilibrium used in the preliminary phase and accounting for these variations can lead to significant changes in the flow conditions entering and exiting the cascade.

Throughflow design is an iterative process where the momentum equations are solved along each streamline using the Streamline Curvature method until a solution has converged on the mass-flow for that streamtube (Wilson & Korakianitis, 1998). The output of a converged Throughflow design is the boundary conditions necessary to conduct blade design along stream sections.

### 1.1.3. 2D Blade Design

The second stage of design, Throughflow analysis, obtains the desired flow angles and velocities to achieve the duty required of the compressor. The next step is to incorporate actual airfoils into the cascade to achieve these air angles and velocities. 2D

blade design takes into account different design parameters, along with certain losses, to properly fit a blade into the passage to achieve the desired flow. General airfoil design, thickness profiles, LE and TE radii, incidence, deviation and boundary layer growth are some of these parameters (Wilson & Korakianitis, 1998). Depending on the flow conditions (subsonic or transonic) the airfoil design can range from the early NACA 65-series blades, to Double Circular Arc (DCA) profiles (Gallimore, 1999). More recently, airfoil shapes are automatically generated from blade-to-blade design optimization programs that conduct the design of the airfoil based on the requirements set by the designer, leading to an airfoil specifically customized and optimized for the job.

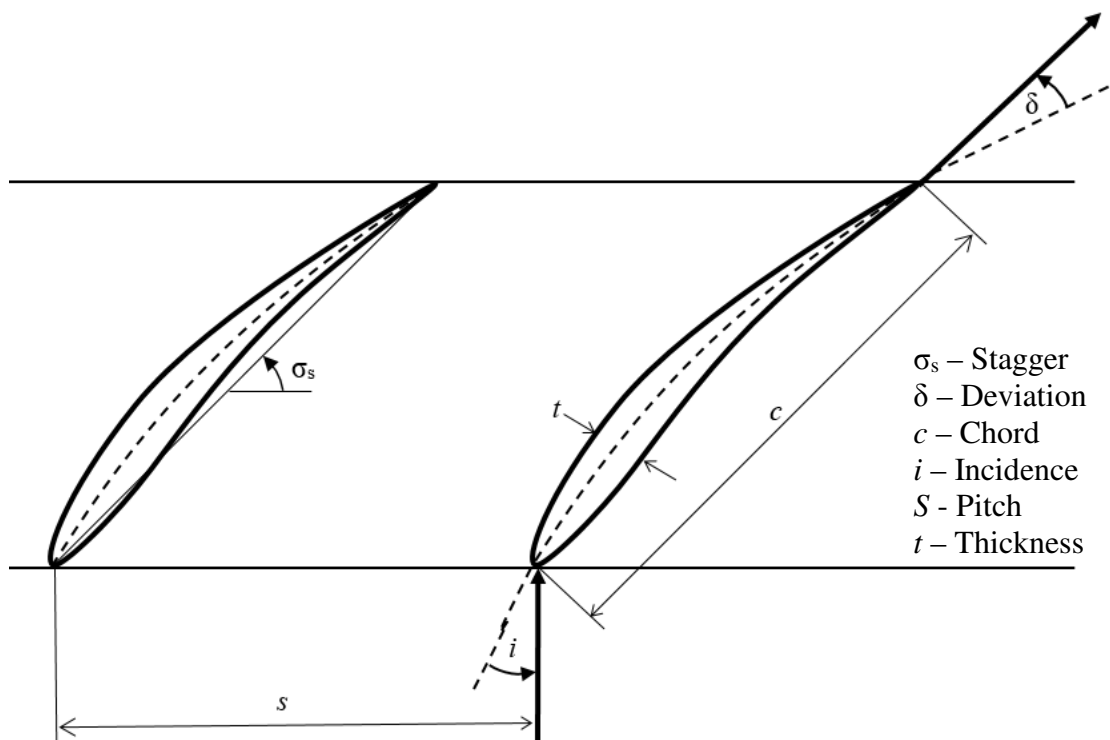


Figure 1.4 Typical compressor cascade displaying some design parameters.

Based on experience, designers can specify an incidence trend for the blade to increase the efficiency of the blade and increase the surge margin. For example, introducing

slight negative incidence in areas such as the tip and hub of the blade can aid in increasing the operating range of the compressor.

Once the airfoil sections are designed for the selected streamlines, the airfoils are stacked to generate the 3D blade shape. Due to the fact that this is still a 2D process that does not include full endwall effects, the blade must then be taken into the final step of the design process.

#### **1.1.4. 3D Blade Design**

This stage of the process is considered more of an analysis stage of the compressor. Modern CFD programs make it possible for designers to examine the 3D flow through a blade channel and witness the unique flow characteristics of problems such as hub corner stall (Hah & Loellbach, 1999). Understanding 3D flow characteristics has led to many advancements in compressor design, introducing new 3D design features such as Bow and Sweep (Gallimore, 1999). It has been these types of advancements that have led to the unique blade shapes seen predominantly on modern, high-bypass fan blades where the tip of the blade is curved in a manner to manipulate shocks formed at the transonic tips to obtain higher efficiency and pressure ratio.



Figure 1.5 Example of a modern transonic fan showing 3D features (Rolls-Royce plc, 2014).

With computational power increasing year to year, the possibilities to incorporate effective optimization programs that can efficiently optimize a complete 3D compressor are getting closer and closer.

Influences on flow stability, such as those due to tip gaps, bleeds and fillets (to name just a few), can now be introduced into the design to examine the effects they have on the flow. These geometric features have varying degrees to which they influence the flow field through the compressor (Gallimore, 1999) and should ideally be accounted for during the design process.

## **1.2. Current Design Stalemate**

There are three different approaches a designer can take when preparing to design a compressor, each with its own strengths and weaknesses. These are summarized by Molinari and Dawes (2006) as: design-by-analysis, design optimization, and design-by-sensitivity. Due to the large timeframe associated with designing from scratch, the trend in

the industry has been more of a design by optimization method. By taking components that are known and tested, the engineer can focus on optimizing the component to increase its efficiency and overall performance. This method has proven very successful in the past, but is leading the industry to a virtual “asymptote of the technology development in turbomachinery design” (Molinari & Dawes, 2006). As with all things, compressor blades can only be optimized so much.

Thus, Molinari and Dawes (2006) suggested that in order to achieve increased efficiency while maintaining performance, the future designer will have to revisit the fundamental building blocks of compressor design and investigate the application of new design methods to preliminary design.

Advancements in computational power and CFD programs have allowed more rapid design iterations for investigating new preliminary design methods. By incorporating simplified 3D effects into this early design phase, more accurate initial designs can be made that reduce the iterative optimization required in the later stages of design. With the computational cost of running full transient 3D simulations so high, any decrease in the required iterations will result in large time savings, allowing for a more efficient design process.

### **1.3. Compressor Stall/Surge**

It has been mentioned that the increase in demand has reduced the operating envelope of the compressor, but how is that determined? An aircraft experiences many different conditions during its flight regime from take-off in hot, dry deserts to cruising at 12,200 m (40,000 ft) where temperatures are down to  $-57^{\circ}\text{C}$  ( $-70^{\circ}\text{F}$ ). These constantly changing operating conditions require aero engines to have the ability to operate across all

possible conditions.

The limits of operation in the compressor are categorized by two extremes, stall or surge, and choking. Choking can be simply defined as the limit of massflow that the compressor can 'swallow' and is rarely a serious concern during operation. Choking usually occurs in the turbine first, stopping the compressor from reaching its choking point. However, surge is quite the opposite and is one of the key limiting factors during axial compressor design.

Surge is an aerodynamic instability that occurs in compressors that can be characterized by a total breakdown of steady flow through the compressor stage, or stages (Horlock, 1958). This phenomenon produces oscillations in the mass flow through the compressor that can lead to flow reversal and mechanical failures due to deformations caused by the sudden changes in flow momentum. Surge is preceded by a more docile flow disturbance called stall, which manifests itself as a classical suction surface flow separation. Stall can occur in one or more cells in the compressor cascade, and can propagate from one cell to the next in what is referred to as 'rotating stall'. Both cases can occur with the compressor still operable until the stall becomes severe enough to eventuate in surge.

### **1.3.1. Compressor Map**

The general behavior of a compressor can be determined from its compressor map. A compressor map has a number of different features as seen in Figure 1.6 and is a plot of the compressor's performance at varying total pressure ratios (vertical axis) and corrected mass flow rates (horizontal axis).



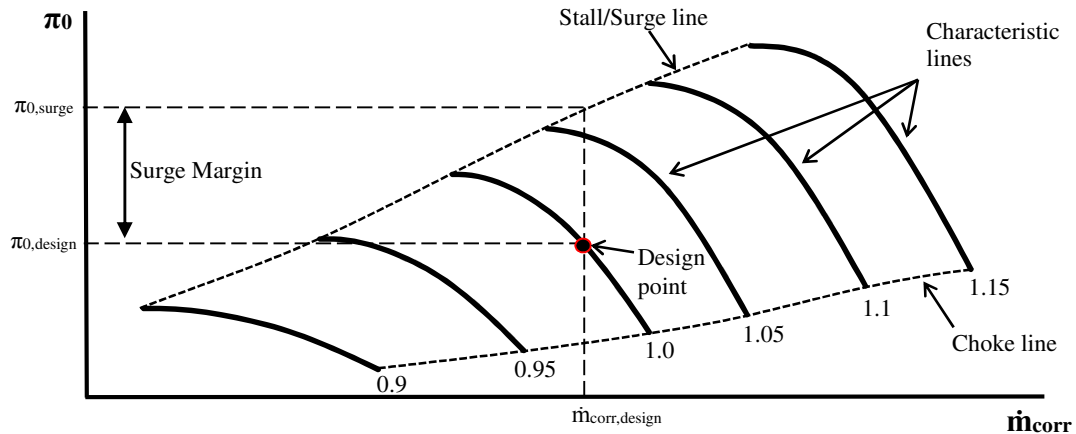


Figure 1.6 Basic compressor map features.

The Characteristic lines show trends of constant rotor speed, normalized to the design rotor speed. The other two important lines shown in this figure are the stall/surge and choking lines and display the trend of these two phenomena, discussed previously, at the different operating conditions. Although a compressor can operate in the stalled region, the limit is usually specified as the point at which the characteristic slope reaches zero (Hill & Peterson, 1992).

The term most commonly used for specifying how far away from surge a compressor is operating is called its Surge Margin (SM). Surge Margin is defined by the equation  $SM = \frac{\pi_{0,surge} - \pi_{0,operating}}{\pi_{0,operating}} \times 100$  where  $\pi_{0,surge}$  is the pressure ratio that lies on the surge line vertically above the operating point as seen in the above figure. A typical surge margin of an axial compressor lies between 10-15 percent and higher (Brun & Kurz, 2005).

The slope of the characteristics can determine the operating limits of the compressor. As seen in (a) of Figure 1.7, the soft slope of the characteristic gives the compressor a wide operating range across the mass flow. In comparison, the hard slope of (b) severely restricts the mass flow operating range of the compressor. This can lead to low surge margins requiring multiple stages to distribute the loading of the compressor. A

compressor having a larger number of stages will operate on a ‘harder’ map.

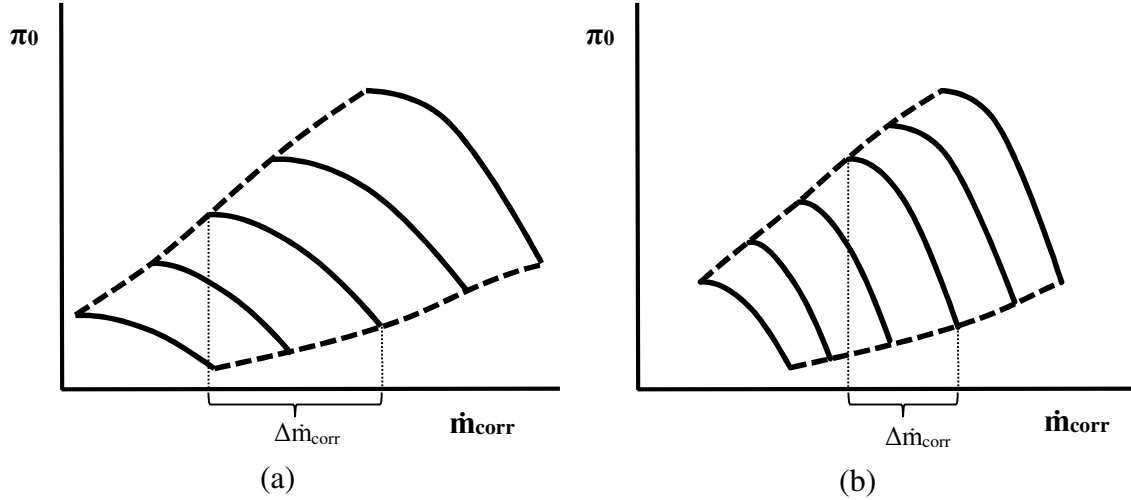


Figure 1.7 Compressor maps comparing soft (a) and hard (b) characteristic slopes.

The sharp slope of the characteristic coincides with an increase in compressor performance as demanded by modern compressors, but at the cost of valuable surge margin.

#### 1.4. Problem Statement

With the current demand for ultra-high efficiency engines at an all-time high, a solution to the asymptotic stalemate in compressor design is required. Modern compressors have gone through many cycles of optimization and have nearly reached their limits in overall performance and efficiency.

As suggested by Molinari and Dawes (2006), the preliminary design phase of compressors will be revisited for a solution to this issue. By reinvestigating the vortex solutions and applying modern computing capability, a study will be conducted on the effects on both the geometry and overall performance of an axial compressor in an effort to provide an innovative method for enhancing its surge margin.

## 2. Literature Survey

### 2.1. Radial Equilibrium

One of the largest improvements made early in axial compressor design was the implementation of radial equilibrium. Radial equilibrium governs the radial flow through turbomachinery where the radial equation of motion is applied to define a pressure gradient to counteract the centrifugal force seen through rotating turbomachinery (Wu & Wolfenstein, 1950). The pressure gradient imposed on the flow becomes the restoring force to maintain the smooth flow of fluid through the blade row. This pressure gradient is specified so that the flow entering and exiting the blade row is considered to have zero radial velocity, meaning that any radial imbalances within the cascade are resolved by the trailing edge of the blade as seen in Figure 2.1.

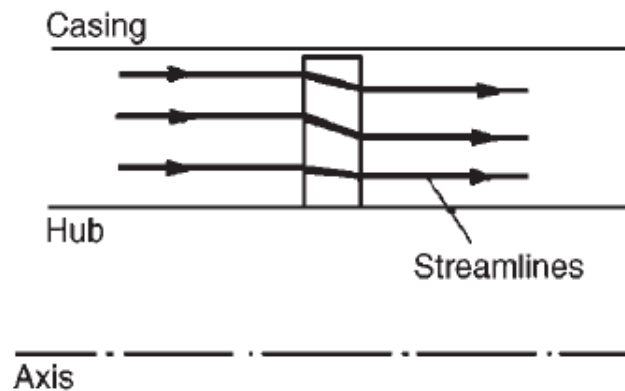


Figure 2.1 Radial equilibrium conditions at the entry and exit of the blade row (Dixon & Hall, 2010).

In areas of a compressor or turbine where the hub-tip ratio is greater than approximately 0.8, radial flows and variations in pressure are negligible, having little effect on the overall flow through the cascade. At hub-tip ratios less than this, the radial velocity variations become a contributing factor to the overall distribution of mass flow through the cascade and must be accounted for (Dixon & Hall, 2010).

## 2.2. Simple Radial Equilibrium Equation

Radial equilibrium is achieved by defining zero radial flow entering and exiting a turbomachinery cascade. To achieve this, a balance between the radial pressure gradient and centripetal force exists. Considering a particle of infinitesimal size, such as that in Figure 2.2 (Dixon & Hall, 2010), the relationship between the pressure gradient and centripetal force (or acceleration considering a body of negligible mass) is derived from the radial momentum equation and can be simplified to Equation 2.1 using the assumption of zero radial velocity along with axisymmetric flow.

$$\frac{1}{\rho} \frac{dP}{dr} = \frac{V_u^2}{r} \quad (2.1)$$

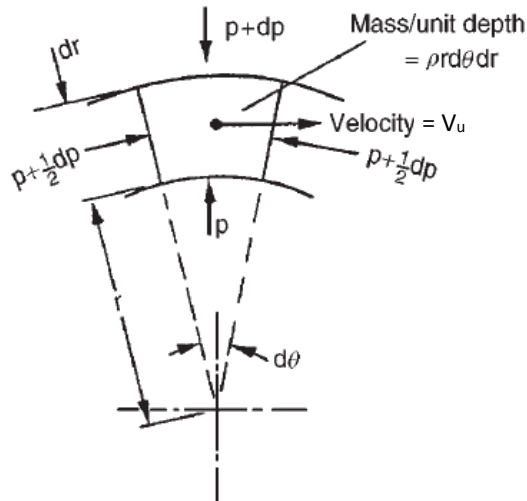


Figure 2.2 Fluid element (Dixon & Hall, 2010).

A method of applying this relationship to turbomachinery design is necessary. Thus, starting with the definition of stagnation enthalpy, using some thermodynamic relationships, Equation 2.1, and by making some assumptions and substitutions, the generalized equation known as the Simple Radial Equilibrium Equation (SREE) can be

obtained, Equation 2.2. The full derivation of this equation can be found in Appendix A.

$$\frac{d}{dr} (V_z)^2 = -\frac{1}{r^2} \frac{d}{dr} (rV_u)^2 \quad (2.2)$$

There are several methods for how this equation is utilized; by defining a circumferential velocity profile with respect to radius, the axial velocity profile can be obtained. A common circumferential velocity profile used is presented by Horlock (1958) in the following form.

$$V_u(r) = ar^n \pm \frac{b}{r} \quad (2.3)$$

Setting  $n = 0, \pm 1$ , three common solutions can be obtained: Exponential, Free Vortex and Constant Reaction. The more frequently used form is the Free Vortex,  $n = -1$ , resulting in a circumferential velocity distribution of  $V_u = \frac{k}{r}$ , where  $k$  is a constant. Substituting this into Equation 2.2, the resultant axial velocity distribution with radius is found to be zero and hence, axial velocity is constant along the length blade.

For all three of the proposed solutions of  $n$ , it can be shown that the work distribution along the length of the blade is also constant. In theory, there are an infinite number of solutions possible for the SREE across all real numbers. However, due to the complexity of the integration to solve the SREE for higher-ordered equations without the aid of computers, these solutions were not explored during the early stages of research into compressor design theory. A number of these vortex solutions have been summarized by Horlock (1958) and can be found in Table A.1, in Appendix A.

### **2.3. Improvements Following the SREE**

There have been a number of design methods to follow SREE design where fewer simplifications and assumptions about the flow have been made. One of these methods is the Actuator Disc Theory. This theory is an extension to the solution of the SREE equation where small radial velocity variations and influences of surrounding blade rows are taken into account to solve for the axial velocity distribution between the blade rows (Carmichael & Horlock, 1957). This method reintroduces the full equations of motion, but localizes the body forces on the infinitesimally thin disk so that the body forces do not actually appear in the resulting equations (Oates, 1988). The disc is placed at some point in the blade channel, usually approximately  $1/3$  of the axial chord, and with that, the axial and radial variations in velocity can be calculated assuming radial equilibrium conditions exist far upstream and downstream of the disc.

The method most commonly used in recent times is the Streamline Curvature method, used in the throughflow design phase, as discussed in section 1.1.2. This is an iterative method that solves the equations of motion, energy and state along a streamline through the cascade. This method is favorable for its ability to handle the various changes in radius encountered in gas turbine engines along with being able to cope with both subsonic and supersonic flows (Dixon & Hall, 2010).

## 2.4. Modifications to the SREE

In modern times, long after the original inception of the SREE, computers have become powerful and readily available. They have become an integral part of turbomachinery design, aiding in all stages of design. With the ability to iterate, integrate and solve simultaneous equations, higher order modifications to the SREE can be explored. Larson (1975) investigated the possibility of a higher-order tangential velocity profile to apply to the SREE by incorporating a second-order term into Equation 2.3, shown in Equation 2.4.

$$V_u(r) = a_2 r^2 + a_1 r + a_0 \pm \frac{b}{r} \quad (2.4)$$

Results showed significant change in relative flow angles at the hub of approximately six degrees, large enough to warrant further investigation. Unfortunately, due to the design of the thesis and lack of CFD programs at the time, no further investigation was completed on the effects of this new vortex method. The overall goal of his work was to generate a design tool to incorporate this new method.

The resulting change in flow angles from this new solution suggests that higher order solutions of the SREE could lead to new blade designs from the preliminary design phase, as discussed previously in section 1.2.

### 3. Hybrid Vortex Concept and Derivation

#### 3.1. Concept

As stated earlier, a new method is to be investigated for application during the preliminary design phase of axial compressors. Examining the fundamental equations discussed in Section 2, the resulting constant axial velocity distribution from the Free Vortex method stood out as a major design flaw. Viscous effects and the presence of the blade itself influence the overall flow distribution along the span of the blade. The combination of these two result in a composite boundary layer that significantly changes the flow behavior at the hub of compressor blades, as seen in Figure 3.1.

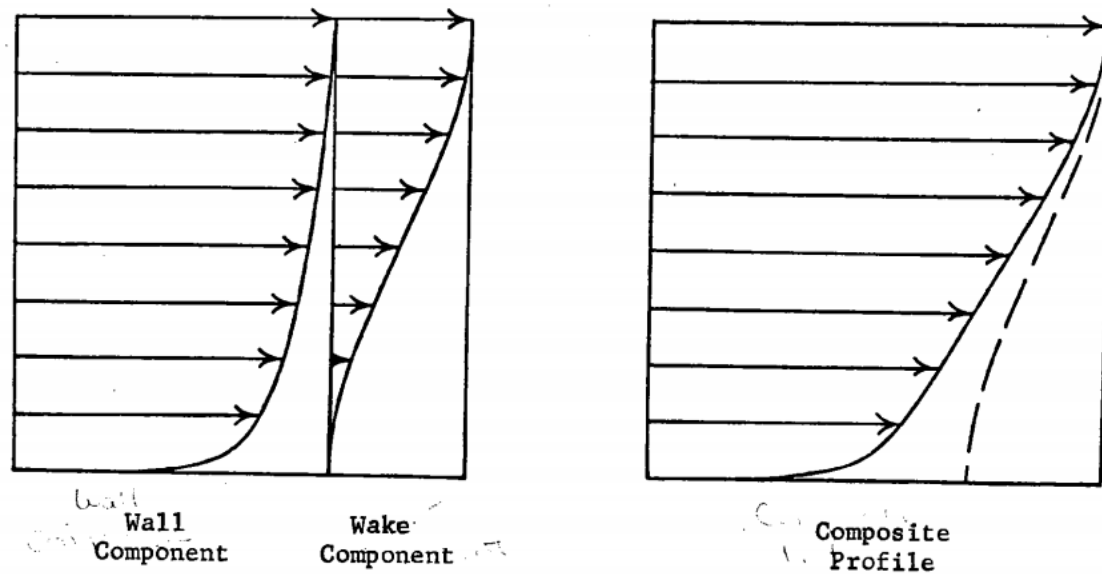


Figure 3.1 Resulting composite boundary layer (Coles, 1969).

Due to this redistributed mass flow, the resulting axial velocity profile is substantially different when compared to the designed constant axial velocity from the SREE. This can be seen in Figure 3.2 below where the resultant axial velocity profile of a



Free Vortex blade is compared to its designed mass flow.

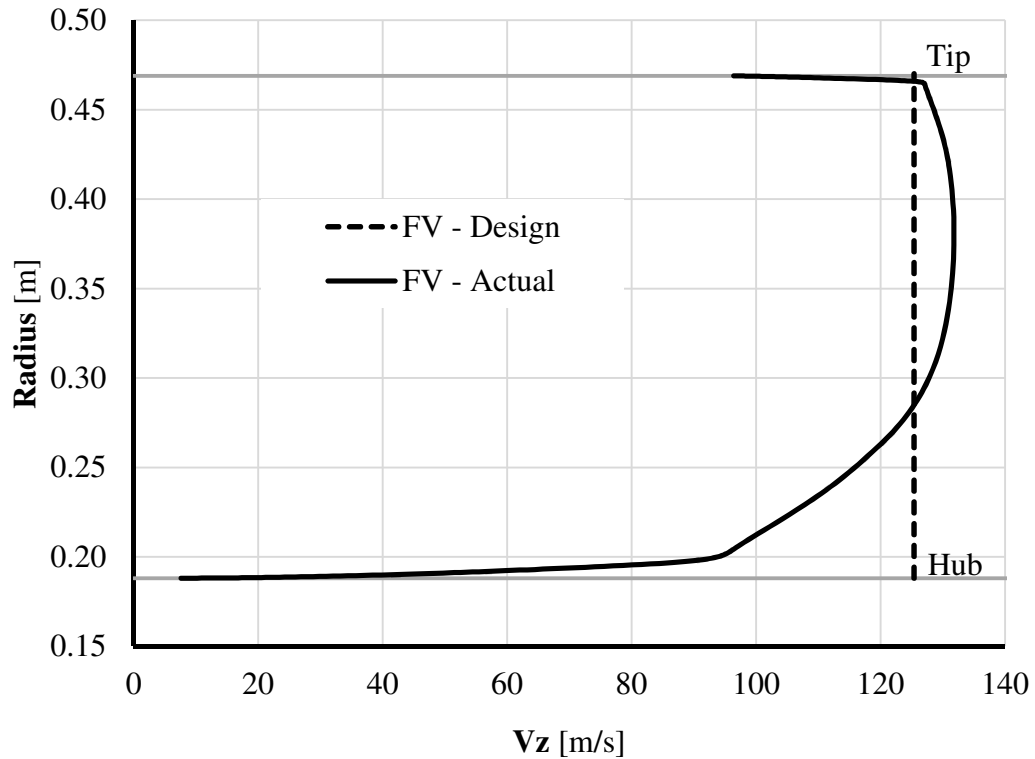


Figure 3.2 Design vs. actual axial velocity distribution

It is from this large discrepancy between design and resulting axial velocity that the concept of this thesis is derived. As opposed to specifying a tangential velocity profile for the SREE, a desired axial velocity profile will be specified and a resulting tangential velocity profile to achieve radial equilibrium will be obtained. To do this, a generalized equation for specifying the axial velocity distribution with radius is required that can then be substituted into the SREE to derive the expression for tangential velocity.

### 3.2. Equation Derivation

An analytical solution to the SREE is desired when given a realistic axial velocity distribution so that true radial equilibrium is obtained. To solve the SREE for a higher order axial velocity distribution, a simplified equation for the axial velocity is required. This equation would be used to curve-fit with either an exported velocity profile as is done in this report to simplify the scope of the research, or with a profile obtained through analytical methods such as those conducted by Horlock and Hoadley (1972).

The vertex form of a polynomial of power ‘B’ was chosen to approximate the axial velocity profile due to its simplicity and ability to fit a large range of velocity profiles.

$$V_z(r) = -A(r - r_m)^B + V_{z,m} \quad (3.1)$$

The benefit of this equation style is the ability to integrate the general equation without requiring a specific number of coefficients dependent on the power of the polynomial. Substituting this back into the SREE and integrating, we can achieve the following vortex solution for the tangential velocity with respect to radius.

$$V_u(r) = \sqrt{\frac{2A(r - r_m)^B}{r^2(B + 1)} \left[ \left( V_{z,m} - \frac{A}{2}(r - r_m)^B \right) \frac{(2r_m^2 + 2r_m Br + B(B + 1)r^2)}{(B + 2)} \right] + \frac{k}{r^2}} \quad (3.2)$$

Where the constants  $r_m$  and  $V_{z,m}$  are obtained from the initial meanline design. ‘A’ and ‘B’ are obtained when curve fitting the axial velocity profile, and the final unknown constant,  $k$ , is obtained by setting  $r = r_m$  and  $V_u(r) = V_{u,m}$  (from the meanline design). This solution, herein referred to as the *Hybrid Vortex*, allows the blade to be designed against the axial velocity profile encountered by the blade due to viscous effects. The full derivation of Equation 3.2 can be found in Appendix B.

### 3.3. Hybrid Vortex Implementation

The proposed Hybrid Vortex method takes advantage of modern computing power to incorporate loops into the design process that are lacking in the baseline design process. The Free Vortex design can be summarized by the flowchart in Figure 3.3 where a single design loop is incorporated into the 2D blade design to achieve the desired blade loadings. This method fails to bridge the gap between 2D and 3D flow within the cascade, using the 2D airfoils, stacked on their centroid to generate the final 3D blade to be built and tested.

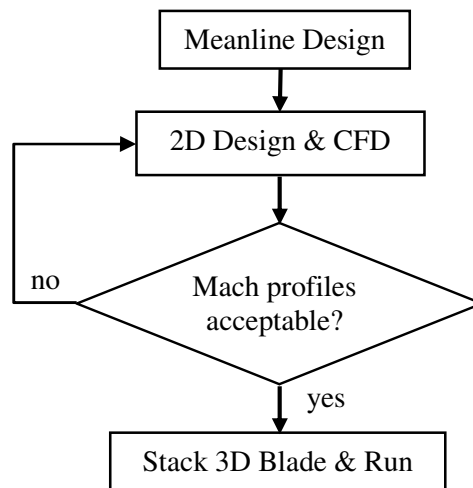


Figure 3.3 Free Vortex design flowchart.

The Hybrid Vortex method utilizes the 3D CFD results to converge on set design parameters such as the axial velocity distribution and Mach profiles. The Hybrid Vortex design flowchart, Figure 3.4, illustrates the additional design loops incorporated into the new method. The first design loop (A) is used to match the required performance parameters of the baseline blade. The second loop (B) is where the 3D results are used to match the derived axial velocity distribution and refine the blade. Converging on the designed axial velocity profile can be considered a micro iteration process, with the Mach

profile refinement a macro loop to optimize the 3D airfoil design.

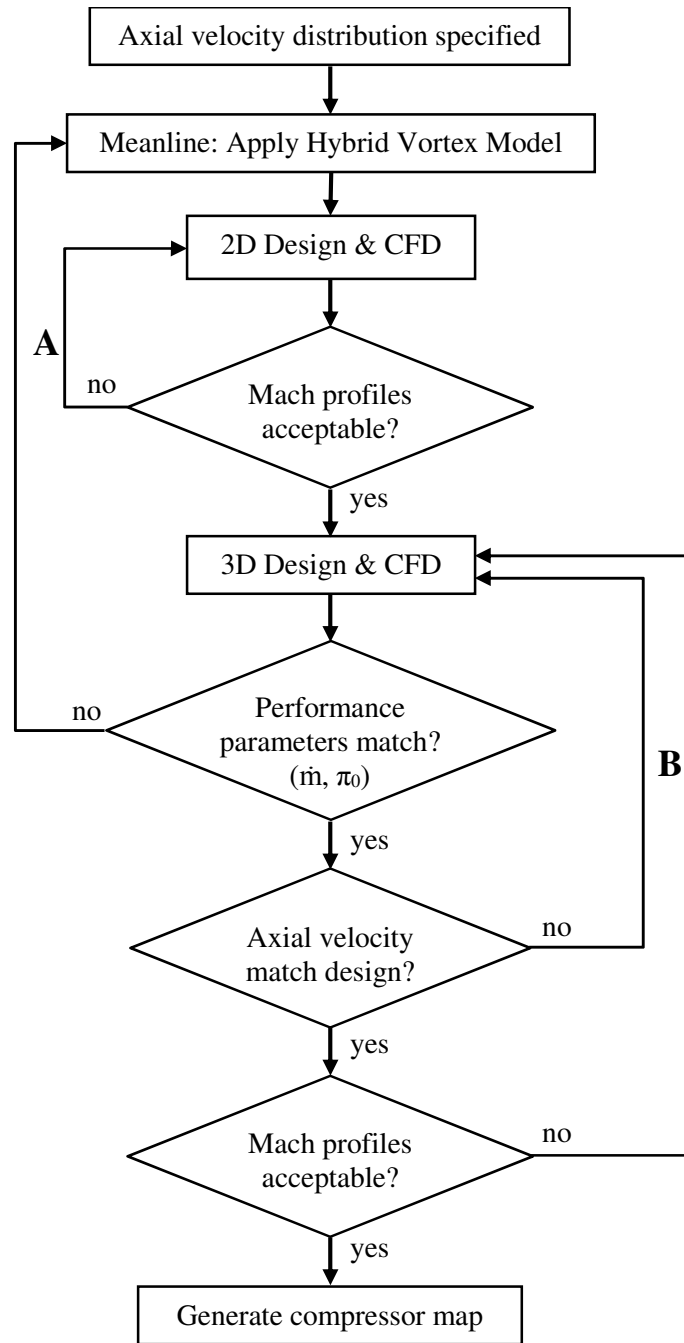


Figure 3.4 Hybrid Vortex design process flowchart.

## 4. Blade Design and Methodology

A single stage from a low pressure compressor with low hub-to-tip ratio and non-axial flow entering the blade was selected for this study. This was selected to produce a blade with large variation of twist from hub to tip, with non-axial flow used to examine the effects of the Hybrid Vortex on the LE design. The baseline compressor was designed using the Free Vortex method discussed in Section 2.2.

### 4.1. Meanline Design

Meanline design was conducted to set the overall geometry and trends of the baseline blade. The compressor was designed at sea level conditions and modelled after a low pressure compressor having approximately 1 m (3.28 ft) tip diameter, similar to that found on a small commercial jet. The major design parameters for the rotor are summarized in Table 4.1.

Table 4.1 Meanline design choices.

Variable	Value
$\dot{m}$	80 kg·s <sup>-1</sup>
$\pi_0$	1.3
H/T	0.4
RPM	7,200
$M_{LE}$	0.38
$P_{0,LE}$	101,005 Pa
$T_{0,LE}$	298.49 K
$\alpha_{m,LE}$	15°
NoB	22
$\sigma_m$	1.385

A smooth annulus shape was achieved, Figure 4.1, maintaining a constant tip diameter through the compressor stage.

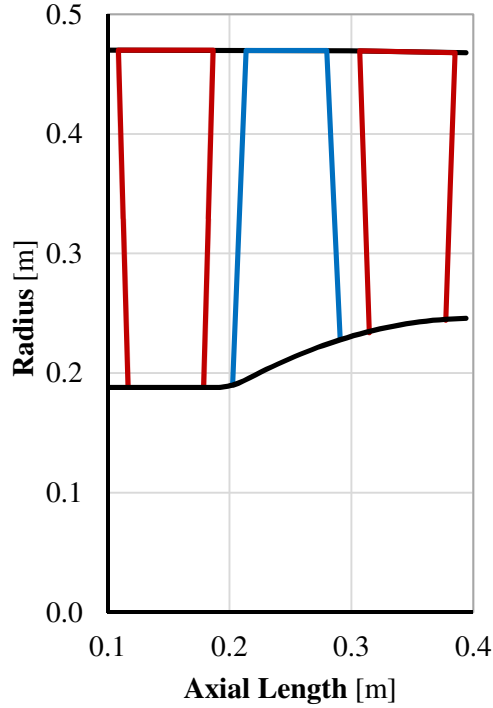


Figure 4.1 Meridional view of compressor annulus.

#### 4.1.1. Hybrid Vortex Design Cases

In order to determine the best method of integrating the new Hybrid Vortex method into compressor blade design, three different cases were selected and tested. Each of these cases shared the same LE design where the axial and circumferential velocity profiles of the Hybrid Vortex, Equations 3.1 and 3.2, were applied. The difference between the three cases is in the design of the TE. To facilitate examination of the effects brought about by the new vortex solution, certain aspects of the baseline FV theory were retained in some of these cases to isolate certain benefits or concerns of the HV. These three cases are summarized in Table 4.2 and are discussed in the subsequent paragraphs.

Table 4.2 Hybrid Vortex TE design cases.

Case #	Axial Velocity	Circumferential Velocity
1	HV method (Eqn 3.1)	Hybrid Vortex method (Eqn 3.2)
2	HV method (Eqn 3.1)	Euler T.M. Eqn.: constant radial $\Delta h_0$
3	FV method: $V_z(r)=const.$	FV method: $rV_u = const.$

### **Case #1**

The first case was a fully Hybrid Vortex blade, using the axial and circumferential velocity profiles from the HV methodology described in Section 3 for both the LE and TE.

### **Case #2**

Upon reviewing the thermodynamics of Case #1, it was discovered that the work distribution was no longer constant, as it is in the FV design methodology. Thus, Case #2 reapplied this relation to design the TE. The TE axial velocity distribution used the HV methodology as in Case #1, but the circumferential velocity profile was determined using Euler's Turbomachinery Equation to calculate the distribution necessary for constant work.

### **Case #3**

The final case retained the TE design methodology used for the FV. Thus, axial velocity was held constant with radius and the relationship  $rV_u = constant$  was used to determine the circumferential velocity component.

## **4.2. 2D Design and CFD**

The 2D blade design was conducted using ANSYS® BladeGen™. The blade geometry is defined by a number of parameters including normal blade thickness, thickness location, LE and TE radii, LE and TE wedge angle, chord and blade angles to name some of the more important parameters. The 2D design was conducted at five separate stream sections along the blade span: at 2%, 25%, 50%, 75% and 98% span.

Two NASA codes were used to complete the numerical analysis. GRAPE and RVCQ3D were chosen for this analysis, due to the high fidelity associated with the two

programs. GRAPE is an elliptic grid generator used for the preprocessing and grid generation for use in the RVCQ3D program, which is a code designed for rapid quasi-3-D flow analysis through turbomachinery. RVCQ3D uses the thin-layer Navier-Stokes equations on blade-to-blade surfaces to solve the given problems with a choice of three turbulence models. Both codes are written in FORTRAN and are operated through text input and output files (Chima, 1999). Samples of both files can be found in Appendices D and F. A custom script, b2r, was used to perform the text I/O transformations required between these programs, and to automatically execute the flow computations and plot results. This script is described in Appendix K.

The airfoil design method used in this study was a velocity/Mach profile matching method. This process involves manipulating the airfoil shape to meet desirable Mach distributions along the airfoil surfaces, with the ideal case shown in Figure 4.2 (a) with  $M_P \approx M_{LE} + (15\% \rightarrow 25\%)M_{LE}$  and  $x_{M_P} \approx (20\% \rightarrow 30\%)x/c$ . The resulting profile for the 25% span section can be seen next to this ideal profile in Figure 4.2 (b).

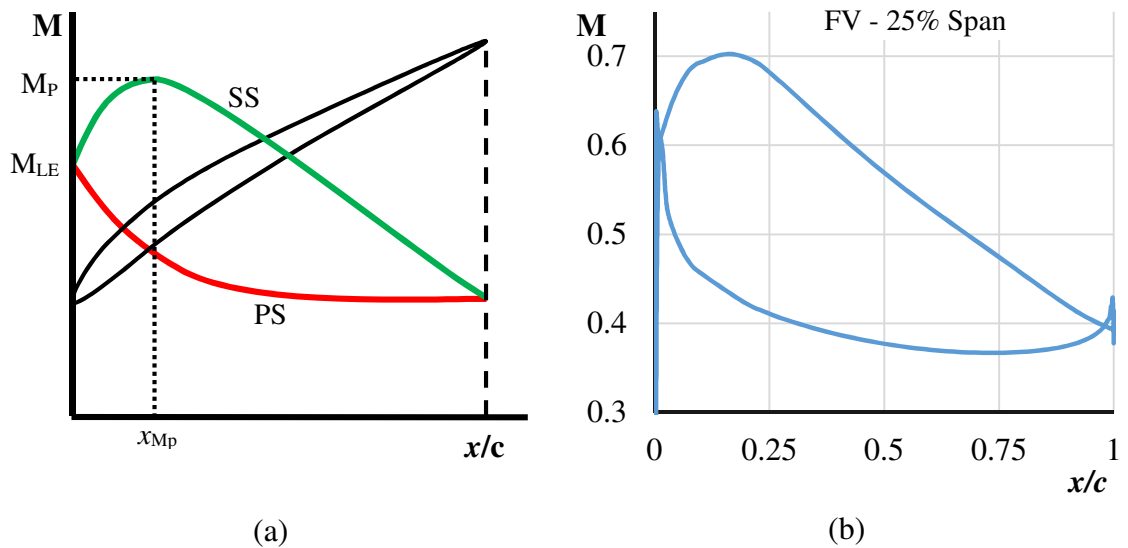


Figure 4.2 Ideal (a) and achieved (b) Mach profile for a compressor blade.



Along with matching these profiles at each 2D slice, overall geometric blade trends regarding thickness-to-chord ratio, LE and TE angles, LE and TE radii, and chord vs the span of the blade are required to be smooth. This ensures that no geometric discrepancies of the blade will affect the results of the simulations.

#### 4.2.1. 2D Meshing and Independency

Although computational time is not an issue with the NASA codes, having a maximum CPU time of 15 seconds for the largest mesh, a mesh independent analysis was completed for the baseline case. Using the GRAPE input file, the mesh size was varied from 4,500 – 21,000 nodes. The combinations of nodes tested are shown in Table 4.3 with the selected mesh size highlighted.

Table 4.3 2D mesh independence total node count.

Total # of Nodes		<i>k</i>		
		60	45	30
<i>j</i>	350	21,000	15,750	10,500
	300	18,000	13,500	9,000
	200	12,000	9,000	6,000
	150	9,000	6,750	4,500
	Max Y+	3.04	16.78	46.14

As can be seen in Figure 4.3 below, independence was achieved at the 18,000 node point for the 300x60 mesh count with the results consistent between this mesh and the 350x60 mesh results and thus, it was the chosen mesh size for the study. This mesh is shown in Figure 4.4 with the LE resolution magnified for clarity.

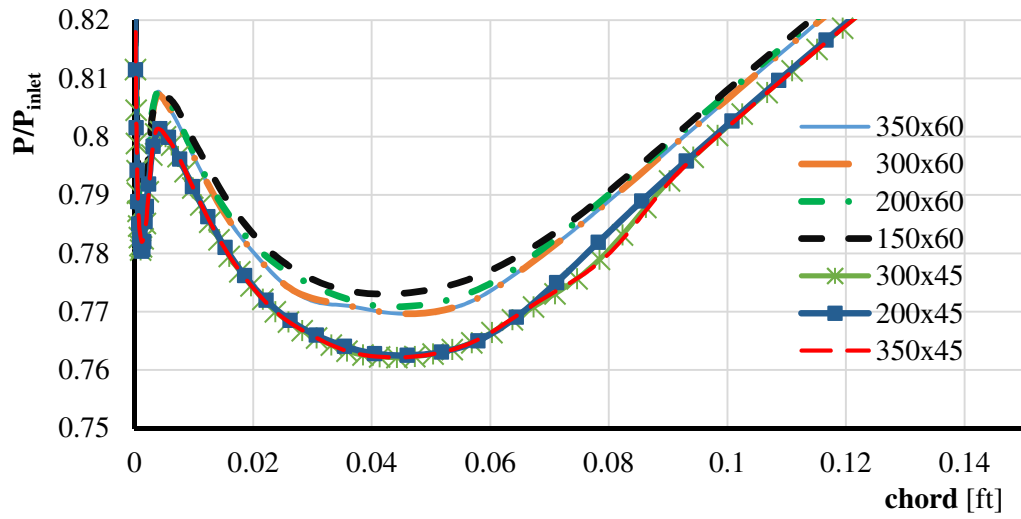


Figure 4.3 2D mesh independence study results.

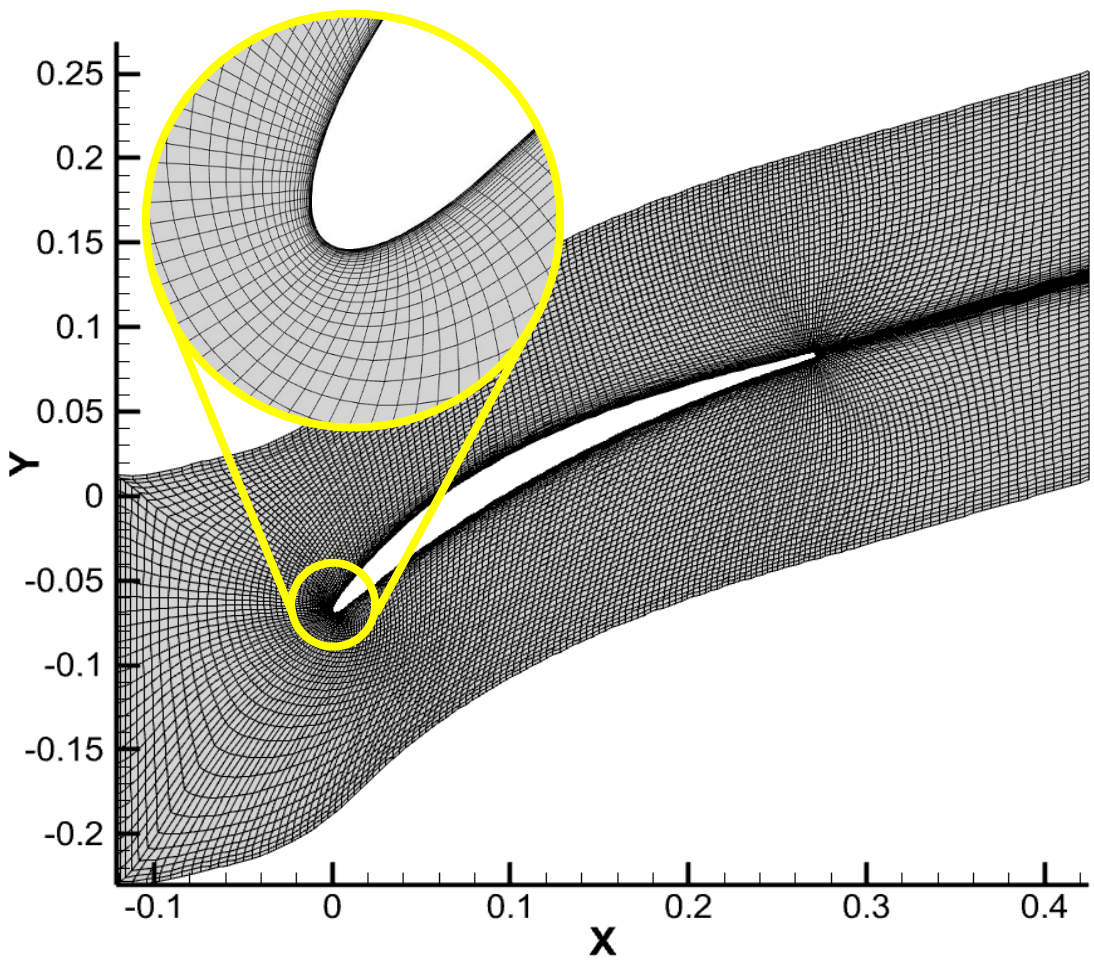


Figure 4.4 Sample of the final mesh at 25% span.

### 4.3. 3D Design and CFD

Three ANSYS® component systems were utilized to complete the 3D design of the blades for this study: BladeGen™, TurboGrid™ and CFX®.

BladeGen™ was used as a continuation from the 2D blade design to stack the airfoils on their centroid. Figure 4.5 shows the resulting blade shape following the stacking process both before (a), and following (b) the smoothing function used to interpolate between the five slices of the blade.

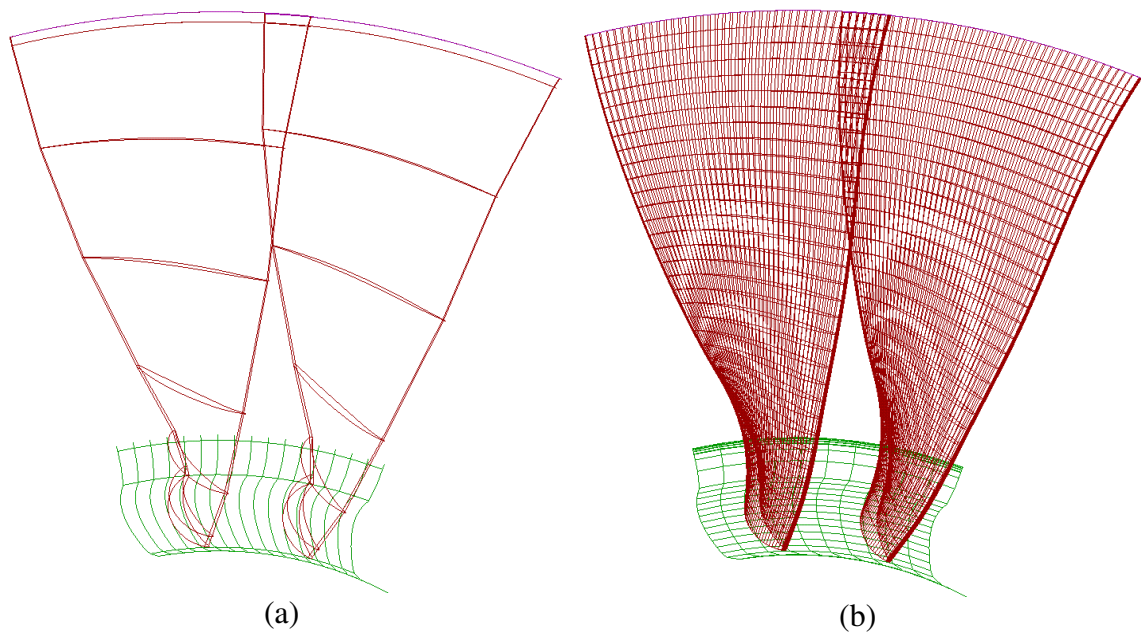


Figure 4.5 Free Vortex airfoil sections stacked to form the 3D blade.

#### 4.3.1. 3D Meshing

Meshing of the 3D blade was completed using ANSYS® TurboGrid™, a meshing program designed primarily for use in turbomachinery. TurboGrid™ uses built-in grid topologies to ensure an optimal mesh is generated with minimal input from the user. This is key for rapid design iterations when completing 3D design iterations on single, or

multiple blades. This also ensures self-consistent meshing between design iterations to minimize mesh dependency on small design changes. Coinciding with general turbomachinery best practice guidelines for running CFD, a structured, hexahedral mesh was used throughout the entire domain. Figure 4.6 shows an example of the topology used in the blade passage with the final mesh superimposed to show the boundary layer refinement.

**ANSYS**  
R16.0  
Academic

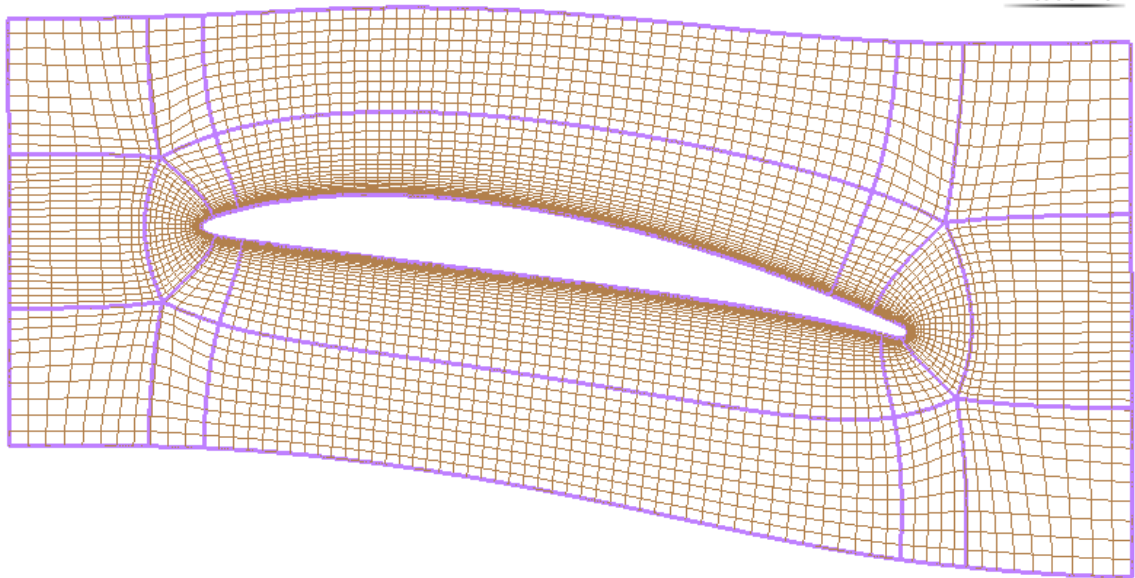


Figure 4.6 Topology sample displaying the final refined mesh.

Three mesh sizes were studied to ensure a solution independent of the mesh density. The criteria for the three meshes are shown in Table 4.4. The final mesh size deemed acceptable was the medium mesh of approximately 2.5M elements. This common mesh was maintained for the remainder of the study in order to ensure mesh consistency.

A constant tip gap of 0.5% span was imposed during the meshing process with the number of cells spanning the gap also displayed in Table 4.4 for each mesh. A sample of the refinement in the tip gap can be found in Figure I., Appendix H.

Table 4.4 Mesh sizing for independent study

<b>Rotor</b>	<b>Course Mesh</b>	<b>Medium Mesh</b>	<b>Fine Mesh</b>
<b>Cells</b>	1.0M ( $\pm 50k$ )	2.5M ( $\pm 50k$ )	5.0M ( $\pm 50k$ )
<b>Cells in tip gap</b>	40	55	75
<b>Target Y+</b>	$\leq 10$	$\leq 5$	$\leq 2$
<b>Min. grid angle</b>	30	30	32
<b>Max Aspect Ratio</b>	2,500	2,650	3,900

Due to CFX<sup>®</sup>'s built in wall function, the maximum Y+ value of 5 is more than acceptable for obtaining accurate boundary layer results, with the majority of the blade having a value of less than 2. A contour demonstrating the Y+ of the blade can be found in Figure I.2, Appendix H.

The final mesh of the full domain can be seen in Figure 4.7 with the LE magnified to show the refinement of this critical area.

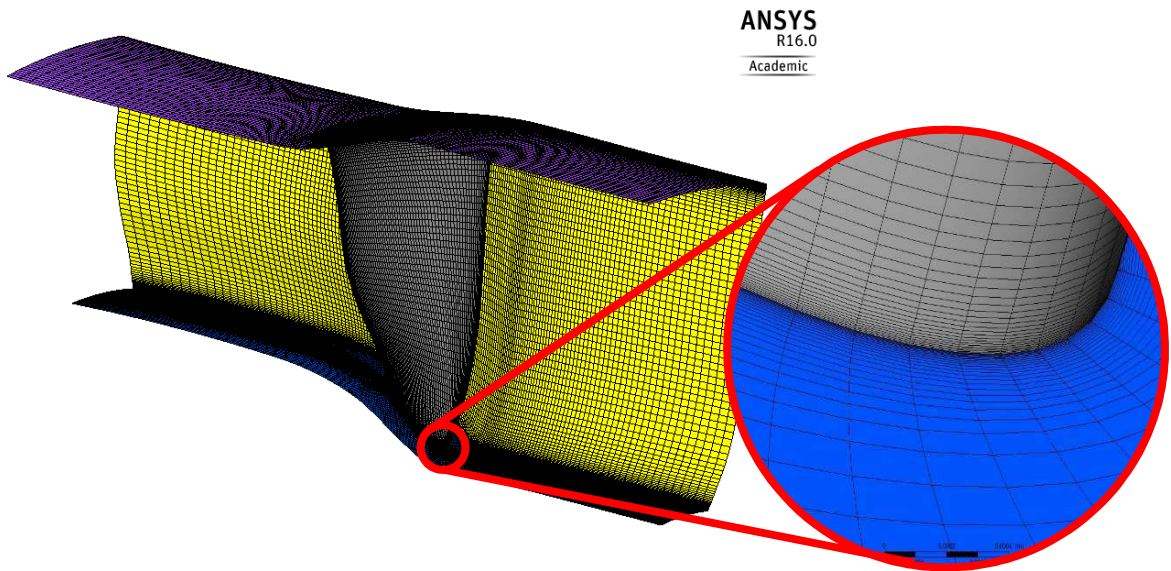


Figure 4.7 Final medium mesh with LE refinement magnified.

### **4.3.2. Simulation Setup**

ANSYS® CFX® was chosen for this analysis due to its robustness and speed for analyzing turbomachinery. The numerical methodology used for the analysis was structured after a study by Cornelius *et al.* (2014) where, in conjunction with Siemens, a multi-stage axial compressor was numerically compared to experimental results for predicting the onset of stall using both steady and transient simulations.

### **Boundary Conditions**

The blade was simulated as steady state using total pressure and temperature inlet conditions with either averaged static pressure outlet, mass flow outlet or corrected massflow outlet with near identical results. The pressure outlet condition became numerically unstable upon approaching the surge point of the blade, whereupon the mass flow outlet condition was used to verify surge had been reached - as evidenced by a sudden 'dip' in the characteristic. Some numerical issues arose due to high transonic flow during runs having high RPM. For these situations, corrected mass flow boundary conditions were imposed, as recommended by the ANSYS® Reference Guide, in order to correct the convergence issues.

In addition to the inlet total conditions, an inlet velocity profile was specified to simulate the flow from an inlet guide vane. In order to simplify the study, it was assumed that the inlet guide vane or stator was able to provide the required absolute flow angle desired for each vortex solution at the design condition. The initialization files for these profiles are attached in Appendix H.

Outlet conditions and RPM were changed to generate the full compressor maps while inlet conditions remained constant.

## Turbulence Model

In accordance with Cornelius *et al.* (2014), the Shear-Stress-Transport (SST) with the Reattachment Modification (RM) turbulence model was selected, due to its ability to more accurately predict surge. The SST model alone has a tendency to prematurely predict the onset of surge and the  $k$ - $\epsilon$  model leads to a high surge point due to its inherent delayed prediction of separation. Thus, the SST+RM model was used for all test cases.

## Convergence Criteria

Multiple convergence criteria were imposed to ensure an accurate and consistent solution was met for all simulations. Three main criteria, listed in Table 4.5, were set to declare convergence has been achieved. Convergence was achieved within 1,500-2,500 iterations, with simulations close to surge requiring higher iteration counts to settle on a solution.

Table 4.5 Convergence criteria.

Monitor	Criteria for Convergence
Residual RMS	$< 10^{-4}$
Domain Imbalance	$< 1\%$
Mass flow Efficiency Total Pressure Ratio	Steady Solution $\Delta\{\dot{m}, \eta_{tt}, \pi_0\} < 10^{-4}$

## 5. Results

### 5.1. Baseline Case – Free Vortex

#### 5.1.1. Meanline

As discussed in Section 4.1, the Free Vortex method for radial equilibrium was chosen for the baseline blade design. The main focus of the meanline design was to create a blade that was moderately loaded, and isolate the features of the new method. Starting from a poor blade will not fully demonstrate one method's superiority over another. The aerodynamic health parameters of the blade were the criteria used to judge the initial performance of the baseline blade. These criteria, their selected limits and status are listed in Table 5.1.

Table 5.1 Aerodynamic health properties of baseline blade.

Parameter	Criteria	Value	Status
Work Coefficient ( $\lambda$ )	$0.2 < \lambda < 0.5$	0.3740	<i>Achieved</i>
Flow Coefficient ( $\Phi$ )	$0.3 < \Phi < 0.75$	0.4652	<i>Achieved</i>
Average Diffusion Factor	0.45	0.3476	<i>Achieved</i>
DeHaller Number	$DH > 0.68$	0.7314	<i>Achieved</i>
$\Delta\beta_{\max}$	$\Delta\beta < 40^\circ$	$44.26^\circ$	<i>Failed</i>
Degree of Reaction	N/A	0.6532	N/A

It can be seen that the baseline blade satisfies all criteria excluding the change in relative flow angle at the hub. This was deemed acceptable due to the high solidity at the hub of the blade, resulting in an acceptable Diffusion Factor at the hub of 0.38.

Also obtained from meanline design are the velocity triangles showing the variation of the absolute and relative velocities and their angles through the cascade. A sample of these triangles are shown in Section 5.2.1.



### 5.1.2. 2D Design

The 2D design of the baseline blade was conducted using the methods discussed in Section 4.2. This process was used to iteratively converge on a set of airfoils that met the necessary flow criteria set by the meanline design and the Mach profiles. The 50% span Mach profile is shown in Figure 5.13, with the rest of the profiles found in Appendix G.

While conducting the airfoil design, the geometric trends between the span sections were monitored to ensure that a smooth trend was achieved. The geometric trends can be found in Appendix D.

To minimize LE spikes in the Mach profiles, an elliptical LE design was chosen. Based on a thesis by Powell (2005), an elliptic ratio of three was chosen. The elliptical LE design leads to reduced separation bubbles at the LE where high flow acceleration can occur. Figure 5.1 shows the difference in LE geometry at 25% span with Figure 5.2 demonstrating the impact of the elliptic design on the Mach spikes formed at the LE.

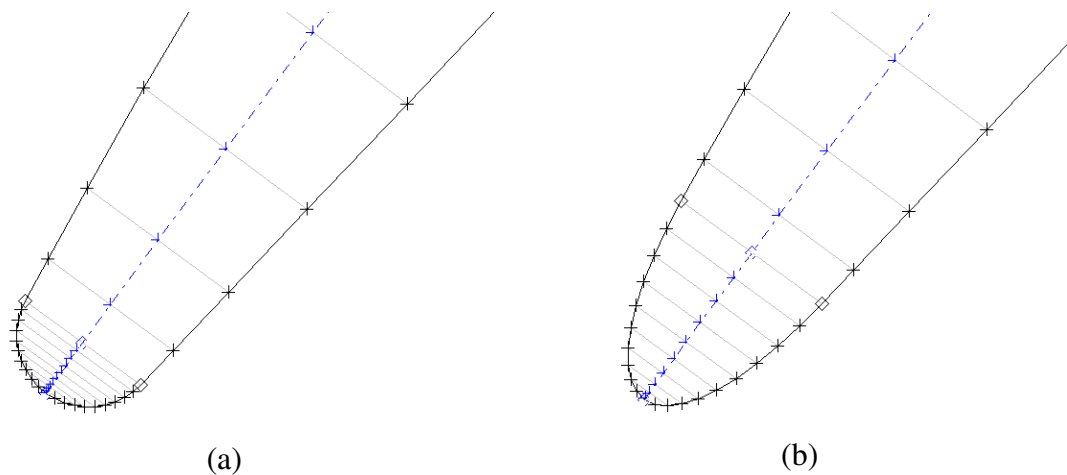


Figure 5.1 Comparison between circular (a) and elliptic (b) LE design at 25% span.

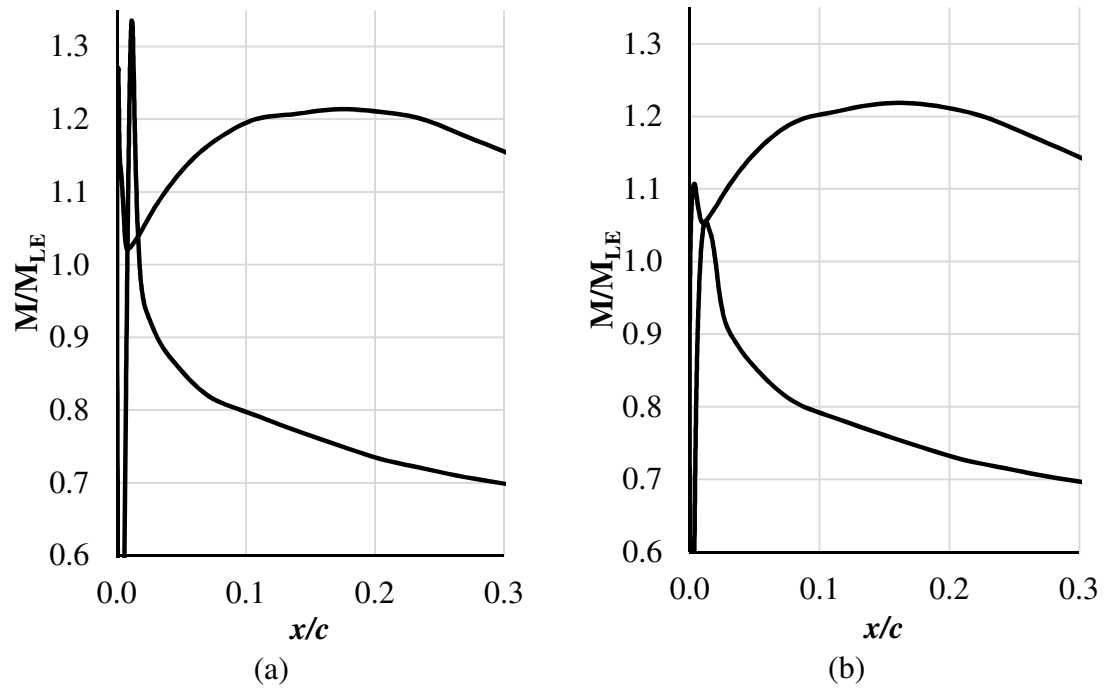


Figure 5.2 LE Mach spike comparison of circular (a) and elliptic (b) LE at 25% span.

Upon satisfaction of all Mach profiles and geometric trends, the airfoils were stacked upon their centroids to form the final 3D blade. The stacked layout of the Free Vortex blade is illustrated in Figure 5.3.

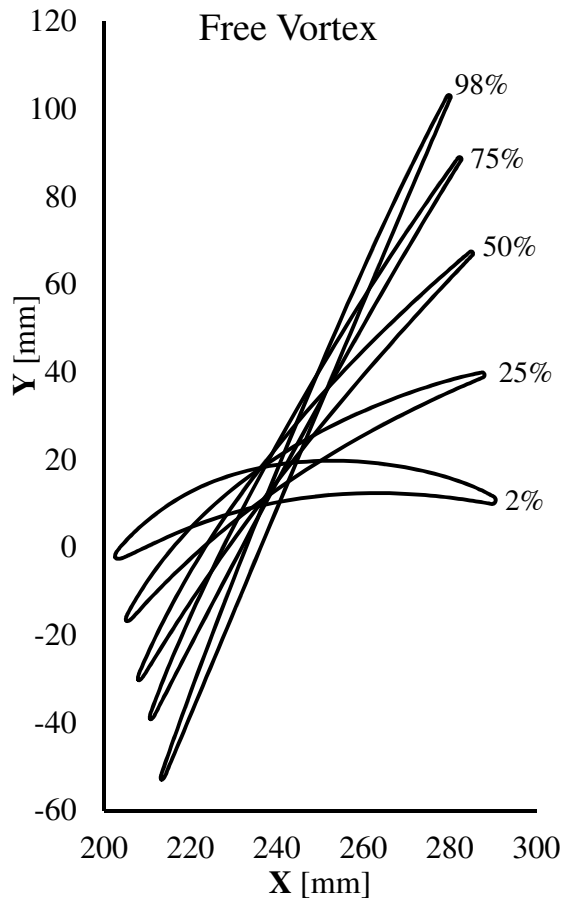


Figure 5.3 2D airfoil sections of the Free Vortex stacked on their centroids.

### 5.1.3. 3D Performance and Observations

The baseline blade was computationally tested using the process previously outlined in Section 4.3, resulting in the final overall design point performance listed in Table 5.2.

Table 5.2 Baseline performance parameters.

<b>Mass Flow [kg/s]</b>	79.7
<b>Pressure Ratio</b>	1.302
<b>Isentropic Efficiency</b>	94.45

Due to the nature of the Free Vortex design method, as discussed in Section 3.3, no 3D design was completed on the blade. Thus, the 3D CFD is used as a compressor performance evaluation tool to observe the influence 3D flow has on the blade.

A number of poor flow features arose from the Free Vortex design with positive incidence seen at the hub of the blade, Figure 5.4, as predicted due to the large difference in design and resultant axial velocity profiles (recall Figure 3.2).

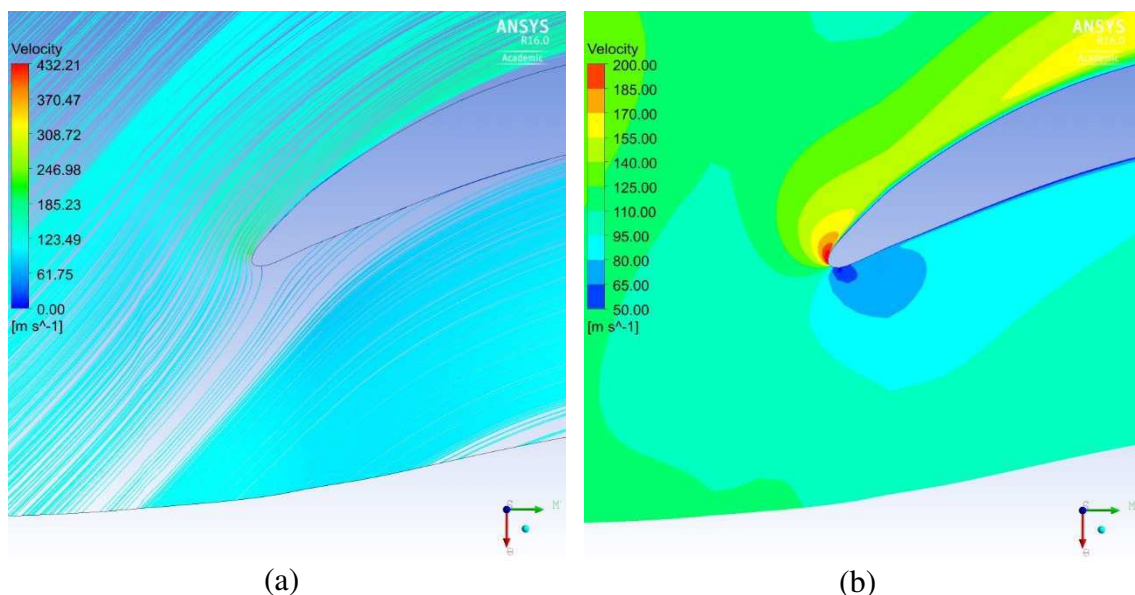


Figure 5.4 Velocity streamlines (a) and contour (b) of the LE at 2% span for the FV blade.

An additional consequence of the redistribution of mass flow is the local increase in mass flow from approximately 30% span upwards. This redistribution results in high levels of negative incidence, see Figure 5.5, which limits the efficiency of the blade. However, this also results in an increase in the incidence range the airfoils can operate in, leading to a fictitious extension to the surge margin of the rotor.

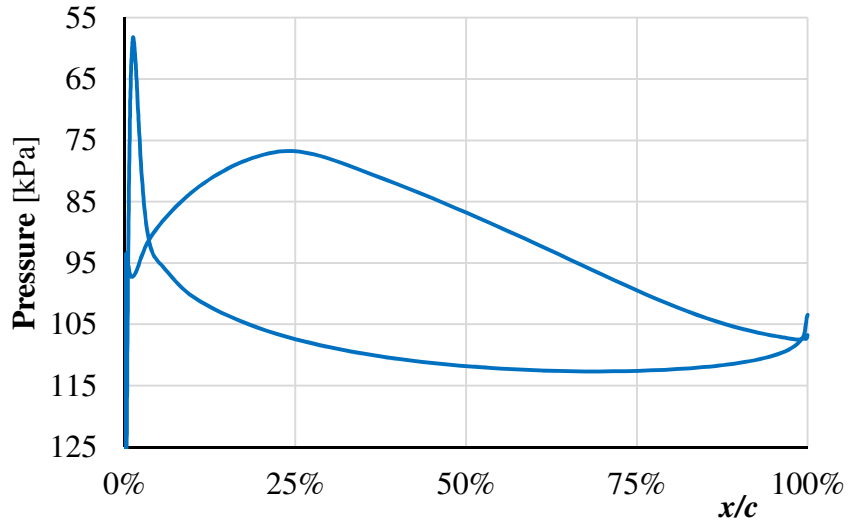


Figure 5.5 Pressure contour at 50% span.

With the designed axial velocity distribution not achieved, the SREE is violated resulting in a loss of radial equilibrium. With the severe decrease in momentum at the hub, the balance of forces is overcome by the centrifugal force imposed on the flow by the rotating cascade. This imbalance results in substantial radial travel from the hub of the blade up to 35% span, as illustrated in Figure 5.6.

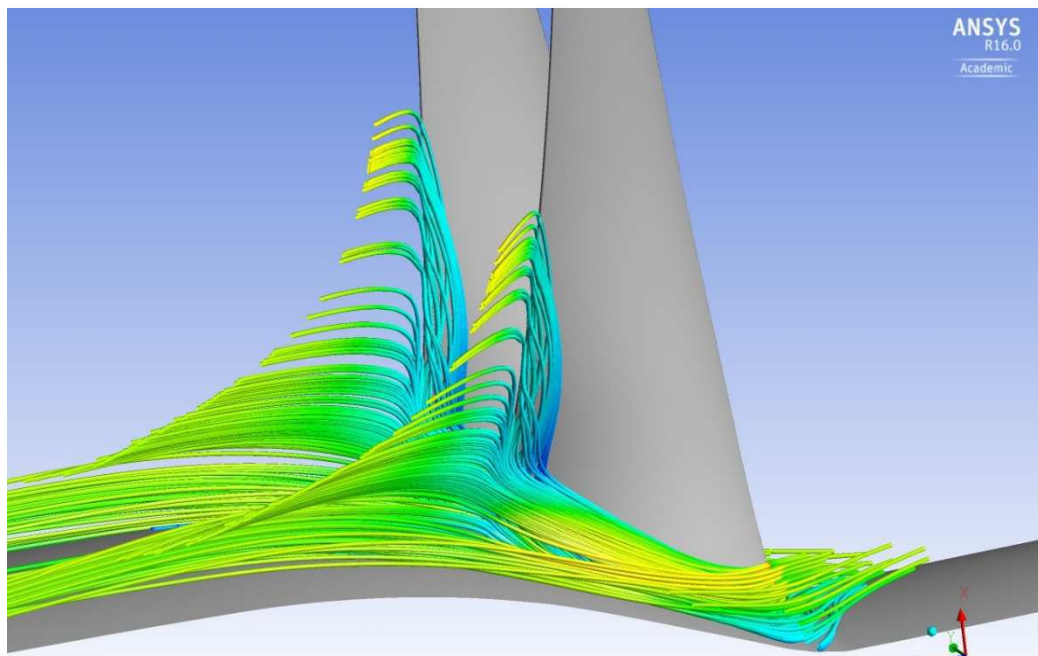


Figure 5.6 Hub streamlines of the Free Vortex blade at the design point.

## 5.2. Hybrid Vortex 2D Design Loop

Referencing the Hybrid Vortex design flowchart, Figure 3.4, the first step is to obtain the axial velocity equations for the LE and TE. This was completed using a mass-balance, curve-fitting process where the axial velocity profiles obtained from the Free Vortex CFD results were set as the desired profiles for the new Hybrid Vortex blades. A mass balance is required to ensure the correct mass flow through the blade channel. Due to the application of the simplified equations, some areas will result in higher or lower values for the axial velocity profile as seen in Figure 5.7. From this figure, it can also be seen that the extreme outer edges of the annulus (0%-2% and 98%-100% span, where the flow is dominated by the boundary layer) were neglected in this curve-fitting process, due to the unpredictable flow in these regions. Neglecting these outer limits results in a smoother, more mechanically sound blade shape through the outermost sections of the blade span.

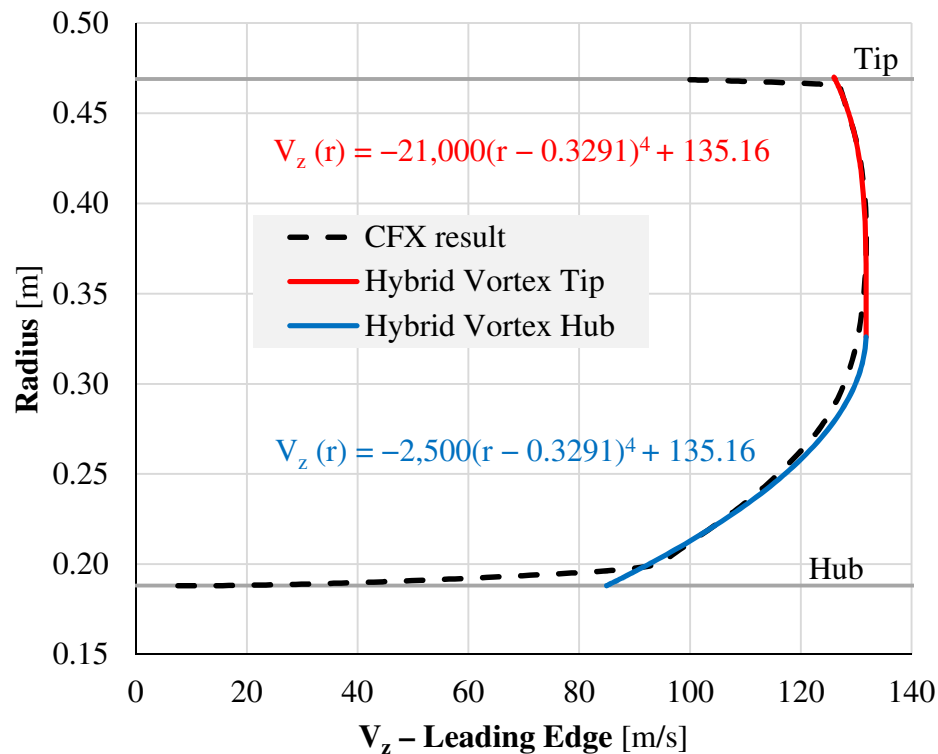


Figure 5.7 Hybrid Vortex equation fitting for the LE.

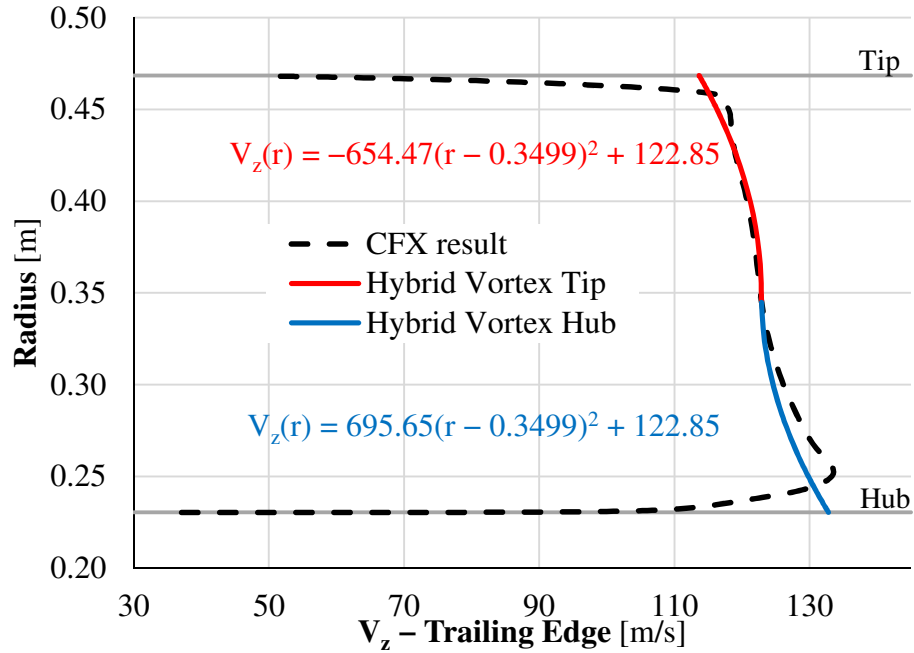


Figure 5.8 Hybrid Vortex equation fitting for the TE.

From the curve fit equations obtained in the above two figures, the derived circumferential velocity equation can be applied to determine the circumferential velocity distributions. These distributions are shown in Figure 5.9.

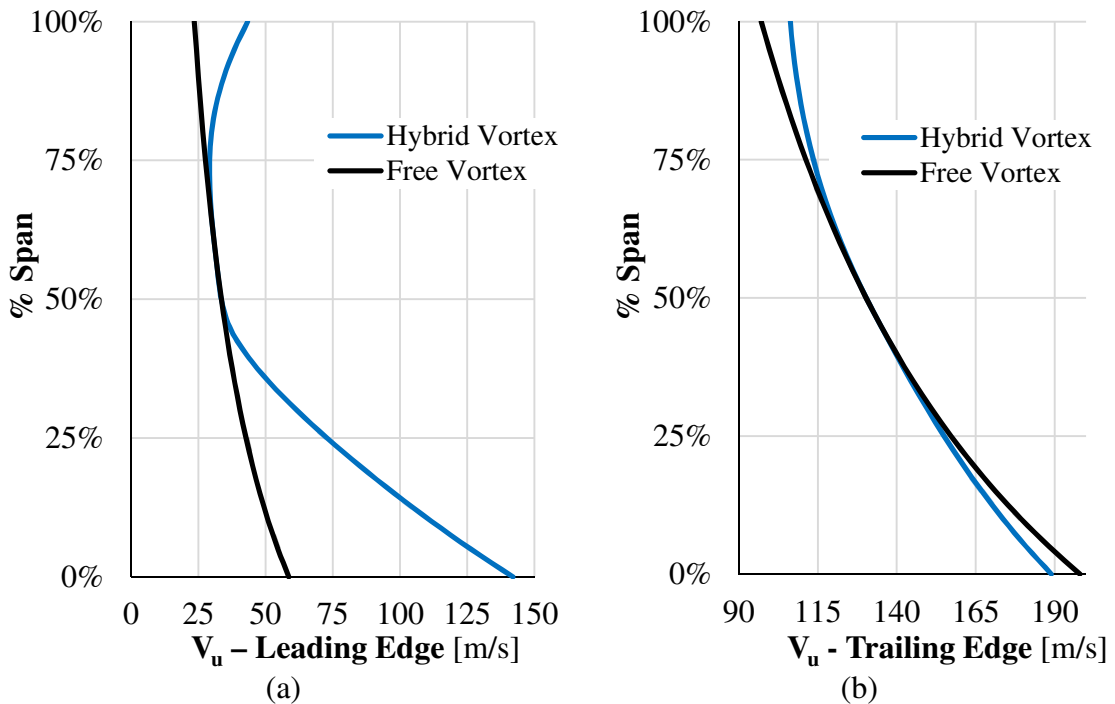


Figure 5.9 Circumferential velocity profiles for the LE (a) and TE (b).

### 5.2.1. Meanline Design

The curve fitted axial velocity, and resultant circumferential equations can now be applied to the meanline design code to generate the triangles for each of the Hybrid Vortex cases. The meanline design of the Hybrid Vortex blades resulted in significant changes to the blade geometry, mainly in the lower 25% of the blade span. Early indications of this trend can be seen in the velocity triangles, illustrated in Figure 5.10, where the HV Case #1 triangles are superimposed onto the Free Vortex triangles at 2% span.

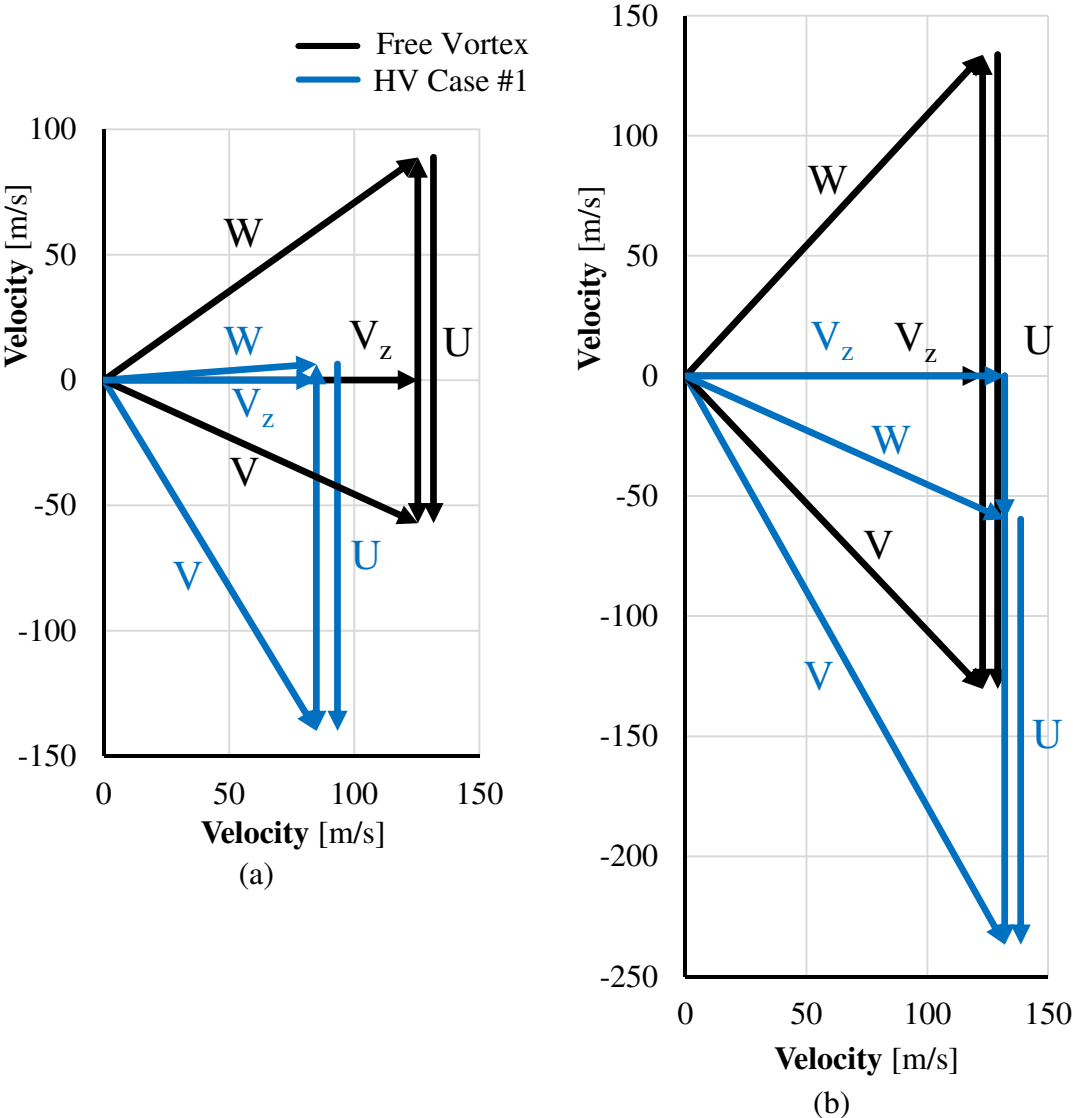


Figure 5.10 Velocity triangle comparison at 2% span for the LE (a) and TE (b).



This substantial difference in velocity triangles can be observed along the span of the blade by plotting the relative velocity angle trends at both the leading and trailing edges, as seen in Figure 5.11 and Figure 5.12, remembering that all three Hybrid Vortex blades share the same LE design.

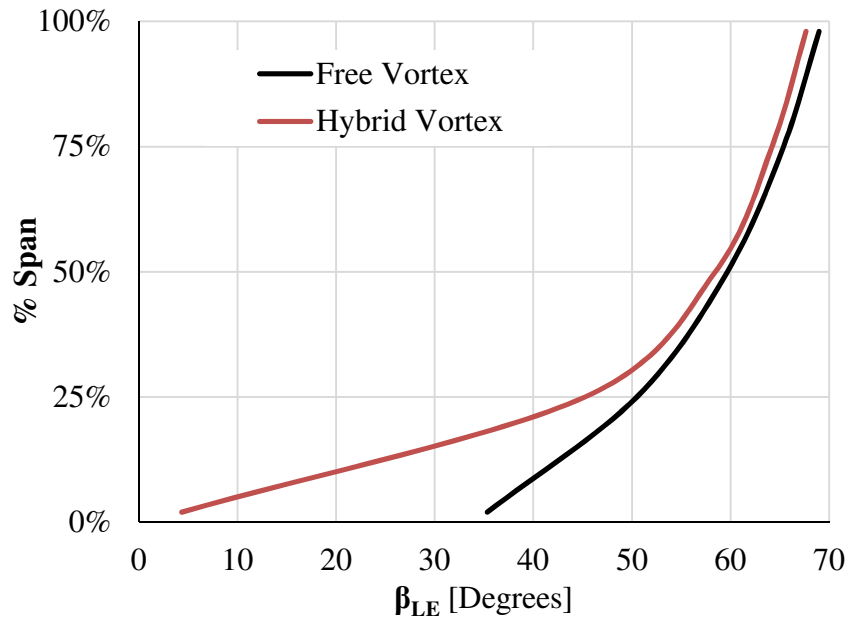


Figure 5.11 LE relative flow angle comparison between the FV and HV blades.

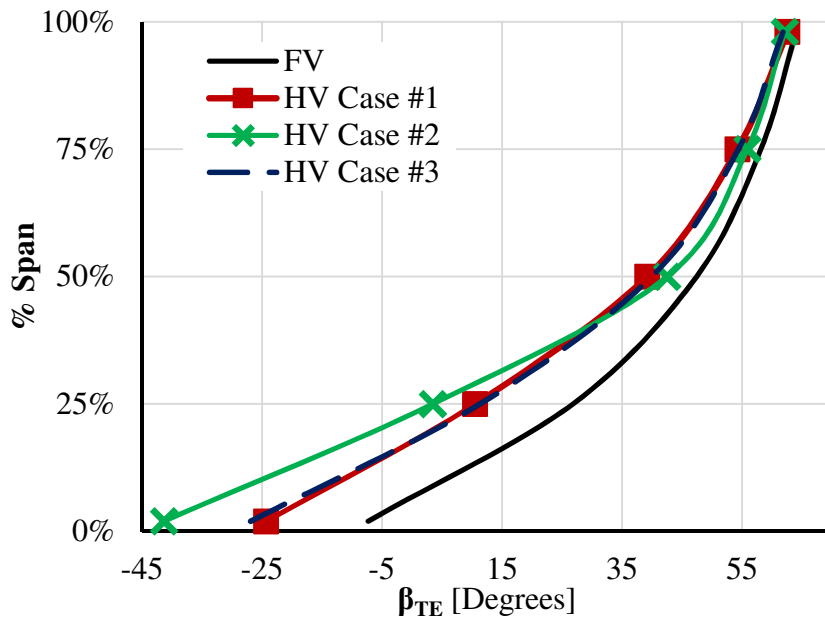


Figure 5.12 TE relative flow angle comparison between the FV and HV blades.

All aerodynamic values from the meanline design, and hence the velocity triangles, are tabulated in Appendix C.

A fascinating aero/thermodynamic feature observed during this stage of the HV design occurs in the hub region of the blade. Contrary to standard compressor theory, the new solution accelerates the relative flow through the blade channel, which will theoretically help mitigate the issue of the adverse pressure gradient within the lower ~15% of the span. In an area prone to separation due to high camber, such as the hub, this feature has the potential to reduce the risk of hub stall and will be a significant point of interest during the final analysis of the blade.

### **5.2.2. Airfoil Design**

Consistency in both the blade geometry and meshing was achieved by copying the final ANSYS® Workbench used for the Free Vortex blade separately for each Hybrid Vortex blade, a total of three copies. The geometry was then manipulated in BladeGen to achieve an initial design for each of the Hybrid Vortex blades. The iterative airfoil design process described in Section 4.2 was conducted to achieve the required Mach distributions across each section of the three HV cases.

To minimize unwarranted improvements or losses to the performance of the new blades, similar blade loadings between all cases was required. To achieve this for each of the five span locations, the Mach profile was plotted with the profiles for each design case, while normalizing values based on the LE Mach number. This allowed visual comparison of the similarities between each design to ensure no outlying factors contributed to significant changes in the flow around the blade. The 50% span is shown in Figure 5.13 to illustrate how this method was utilized, with the remainder of the profiles shown in

Appendix G for reference.

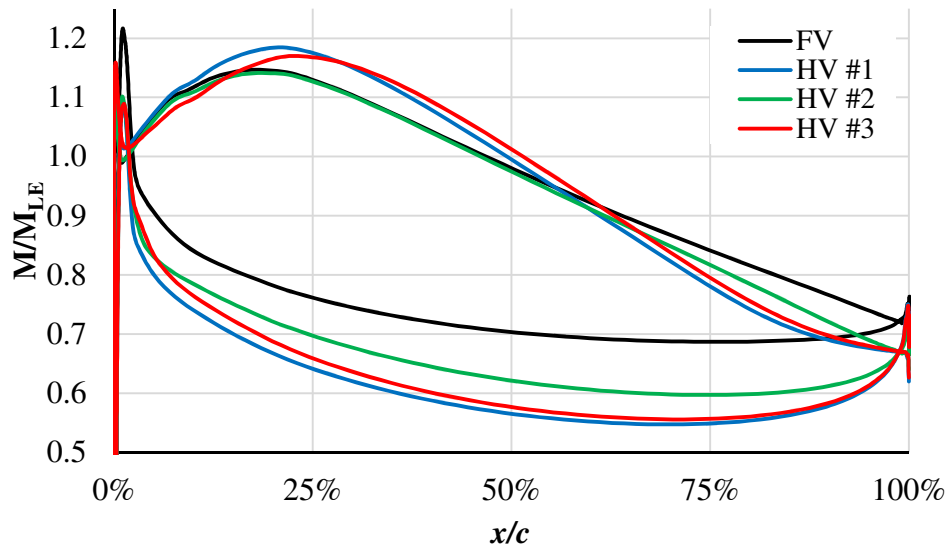


Figure 5.13 Normalized Mach distribution for all four designs at the 50% span.

Due to varying exit Mach numbers and flow angles, the TE's tended to have dissimilar conditions and attention was focused mainly on the retention of similar peak Mach numbers and the location of that peak.

### Design Point Matching

With reference to the Hybrid Vortex design flowchart, Figure 3.4, a design iteration loop was now required to match the design point conditions of the baseline case. To achieve this, each HV case was run through 3D CFD using the design mass flow rate to obtain the current operating conditions. From these results, the meanline design was adjusted at the TE, slightly reducing stagger and the TE metal angle if the desired pressure ratio was not achieved for the design mass flow, and vice versa if the pressure ratio was too high. This was followed by repetition of the 2D design and CFD processes. This methodology was used until the required performance characteristics were converged upon. The final

performance parameters following the 2D design of the HV cases are displayed in Table 5.3.

Table 5.3 Final design point values for all 2D design cases.

<b>Rotor</b>	<b>FV</b>	<b>HV Case #1</b>	<b>HV Case #2</b>	<b>HV Case #3</b>
<b>Mass Flow [kg/s]</b>	79.70	79.70	79.70	79.70
<b>Pressure Ratio</b>	1.302	1.299	1.296	1.301
<b>Isentropic efficiency</b>	94.45	91.19	91.26	91.66

The final airfoil sections could now be compared to see the contrast between the baseline blade and the three Hybrid Vortex cases. As previously discussed, the largest transformation came in the design of the hub, with only minor differences in the rest of the blade. The 2% span and 25% span airfoils are compared in Figure 5.14 and Figure 5.15 respectively, with the remainder of the airfoil section comparisons located in Appendix G.

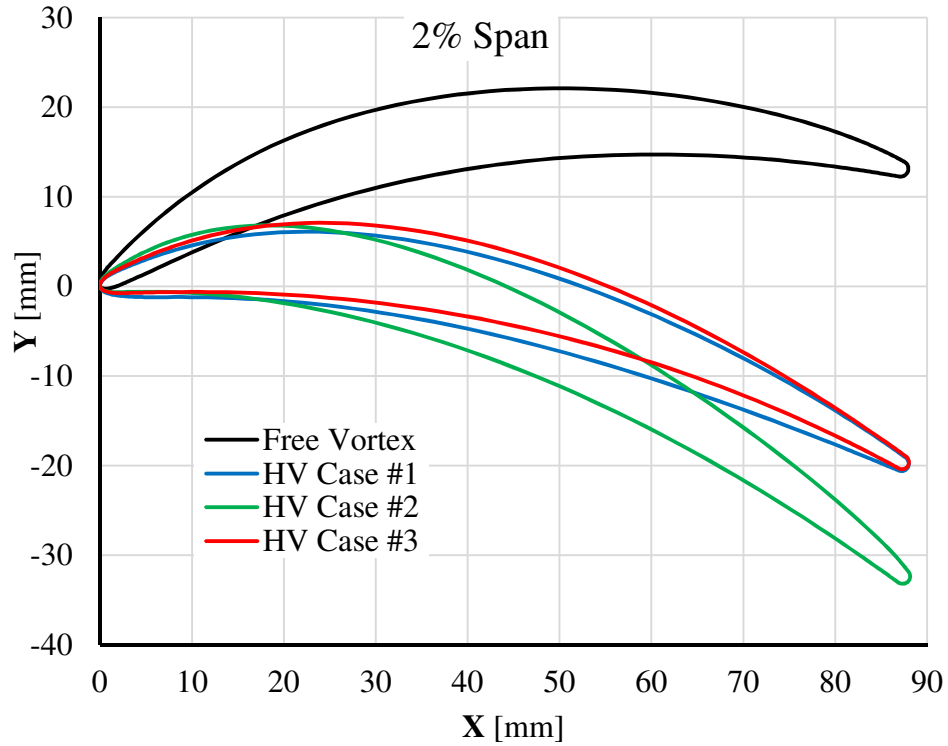


Figure 5.14 Airfoil sections of all four design cases at 2% span.

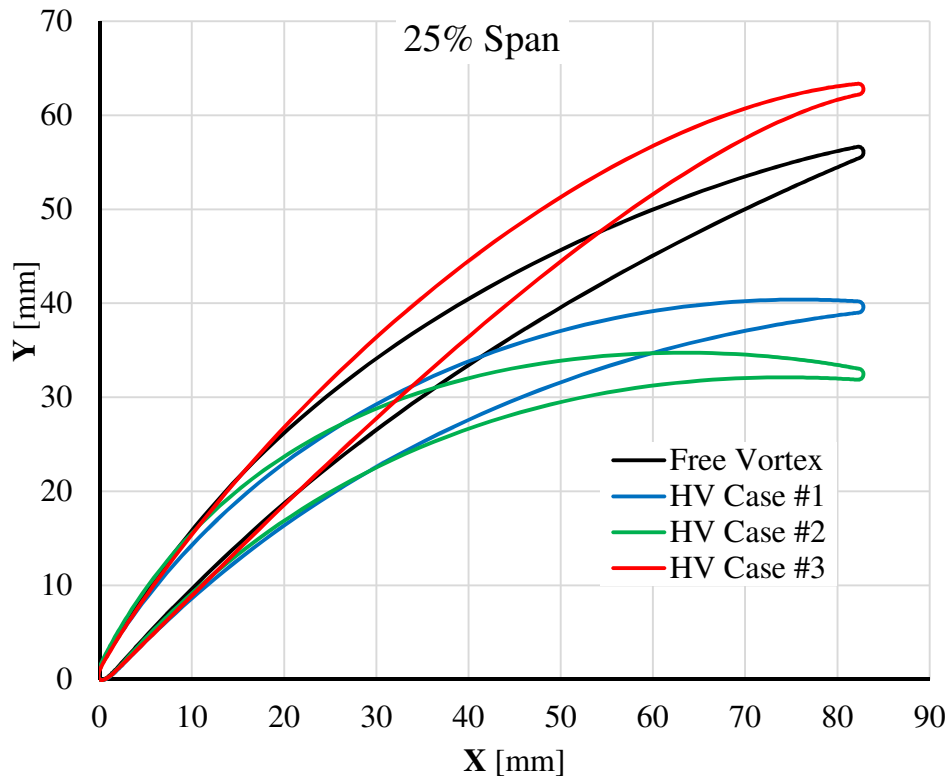


Figure 5.15 Airfoil sections of all four design cases at 25% span.

Also located in Appendix G are the full stacked plots of each HV design case, showing the overall twist in the blade through all sections.

### **5.3. Hybrid Vortex 3D Design Loop**

#### **5.3.1. Final Hybrid Vortex Case Selection**

The first step required to complete the 3D design iteration for the Hybrid Vortex was to select the best of the three cases to continue through this final design process. This selection was done to reduce the overall scope of the blade design effort, due to the high labor and computational costs of running the full 3D simulations.

In order to determine the best of the three design cases for advancement to the 3D design effort, each blade was analyzed for favorable traits. From Table 5.3 it can be seen that all cases have similar performance specifications, with Case #3 obtaining the highest efficiency. This case is also closest to the design point. A key variable evaluated was the resultant axial velocity profile and how close it was to the distribution specified during the preliminary design of the blade. This profile is important because the radial equilibrium condition was specified for that axial velocity profile, and the next iterative loop would be to modify the blade to match the required axial velocity profile. The TE axial velocity profiles are plotted in Figure 5.16 along with the axial velocity distributions each case was designed with for comparison.

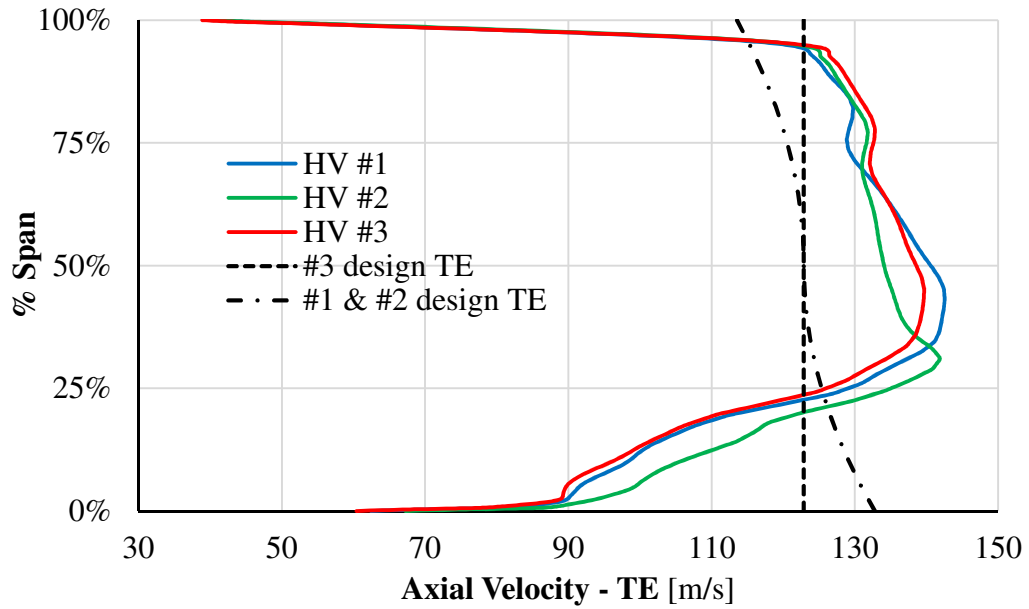


Figure 5.16 Axial velocity distributions at TE following 2D design.

Evident from the above figure, all three cases have a fairly poor trend with respect to their original design profile. The profile that resulted in the smallest average percent difference was Case #2 at 11.4%, followed by Case #1 at 13.4% and an average of 13.5% for Case #3. Given that all profiles were quite inconsistent with their design profile, Case #3 was chosen as the best to use due to its simplicity of a constant axial velocity assumption.

Examining the mass averaged turbulent kinetic energy (KE) distribution along the span at the TE of each case, it can be seen that Case #3, again, has the most favorable characteristics. Having the same peak value as Case #1 (excluding the turbulence caused by the tip vortex), the average turbulent KE in the tip region favors Case #3, leading to a smaller average value. These results are plotted in Figure 5.17 below.

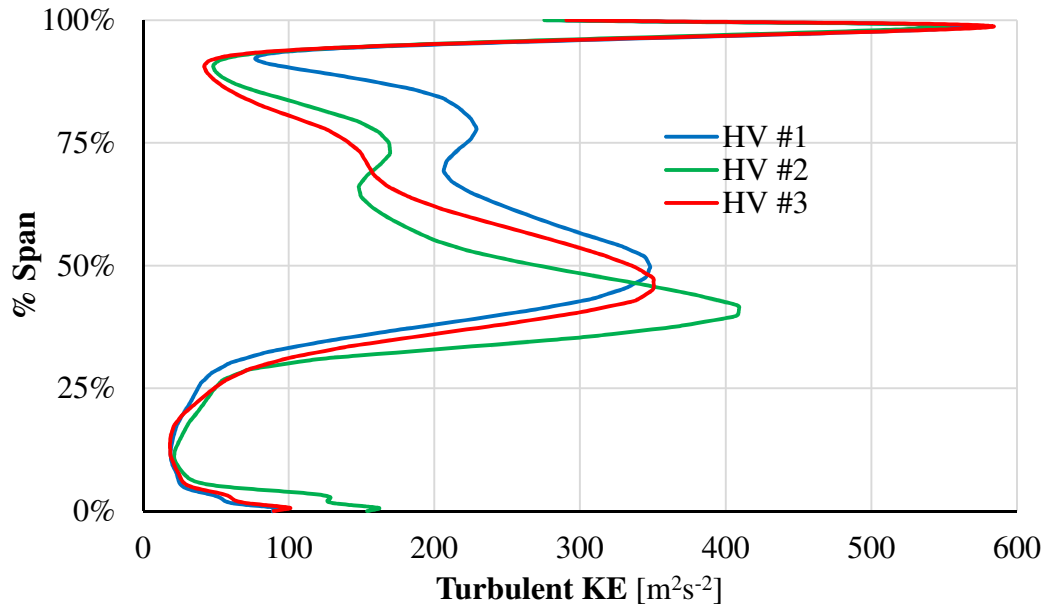


Figure 5.17 Turbulent kinetic energy distribution along the blade span.

From the above comparisons it can be seen that the most viable option for continuing the 3D design is Case #3 of the Hybrid Vortex solution. This choice also reduces the variables changed between the baseline and HV blade, since Case #3 uses the same assumption of  $rV_u = const$  for the TE design as the Free Vortex. With Case #3 selected, the full 3D design loop ‘B’ of Figure 3.4 was conducted. Henceforth, all references to “HV” or “Hybrid Vortex” not referenced as a specific case will refer to Case #3.

### 5.3.2. Axial Velocity Convergence Loop

The first integrated loop of the 3D design phase of the HV method is to match the axial velocity distribution set during the preliminary design stage. This is achieved through the manipulation of the airfoil geometry to either ‘open’ or ‘close’ the blade channel to re-distribute the flow in the desired manner. The LE axial velocity profile was the primary focus of this design stage as the LE sets the initial mass flow distribution leading into the



blade channel. The resulting axial velocity profile from the 2D design is shown in Figure 5.18 along with the profile used in the design process.

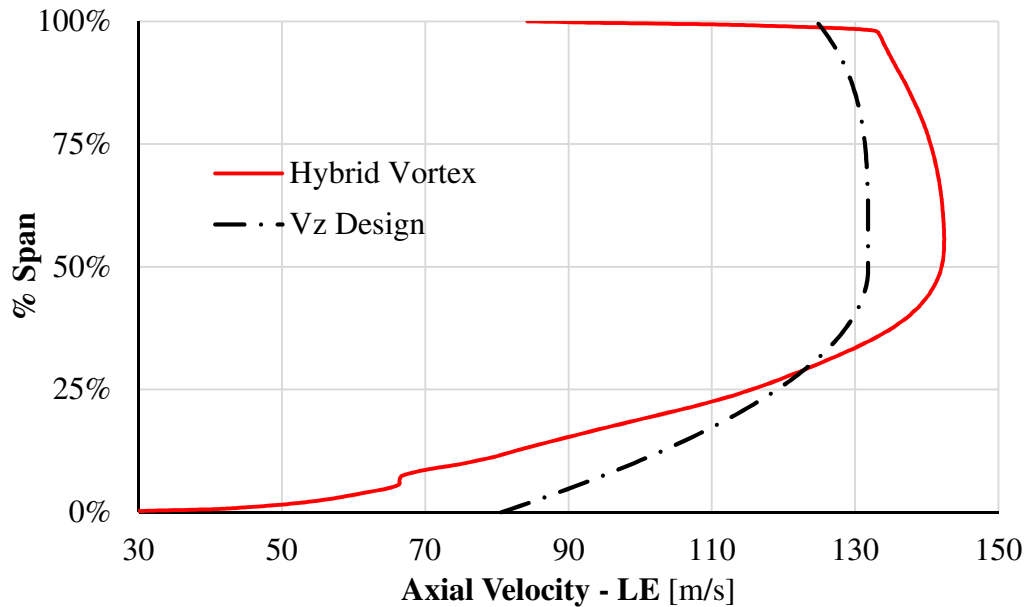


Figure 5.18 Initial axial velocity distribution from 2D design.

From this figure, it can be seen that too much mass flow is passing through the upper portions of the blade and will need to be redistributed to the lower 25% of the span. This was accomplished by two methods - ‘opening’ the lower span sections by reducing blade stagger (recall Figure 1.4) along with ‘closing’ the 50, 75 and 98% span sections by increasing the stagger angle of the blade.

Problems were encountered during this process with an inability to draw more mass flow into the hub of the Hybrid Vortex design. With the high negative stagger already imposed on the 2% span as seen in Figure 5.14, manipulation of stagger had minimal impact on the overall flow within the hub section. Increasing or decreasing stagger therefore resulted in negligible changes in the overall mass flow distribution. This is demonstrated in Figure 5.19 where stagger at 2% span is altered by nearly  $13^\circ$  with minimal

impact on the overall distribution of mass flow.

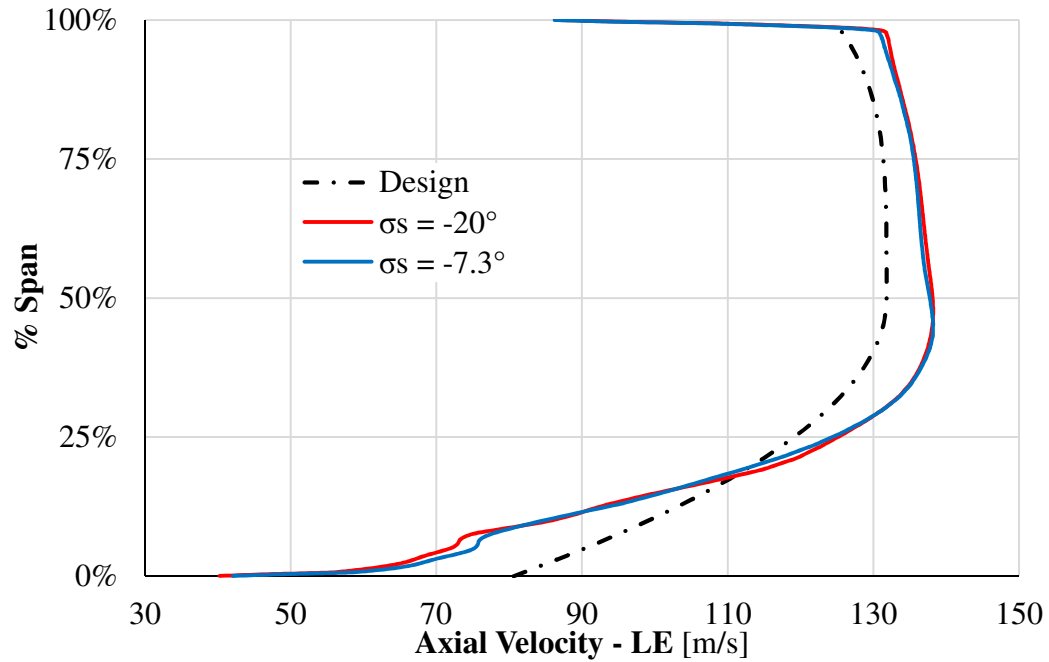


Figure 5.19 Impact of stagger variation at 2% span.

To overcome this problem, flow had to be forced down into the hub region by blocking off the upper half of the blade. This was achieved by increasing stagger in small increments across the areas of high mass flow. Utilizing this method, the following axial velocity profiles were achieved for iterations n, o, and p.

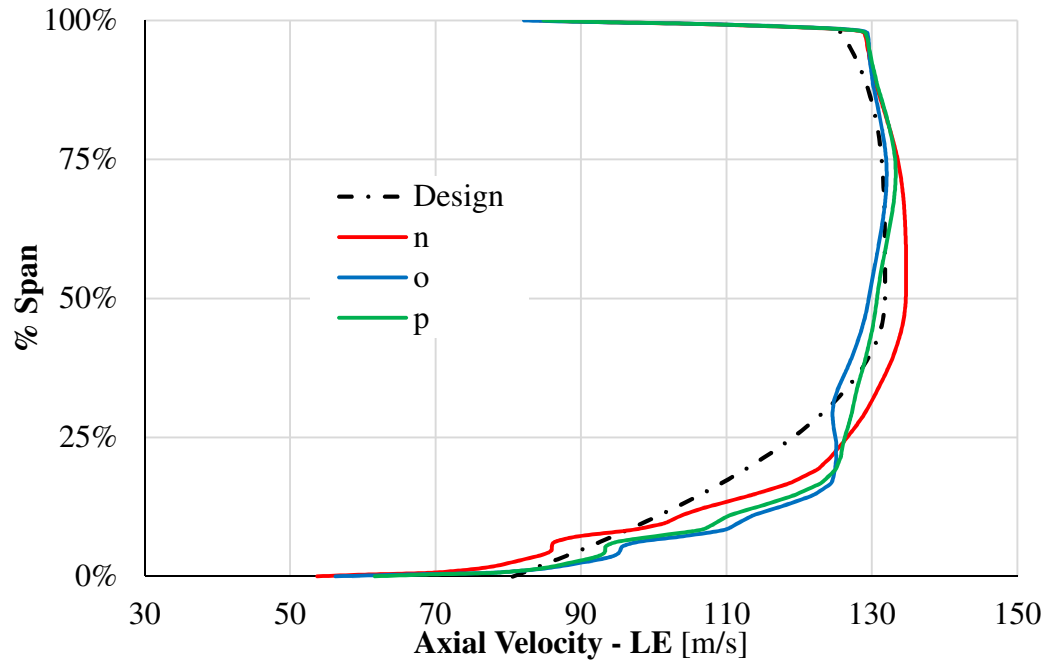


Figure 5.20 Axial velocity distribution of the closest three iterations.

The profiles achieved in Figure 5.20 came at a severe cost of the blade's overall health and performance. The increased act of forcing the flow down to the hub resulted in massive amounts of negative incidence in the entire span of the rotor, reducing efficiency and overall pressure ratio to unrealistic values. Additionally, this led to choking in the upper 75% of the blade as evident in Figure 5.21 where an isosurface is inserted into the domain for a relative Mach number of one.

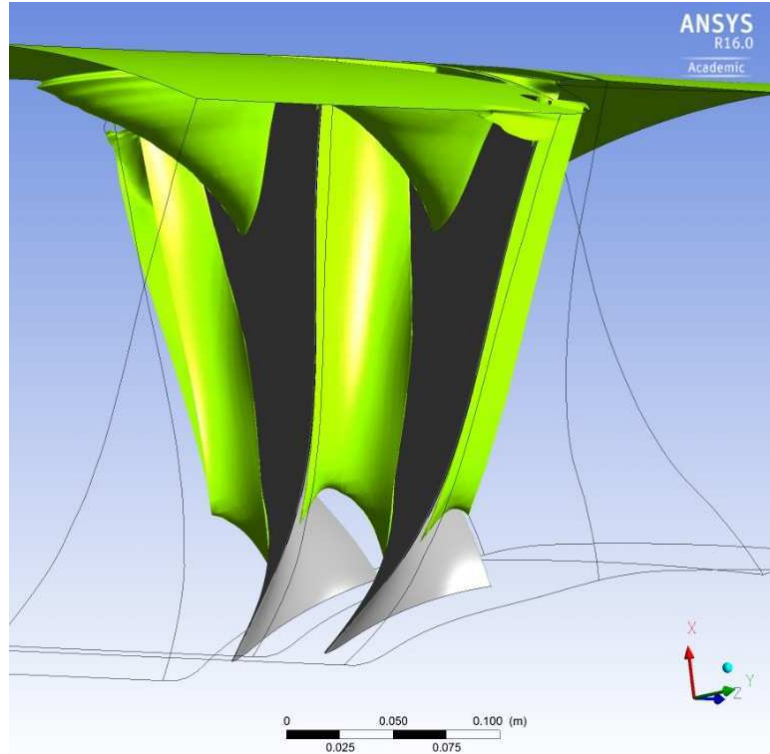


Figure 5.21 Isosurface at  $M_r = 1.0$  for design iteration ‘p’.

Unfortunately, due to the difficulties encountered as a result of this negative incidence and choking of the flow during this phase of the design loop, the axial velocity profile was not achieved even after approximately 100 design iterations and hundreds of computational hours. Without the use of an automated blade optimization program, matching of the axial velocity profile was deemed infeasible and subsequently set aside as a strict design requirement. This led into the second loop of the Hybrid Vortex method where the 3D blade optimization was conducted.

### 5.3.3. 3D Blade Optimization

The final step in the Hybrid Vortex design process consisted of an optimization process to account for the change in flow physics when transitioning from 2D to 3D flow field assessment. A number of different parameters were focused upon for optimization from local incidence to Mach profiles. Only 3D design was conducted during this loop, meaning every change to the blade geometry required a full 3D simulation to be conducted. Observing the simulation residuals and monitor points, it was determined that approximately 500 iterations were required to obtain an acceptable solution for these quick design runs. The mass flow monitor residual, Figure 5.22, demonstrates the acceptable level of convergence achieved by 500 iterations.

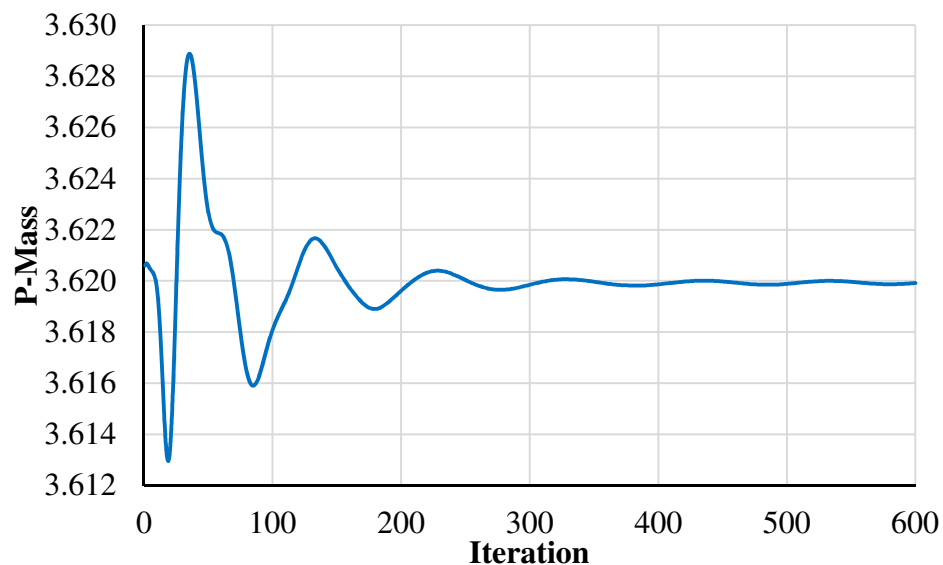


Figure 5.22 P-Mass residual monitor.

The main concern of the 2D blade observed in the results of the 3D CFD evaluation was the presence of negative incidence along a substantial portion of the LE. This negative incidence was remedied incrementally, through the reduction of stagger angle along with slight manipulation of the LE metal angles. A sample of the pre- and post-3D design

sections are presented in Figure 5.23 through Figure 5.26, with the remaining sections located in Appendix J.

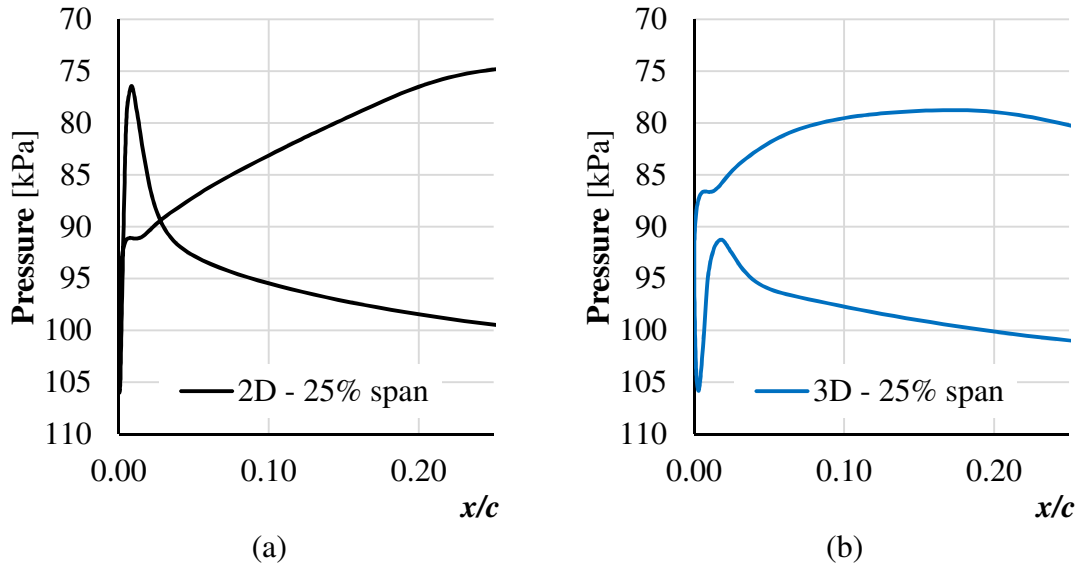


Figure 5.23 LE incidence comparison before (a) and after (b) 3D design at 25% span.

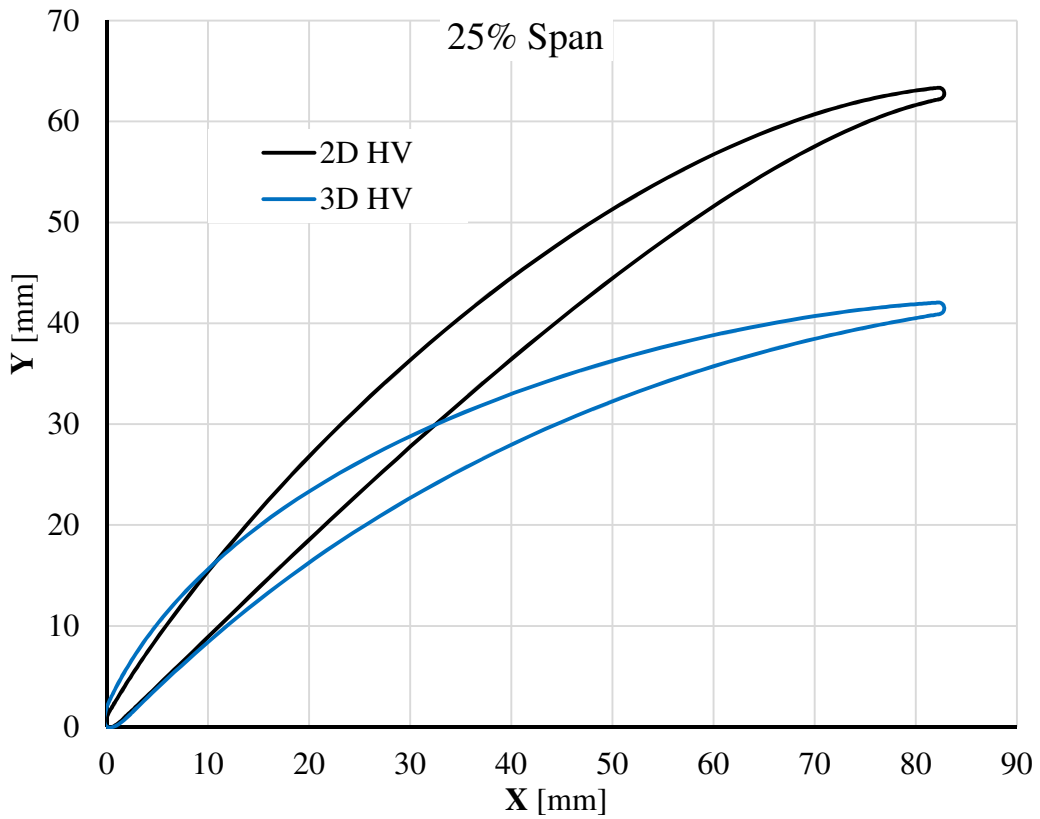


Figure 5.24 Redesigned HV airfoil section at 25% span.

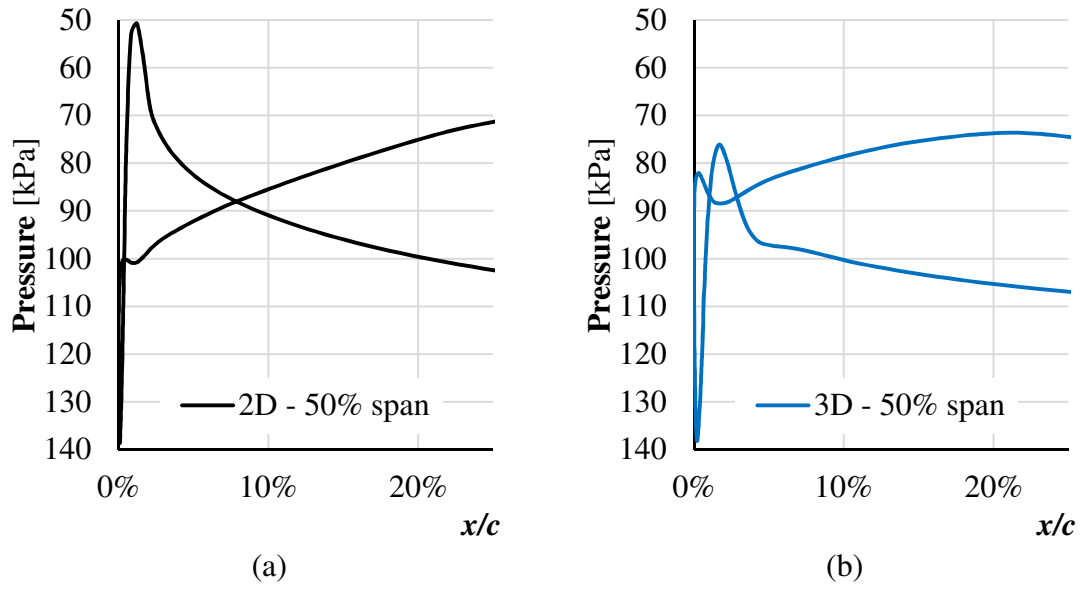


Figure 5.25 LE incidence comparison before (a) and after (b) 3D design at 50% span.

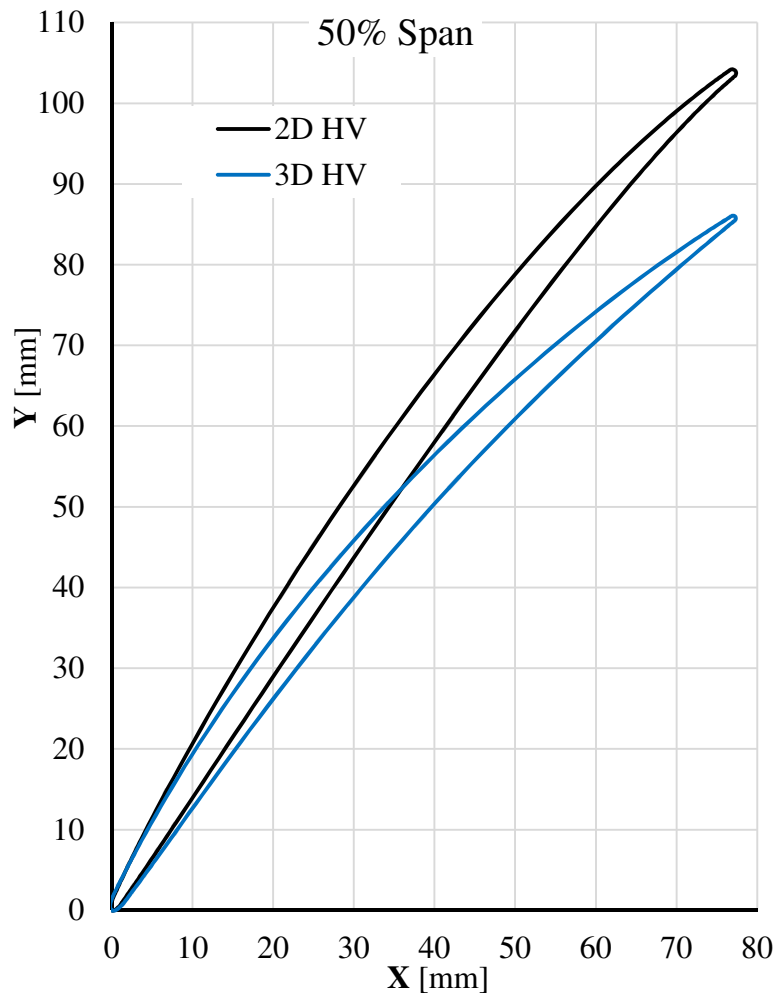


Figure 5.26 Redesigned HV airfoil section at 50% span.

The 3D optimization brought about many improvements in the flow through the cascade, as clearly demonstrated by the large reduction in turbulent kinetic energy along the TE of the blade, shown in Figure 5.27.

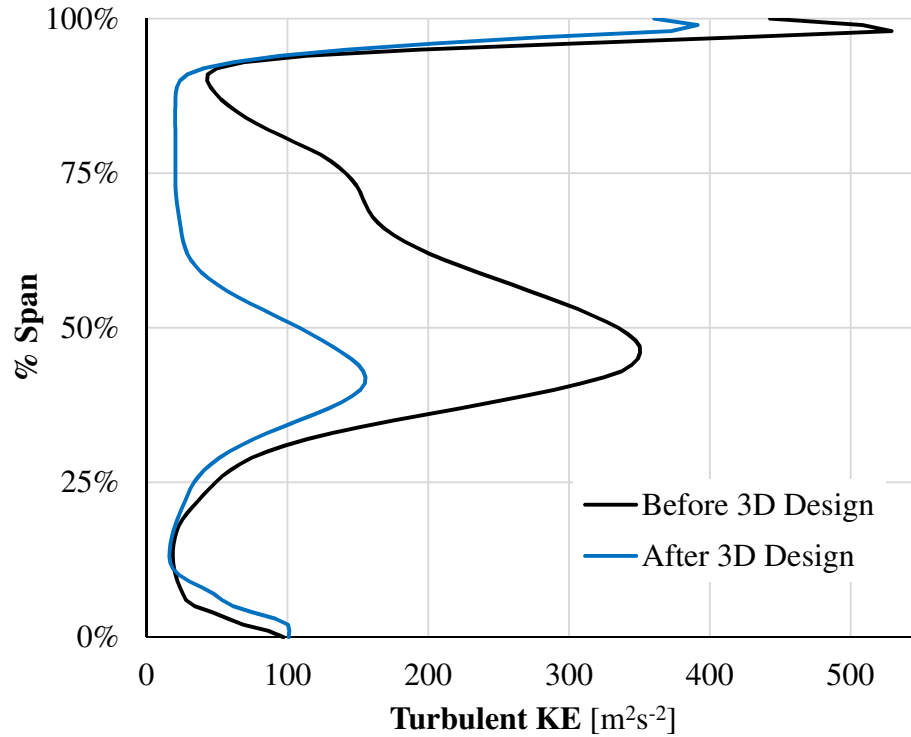


Figure 5.27 Turbulent kinetic energy trends at the TE before and after optimization.

The final performance parameters of the optimized Hybrid Vortex blade are shown in Table 5.4 where an overall efficiency increase of 3.6% was obtained.

Table 5.4 Final performance parameters of optimized HV blade.

<b>Rotor</b>	<b>FV</b>	<b>HV Optimized</b>
<b>Mass Flow [kg/s]</b>	79.70	79.70
<b>Pressure Ratio</b>	1.302	1.307
<b>Isentropic efficiency</b>	94.45%	95.23%



#### 5.4. Observed Flow Features

As stated previously in Section 5.2.1, the hub design of the HV is an area of great interest due to the significant geometric changes brought about by the new HV equations. As a result, the lower portion of the blade became a focal point in the analysis of the new method.

Upon initial visual inspection of the streamlines through the hub of the HV blade, it became evident that the flow through the HV blade exhibited some complex flow features. Vorticity has been introduced into the flow at the hub, resulting in a ‘folding’ of the flow as it moved through the channel. Figure 5.28 illustrates this flow characteristic where streamlines are seeded at the LE, from 0-5% span to capture the flow through the hub.

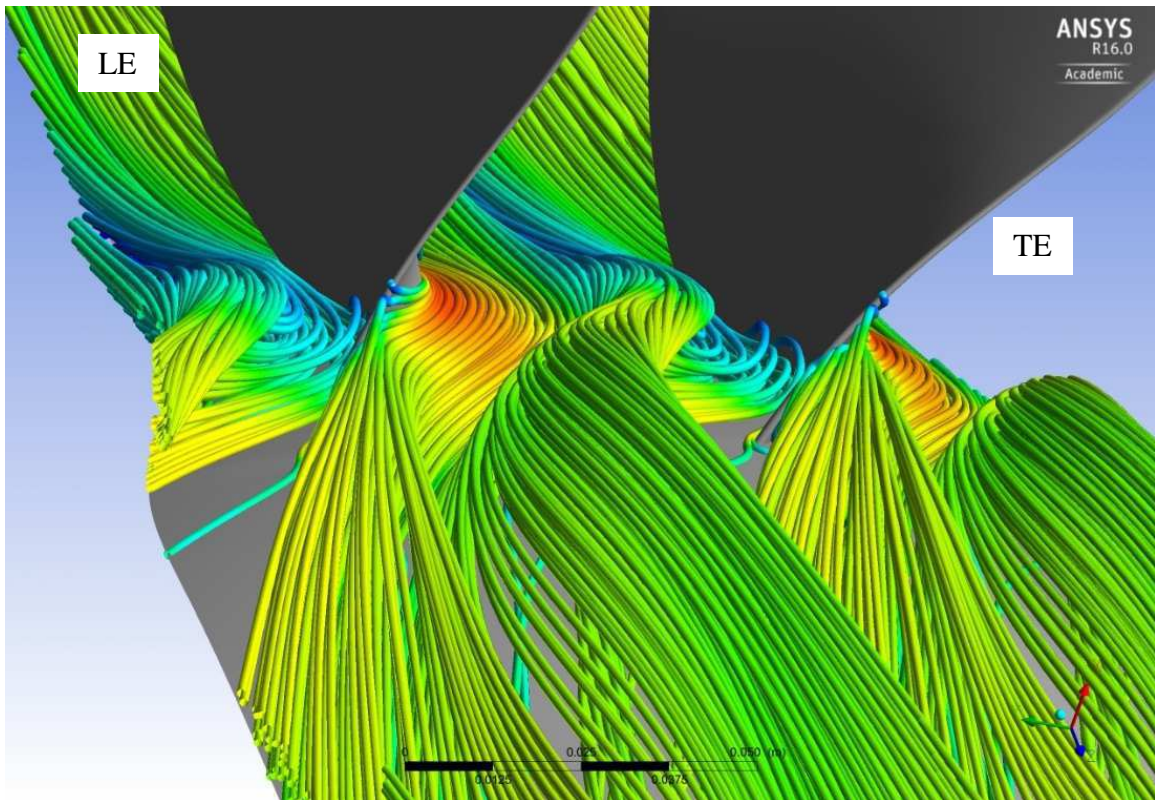


Figure 5.28 Hub streamlines observed from the TE of the HV blade.

To obtain a clear picture of the flow around the hub, surface streamlines were plotted on the suction surface of both the HV and the FV blades. As mentioned previously, due to the inability to match the axial velocity profiles specified in the design, it can be seen that the centrifugal force imposed on the flow by the rotating cascade overpowers the balance of forces in the hub of the blade. However, the effects of this imbalance are noticeably less for the HV than they are in the FV. Figure 5.29 clearly shows a unique attribute of the HV where the blade is doing a better job maintaining radial equilibrium through the lower 10% of the span before the force imbalance dominates the flow.

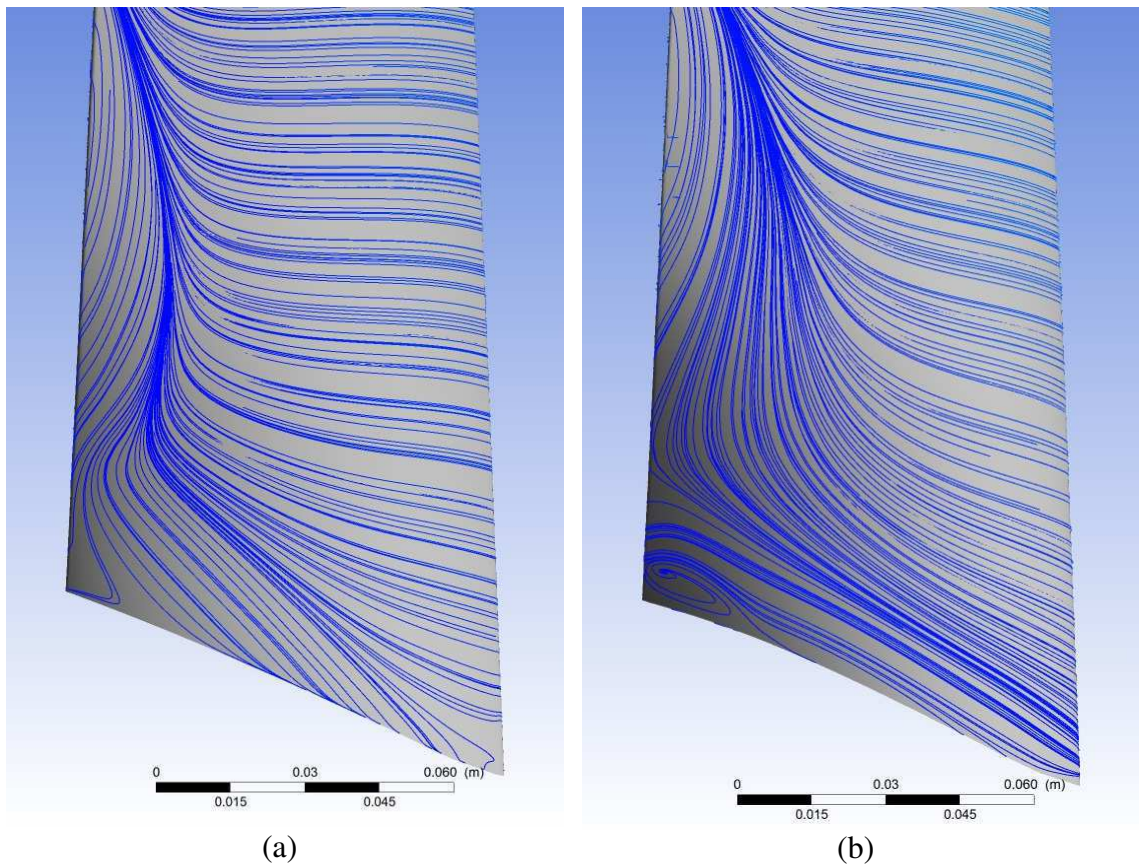


Figure 5.29 Surface streamlines on the hub, suction surface of the FV (a) and HV (b).

This improvement in radial equilibrium is also demonstrated in Figure 5.30 where the radial velocity component has been significantly decreased (approximately 37%) at the hub of the blade compared to the baseline FV.

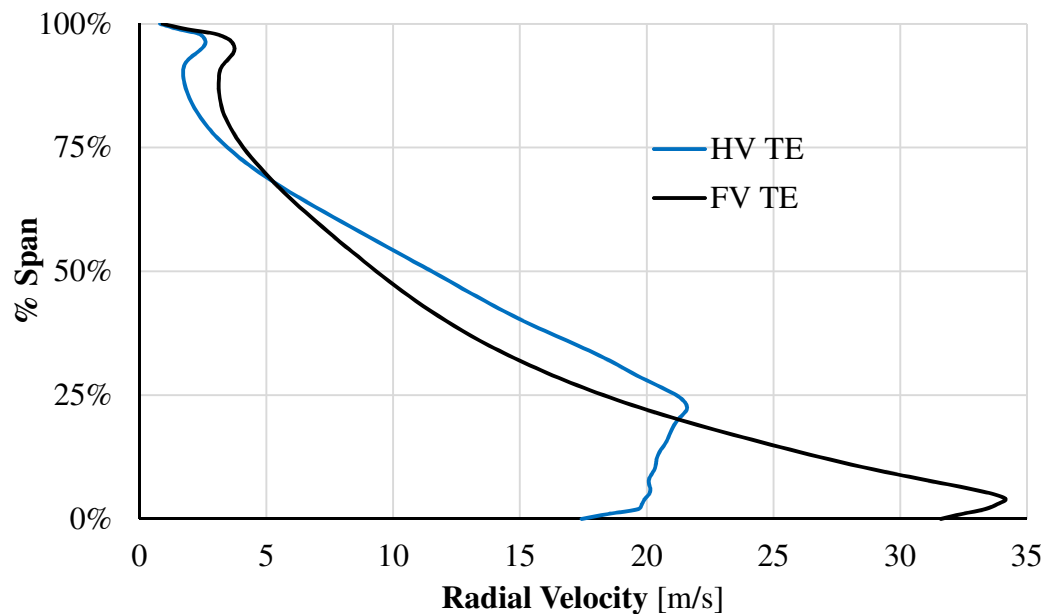


Figure 5.30 Radial velocity comparison at the TE of the HV and baseline blades.

Another beneficial feature of the hub design of the HV is its ability to turn the flow. We can observe that the theory discussed in the final paragraph of Section 5.2.1 is relatively correct. The mass averaged relative flow angle leaving the blade cascade is only  $3.2^\circ$  less than the metal angle of the blade, a very small deviation angle for a hub section with such a large amount of turning. To put this in perspective, Table 5.5 compares these values for the FV and HV blades with the FV having an additional  $10.5^\circ$  of deviation between the relative flow angle and the TE metal angle.

Table 5.5 Relative metal and flow angles at the TE, 2% span.

	$\beta_{TE,metal}$	$\beta_{TE,flow}$	Deviation
<b>Free Vortex</b>	20.7°	7.0°	13.7°
<b>Hybrid Vortex</b>	34.5°	31.3°	3.2°

### 5.4.1. Off-Design Behavior

The overall goal of developing the new Hybrid Vortex method is to achieve a wider operating range while still matching performance criteria, as stated in the introduction. Thus, both the baseline and Hybrid Vortex blades were run at various points at off-design. The design characteristic was obtained for both blades with interesting results, displayed in Figure 5.31.

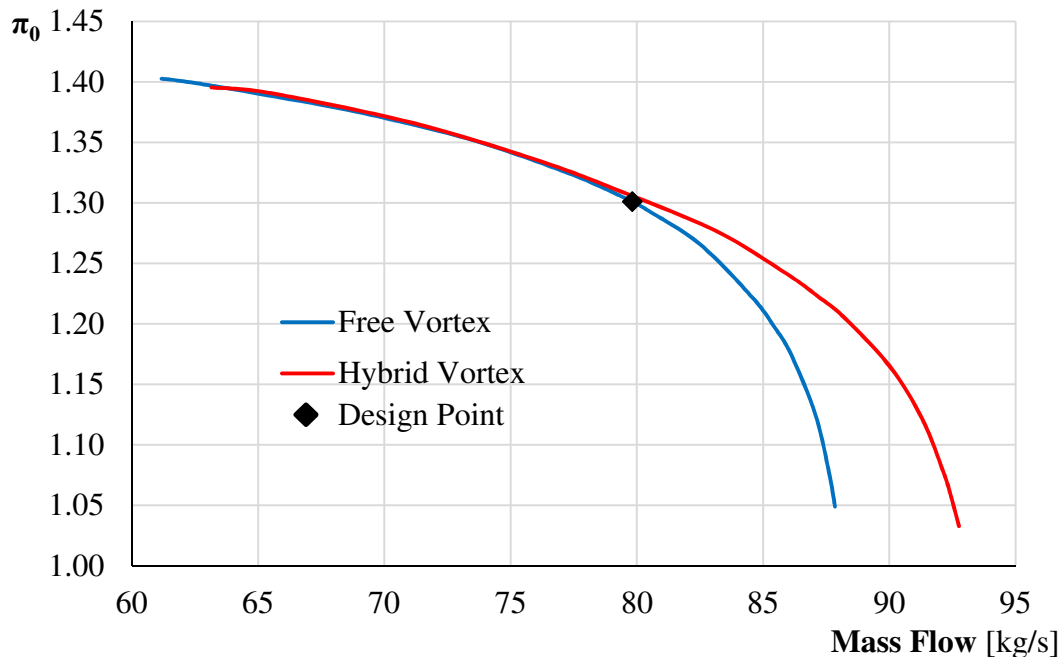


Figure 5.31 Design rotor speed characteristics for the FV and HV blades.

The initial evaluation indicated that the goal of enhancing Surge Margin with the Hybrid Vortex solution might have failed. However, upon further inspection, a number of redeeming factors come from the Hybrid Vortex design that show great potential. The most

obvious of these factors is the extended choking point of the rotor. This increase in choking mass flow over the FV design is larger than the decrease in mass flow at the surge point between the two blades. The mass flow operating envelope can be calculated for both blade designs and is given in Table 5.6.

Table 5.6 Mass flow operating range comparison between the FV and HV blades.

	$\dot{m}_{\text{choke}}$ [kg/s]	$\dot{m}_{\text{surge}}$ [kg/s]	$\dot{m}_{\text{choke}} - \dot{m}_{\text{surge}}$ [kg/s]
<b>Free Vortex</b>	87.85	61.18	26.67
<b>Hybrid Vortex</b>	92.76	63.15	29.61
		$\Delta\dot{m}_{\text{op}}$	+2.94 (+11%)

This increase of 2.9 kg/s amounts to a substantial increase (11%) in operational mass flow range over the Free Vortex method. Plotting the efficiency of the design characteristics for both blades, an interesting discovery was made in relation to the HV blade. It can be seen in Figure 5.32 that the efficiency curve is also translated towards the higher mass flow conditions.

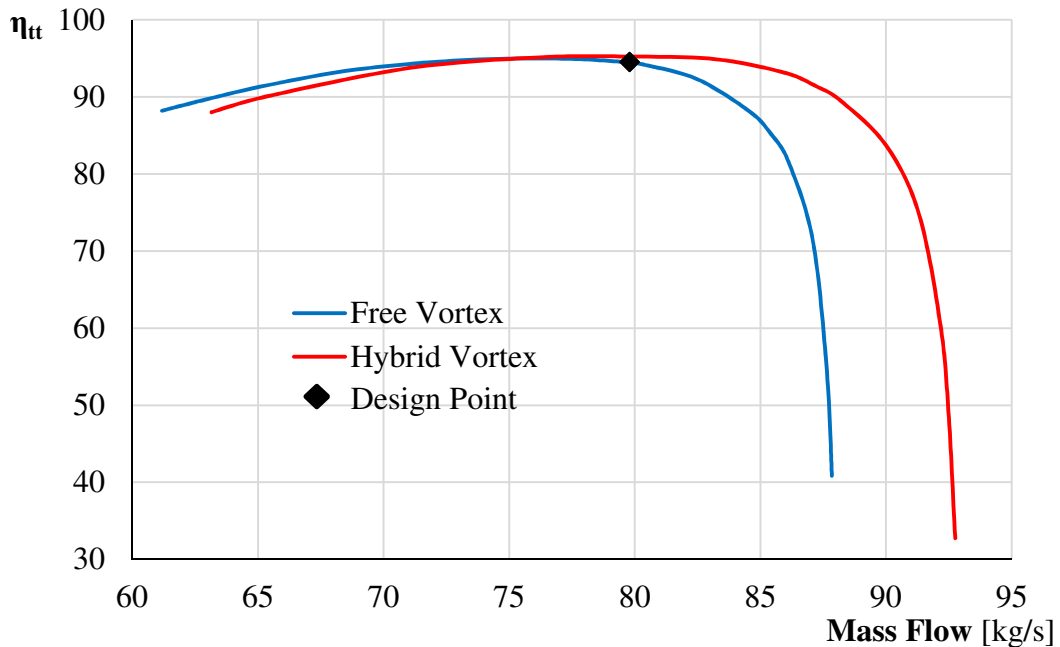


Figure 5.32 Isentropic efficiency for the FV and HV blades.

The extended operating range and peak efficiency trends of the HV blade tend to pose the question of whether or not the current HV blade is designed at its peak performance. The goal of this work is to extend the Surge Margin of a compressor using the HV design methodology. The extended choking margin is of little importance in compressors, as discussed in Section 1.3. With this in mind, theoretically the compressor map can be translated through redesigning the blade while maintaining the Hybrid Vortex methodology. The characteristic would be translated to match the choking mass flow of the FV blade while maintaining the design point pressure ratio and mass flow. This redesign has the potential to produce the hypothetical map illustrated in Figure 5.33 where the HV map has been translated 4.9 kg/s to the left and has maintained total pressure ratio – only a small increase of an additional 0.04 is observed.

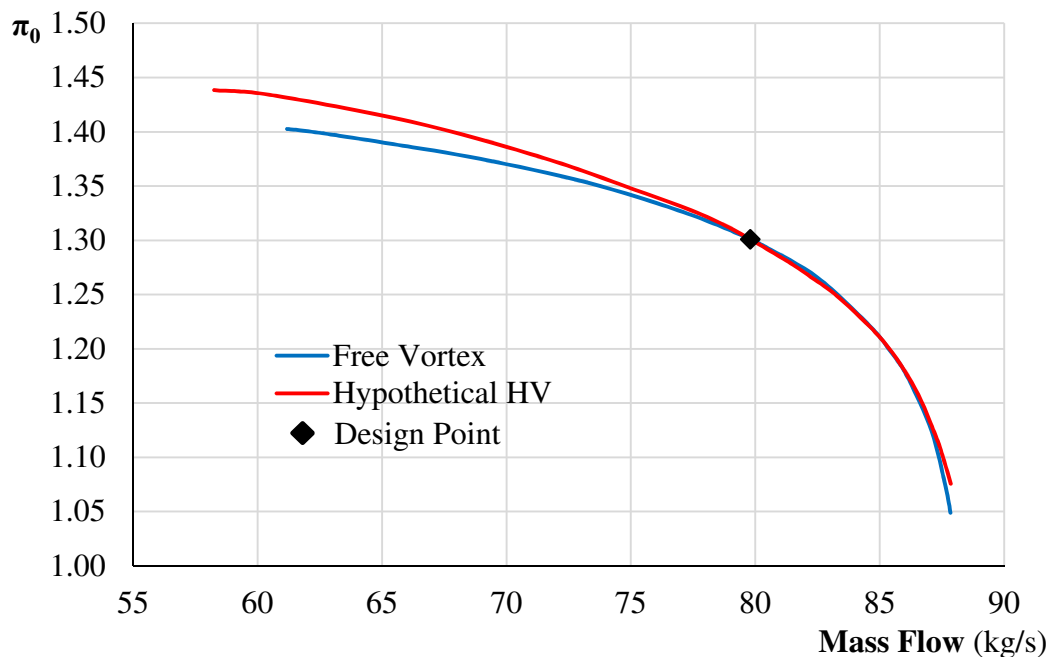


Figure 5.33 Hypothetical Hybrid Vortex characteristic following redesign.



Figure 5.33 shows great potential for the HV design methodology to enhance not only the operating mass flow range, but also to increase the surge margin of the blade when compared to the Free Vortex design methodology. Moreover, this does not take into consideration that the FV blade began with a slight advantage of negative incidence along most of the blade span at design, leading to a fictitious extension of the surge margin of the blade. With the additional ~3 kg/s in mass flow operating range, a buffer is already built into the Hybrid Vortex to allow for slight changes in the characteristic behavior following a redesign to translate the map to the favorable position shown above.

To quantify this potential of the hypothetical characteristic presented in Figure 5.33, let a simplified measure of the surge margin be defined by the following equation:  $SM = \frac{\pi_{0,surge} - \pi_{0,design}}{\pi_{0,design}} \times 100$ . Using the total pressure ratio at the design and surge points on the same characteristic will result in a simplified relationship to quantify the potential improvement. Using this equation and the values of the hypothetical map presented in Figure 5.33, the values of the surge margin were computed and are presented in Table 5.7.

Table 5.7 Hypothetical Surge Margin comparison.

	<b>Free Vortex</b>	<b>Hybrid Vortex</b>
$\pi_{0,surge}$	1.4026	1.4384
$\pi_{0,design}$	1.3019	1.3066
<b>SM</b>	7.73%	10.09%
	$\frac{SM_{HV}}{SM_{FV}} - 1 =$	+30.5%

With a calculated increase in surge margin by 30.5% from the hypothetical Hybrid Vortex characteristic, the potential for surge margin enhancement through the proposed vortex theory appears certain, leaving plenty of room for additional optimization and improvements as it is translated to the desired operating point shown in Figure 5.33.



## 6. Conclusion

A new Hybrid Vortex theory and design method for preliminary axial compressor design has been presented. This was achieved from the analytical derivation of the radial equilibrium equations, through to the generation of the design characteristic line of the compressor map using full 3D CFD.

Due to the common method of design optimization used in the industry today, compressor design has nearly reached an asymptote in performance. To break this stalemate, a modern approach has been applied to the fundamental building blocks of compressor design by revisiting the radial equilibrium equations. As a result of incorporating quasi-viscous effects into the preliminary design phase, unique blade designs more accurately tailored for the flow conditions experienced during operation can be designed, leading to a reduction in optimization time later in the design process.

The Hybrid Vortex theory uses a set axial velocity profile obtained from either analytical relations or exported from a baseline blade design (as completed within this study). The corresponding circumferential velocity profile is then computed from the new method and used to design the blade; i.e., it is used to alter the velocity triangles. To assess the Hybrid Vortex's performance, the well-known and proven Free Vortex theory was used to generate a baseline design case.

Three initial approaches were taken in applying the Hybrid Vortex theory to blade design. Following 2D design the final design method retained the TE, i.e., the TE velocity triangles were computed using the Free Vortex theory, applying the new Hybrid Vortex solution to the LE only.

Significant changes in the hub geometry occurred after implementation of the

Hybrid Vortex method. The hub was restaggered by  $20^\circ$  and a redesign resulted in numerous beneficial flow features. The Hybrid Vortex method increases the overall efficiency of the rotor, reduces the flow deviation at the hub by  $10^\circ$ , and increases the mass flow operating range by 11%.

The potential for the Hybrid Vortex theory to drastically enhance the surge margin within a compressor is very promising. With further re-design and optimization of the blade design, the surge margin has the potential of greatly increasing, with the hypothetical redesign producing an increase of 30.5%.

## 7. Recommendations

Many issues were encountered throughout the study that required multiple redesigns of each blade. Ideally, an automated blade generation and optimization program would have been used to speed up the overall design process, along with ensuring complete consistency between every blade design. By manually altering the airfoil shapes, slight inconsistencies between designs are unavoidable. This would ensure that the only factors leading to improvements in the performance are purely obtained from the new vortex solution. In addition, an automated process that could conduct the 3D design loop for matching the designed axial velocity profile could lead to a converged solution that was unobtainable in the current study.

It is highly recommended to employ a cluster or super computer to speed up the generation of points for the characteristic. The use of the university's cluster "Rigel" proved invaluable.

Following the refinement of the Hybrid Vortex design method, an analytical model for approximating axial velocity distribution would be ideal to speed up the design process significantly, especially when no baseline case is present for exporting the LE velocity profile. This would be a necessity should a design tool be made that incorporates the Hybrid Vortex model.

The next step in the analysis of the Hybrid Vortex (following refinement of the blade) would be a study into rotor-stator interactions (or multiple stages) when using this new vortex solution. Certain unique flow conditions exist in the new blade that could either be beneficial or detrimental to the performance through multi-stage components. For this study, a simplified, linearly tapering annulus would be recommended.

## REFERENCES

- Altuntas, O. (2014, May). Designation of Environmental Impacts and Damages of Turbojet Engine: A Case Study with GE-J85. *Atmosphere*, 5(2), 307-323.
- Brun, K., & Kurz, R. (2005). Gas Turbine Life Limiting Effects of Inlet and Interstage Water Injection. In J. Burnett (Ed.), *34th Turbomachinery Symposium*, (pp. 45-52). Houston. Retrieved 2016
- Carmichael, A. D., & Horlock, J. H. (1957). *Actuator Disc Theories Applied to the Design of Axial Compressors*. London: Ministry of Supply: Aeronautical Research Council.
- Chima, R. V. (1999, March 1). GRAPE 2-D Grid Generator for Turbomachinery. 10. Cleveland, Ohio, USA: NASA Glenn Research Center. Retrieved 2015
- Chima, R. V. (1999, March 1). RVCQ3D - Rotor Viscous Code Quasi-3-D. 18. Cleveland, Ohio, USA: NASA Glenn Research Center. Retrieved 2015
- Coles, D. E. (1969). *Turbulent Boundary Layers in Pressure Gradients*. United States Air Force, Office of Scientific Research. Santa Monica: The RAND Corporation. Retrieved 2015
- Cornelius, C., Biesinger, T., Galpin, P., & braune, A. (2014, June). Experimental and Computational Analysis of a Multistage Axial Compressor Including Stall Prediction by Steady and Transient CFD Methods. (R. Bunker, Ed.) *Journal of Turbomachinery*, 136(6), 061013-1 - 061016-12.
- Dixon, S. L., & Hall, C. A. (2010). *Fluid Mechanics and Thermodynamics of Turbomachinery* (6 ed.). Boston: Elsevier.
- Gallimore, S. J. (1999, May 1). Axial flow compressor design. (J. W. Chew, Ed.) *Journal of Mechanical Engineering Science*, 213(5), 437-449. Retrieved 2015
- Hah, C., & Loellbach, J. (1999, January). Development of Hub Corner Stall and its Influence on the Performance of Axial Compressor Blade Rows. (H. A. Kidd, Ed.) *Journal of TurboMachinery*, 121(1), 67-77. Retrieved 2015
- Hill, P., & Peterson, C. (1992). *Mechanics and Thermodynamics of Propulsion* (Second Edition ed.). Reading, Massachusetts: Addison-Wesley Publishing Company. Retrieved 2015
- Horlock, J. H. (1958). *Axial Flow Compressors, Fluid Mechanics and Thermodynamics*. London: Butterworths Scientific Publications. Retrieved 2015

- Horlock, J. H., & Hoadley, D. (1972). *Calculation of the Annulus Wall Boundary Layers in Axial Flow Turbomachines*. London: Ministry of Defense, Aeronautical Research Council. Retrieved 2015
- Larson, W. D. (1975). *Improvements to Simple Radial Equilibrium Preliminary Turbine Design*. (Masters Thesis), Massachusetts Institute of Technology, Ocean Engineering, Boston. Retrieved 2015
- Molinari, M., & Dawes, W. N. (2006, June 1). Review of evolution of compressor design process and future perspectives. (J. W. Chew, Ed.) *Journal of Mechanical Engineering Science*, 220(6), 761-771. Retrieved 2015
- Oates, G. C. (1988). In J. S. Przemieniecki (Ed.), *Aerothermodynamics of Gas Turbine and Rocket Propulsion* (pp. 301-305). Washington DC: American Institute of Aeronautics and Astronautics. Retrieved 2015
- Powell, J. D. (2005). *Impact of Leading-Edge Orientation and Shape on Performance of Compressor Blades*. Thesis, Naval Postgraduate School, Monterey. Retrieved 2015
- Rolls-Royce plc. (2014). [Photograph]. Retrieved from <https://www.flickr.com/photos/rolls-royceplc/15354297599/in/album-72157644584413758/>
- Smallen, D. (2015, December 15). 3rd Quarter 2015 Airline Financial Data. Washington, District of Columbia. Retrieved 2 18, 2016, from [http://www.rita.dot.gov/bts/press\\_releases/bts056\\_15](http://www.rita.dot.gov/bts/press_releases/bts056_15)
- Ward, T. A. (2010). In *Aerospace Propulsion Systems* (p. 247). Singapore: John Wiley & Sons.
- Wilson, D. G., & Korakianitis, T. (1998). In M. Horton (Ed.), *The Design of High-Efficiency Turbomachinery and Gas Turbines* (2nd ed., pp. 263-279). Upper Saddle River, New Jersey: Prentice-Hall Inc. Retrieved 2016
- Wu, C.-H. (1952). *A general theory of three-dimensional flow in subsonic and supersonic turbomachines of axial-, radial- and mixed-flow types*. Lewis Flight Propulsion Laboratory. Washington: National Advisory Committee for Aeronautics. Retrieved 12 3, 2015
- Wu, C.-H., & Wolfenstein, L. (1950). *Application of Radial-Equilibrium Condition to Axial-Flow Compressor and Turbine Design*. Washington D.C.: National Advisory Committee for Aeronautics. Retrieved 2015

## A. Radial Equilibrium Derivations

### Force Balance

Referencing the infinitesimal fluid element shown in Figure 2.2, a force balance must occur to ensure the centripetal forces experienced as swirl is introduced into the flow does not cause the flow to centrifuge out of the cascade. To counteract this, a radial pressure gradient is introduced that balances the forces on the fluid element. To do this, we start with the Navier-Stokes Equations in cylindrical coordinates.

Radial-momentum equation

$$\rho \left[ \frac{\partial V_r}{\partial t} + V_r \frac{\partial V_r}{\partial r} + \frac{V_u}{r} \frac{\partial V_r}{\partial \theta} + V_z \frac{\partial V_r}{\partial z} - \frac{V_u V_u}{r} \right] = -\frac{\partial P}{\partial r} + \mu \left( \nabla^2 V_r - \frac{V_r}{r^2} - \frac{2}{r^2} \frac{\partial V_u}{\partial \theta} \right) + f_r$$

The following assumptions are made:

$$\text{Steady Flow} \quad \rightarrow \quad \frac{\partial}{\partial t} = 0 \quad (i)$$

$$\text{Axisymmetric Flow} \quad \rightarrow \quad \frac{\partial}{\partial \theta} = 0 \quad (ii)$$

$$\text{Infinitely long cylinder} \quad \rightarrow \quad \frac{\partial}{\partial z} = 0 \quad (iii)$$

$$\text{No radial velocity} \quad \rightarrow \quad V_r = 0 \quad (iv)$$

$$\text{No body forces} \quad \rightarrow \quad f_r = f_\theta = f_z = 0 \quad (v)$$

The r-momentum equation simplifies to,

$$\boxed{\frac{\partial P}{\partial r} = \rho \frac{V_u^2}{r}} \quad (2.1)$$

## Simple Radial Equilibrium

Starting from the stagnation enthalpy (assuming  $V_r = 0$ )

$$h_0 = h + \frac{1}{2}(V_u^2 + V_z^2)$$

$$\frac{dh_0}{dr} = \frac{dh}{dr} + V_z \frac{dV_z}{dr} + V_u \frac{dV_u}{dr} \quad (a)$$

Using the following thermodynamic relationship:

$$Tds = dh - \frac{1}{\rho} dP$$

$$T \frac{ds}{dr} = \frac{dh}{dr} - \frac{1}{\rho} \frac{dP}{dr}$$

Rearranging,

$$\frac{dh}{dr} = T \frac{ds}{dr} + \frac{1}{\rho} \frac{dP}{dr} \quad (b)$$

Substituting Equations (2.2) and (b) into (a) we obtain,

$$\frac{dh_0}{dr} = T \frac{ds}{dr} + \frac{V_u^2}{r} + V_z \frac{dV_z}{dr} + V_u \frac{dV_u}{dr}$$

Simplifying,

$$\frac{dh_0}{dr} - T \frac{ds}{dr} = V_z \frac{dV_z}{dr} + \frac{V_u}{r} \frac{d(rV_u)}{dr} \quad (c)$$

The following assumptions are made:

$$\text{Constant } h_0 \text{ with radius} \quad \rightarrow \quad \frac{\partial h_0}{\partial r} = 0 \quad (i)$$

$$\text{Constant } s \text{ with radius} \quad \rightarrow \quad \frac{\partial s}{\partial r} = 0 \quad (ii)$$

Thus equation (c) reduces to the Simple Radial Equilibrium Equation:

$$\boxed{\frac{d}{dr} (V_z)^2 = -\frac{1}{r^2} \frac{d}{dr} (rV_u)^2} \quad (2.2)$$



Table A.1 Vortex solutions (Horlock, 1958)

<i>Method of Design</i>	<i>Work variation with radius</i>	<i>Tangential velocity distribution</i>	<i>Axial velocity distribution</i>	<i>Reaction distribution with radius</i>	<i>Radial equilibrium</i>
<i>A. Two-dimensional</i>	Supposed constant	Supposed constant	Supposed constant	Supposed constant	Ignored
<i>B. Free vortex</i>	Constant	$V_{ur} = \text{constant}$	Constant	Increases with radius	Yes
<i>C. Constant reaction (without equilibrium)</i>	Supposed constant	$V_u = ar^n \pm \frac{b}{r}$	Supposed constant	Supposed constant	Ignored
<i>D. Half vortex</i>	Supposed constant	Arithmetic mean of free vortex and constant reaction distributions	Supposed constant	Not far from constant	Ignored
<i>E. 'Constant <math>\alpha_2</math>'</i>	Supposed constant	Fixed by the condition that $V_{u2}$ (entry to stator) = (constant) $V_{u1}$ (entry to rotor) = $a - b/r$	Supposed constant	Not far from constant	Ignored
<i>F. Constant reaction</i>	Constant	$V_u = ar^n \pm \frac{b}{r}$	From radial equilibrium	Constant	Yes
<i>G. Forced vortex</i>	Increases with $r^2$	$V_u$ proportional to $r$	From radial equilibrium	Varies with radius	Yes
<i>H. 'Exponential'</i>	Constant	$V_u = a \pm \frac{b}{r}$	From radial equilibrium	Varies with radius	Yes

## B. Hybrid Vortex Derivation

Let the following general equation define the axial velocity variation with radius,  $r$ , in the Vertex Form of a polynomial

$$V_z(r) = -A(r - r_m)^B + V_{z,m} \quad (3.1)$$

Where:  $A, B \equiv$  constants dependent on annulus size and H/T  
 $r_m \equiv$  mid radius  
 $V_{z,m} \equiv$  Axial velocity at the midpoint

Define the Simple Radial Equilibrium Equation (SREE):

$$\frac{d}{dr} (V_z)^2 = -\frac{1}{r^2} \frac{d}{dr} (rV_u)^2 \quad (2.2)$$

Starting with the LHS of Equation (2.2),

$$\begin{aligned} \frac{d}{dr} (V_z)^2 &= \frac{d}{dr} [-A(r - r_m)^B + V_{z,m}]^2 \\ &= \frac{d}{dr} [A^2(r - r_m)^{2B} - 2AV_{z,m}(r - r_m)^B + V_{z,m}^2] \\ &= 2A^2B(r - r_m)^{2B-1}(1) - 2ABV_{z,m}(r - r_m)^{B-1}(1) + 0 \end{aligned}$$

Thus,

$$\frac{d}{dr} (V_z)^2 = 2AB[A(r - r_m)^{2B-1} - V_{z,m}(r - r_m)^{B-1}] \quad (a)$$

Substituting (a) into (2.2),

$$2AB[A(r - r_m)^{2B-1} - V_{z,m}(r - r_m)^{B-1}] = -\frac{1}{r^2} \frac{d}{dr} (rV_u)^2$$

Multiplying by  $-r^2$  and rearranging,

$$\frac{d}{dr} (rV_u)^2 = 2AB[V_{z,m}r^2(r - r_m)^{B-1} - Ar^2(r - r_m)^{2B-1}]$$

Integrate both sides with respect to  $r$

$$(rV_u)^2 + const. = 2AB \left[ V_{z,m} \int r^2 (r - r_m)^{B-1} . dr - A \int r^2 (r - r_m)^{2B-1} . dr \right]$$

Perform the integration,

$$(rV_u)^2 = 2AB \left[ V_{z,m} \frac{(r - r_m)^B (2r_m^2 + 2r_m Br + B(B + 1)r^2)}{B(B + 1)(B + 2)} \dots \right. \\ \left. - A \frac{(r - r_m)^{2B} (2r_m^2 + 2r_m Br + B(2B + 1)r^2)}{2B(B + 1)(2B + 2)} \right] + k$$

Where k is the combined constant from all integrations

$$(rV_u)^2 = \frac{2AB(r - r_m)^B}{B(B + 1)} \left[ V_{z,m} \frac{(2r_m^2 + 2r_m Br + B(B + 1)r^2)}{(B + 2)} \dots \right. \\ \left. - A \frac{(r - r_m)^B (2r_m^2 + 2r_m Br + B(2B + 1)r^2)}{2(2B + 2)} \right] + k$$

Simplifying and rearranging,

$$rV_u = \sqrt{\frac{2A(r - r_m)^B}{r^2(B + 1)} \left[ \left( V_{z,m} - \frac{A}{2}(r - r_m)^B \right) \frac{(2r_m^2 + 2r_m Br + B(B + 1)r^2)}{(B + 2)} \right] + k}$$

Or,

$$\boxed{V_u(r) = \sqrt{\frac{2A(r - r_m)^B}{r^2(B + 1)} \left[ \left( V_{z,m} - \frac{A}{2}(r - r_m)^B \right) \frac{(2r_m^2 + 2r_m Br + B(B + 1)r^2)}{(B + 2)} \right] + \frac{k}{r^2}}} \quad (3.2)$$

To find constant,  $k$ , let  $r = r_m$  and  $V_u(r) = V_{u,m}$  which is obtained from the meanline calculations and is dependent on alpha and  $V_{z,m}$ .

### C. Meanline Aerodynamics

Reproduced below are tables containing the aerodynamic values from the meanline design of all four blade designs. To clarify again, all three Hybrid Vortex design cases share the same leading edge design and thus, only requires the one set of aerodynamic values.

2% Span	LE	
	FV	HV
$\sigma_s =$	14.00	-9.98
$\alpha_{LE} =$	-24.48	-58.76
$\beta_{LE} =$	35.34	4.34
$v_{LE} =$	137.74	163.59
$v_{u,LE} =$	-57.07	-139.86
$v_{z,LE} =$	125.36	84.85
$U_{LE} =$	-145.95	-146.30
$w_{LE} =$	153.67	85.09
$w_{u,LE} =$	88.88	6.44
$M_{r,LE} =$	0.4495	0.2511

2% Span	TE			
	FV	HV #1	HV #2	HV #3
$\Delta\beta =$	42.67	28.63	45.70	31.30
$\alpha_{TE} =$	-57.60	-60.85	-65.77	-62.85
$\beta_{TE} =$	-7.33	-24.29	-41.36	-26.96
$v_{TE} =$	229.26	271.06	321.72	269.26
$v_{u,TE} =$	-193.57	-236.72	-293.37	-239.61
$v_{z,TE} =$	122.85	132.05	132.05	122.85
$U_{TE} =$	-177.77	-177.12	-177.12	-177.12
$w_{TE} =$	123.86	144.88	175.93	137.83
$w_{u,TE} =$	-15.80	-59.60	-116.25	-62.49
$M_{r,TE} =$	0.3515	0.4256	0.5307	0.40

25% Span	LE	
	FV	HV
$\sigma_s =$	38.66	27.87
$\alpha_{LE} =$	-18.83	-32.17
$\beta_{LE} =$	50.50	45.24
$v_{LE} =$	132.45	140.79
$v_{u,LE} =$	-42.75	-74.96
$v_{z,LE} =$	125.36	119.18
$U_{LE} =$	-194.83	-195.14
$w_{LE} =$	197.09	169.25
$w_{u,LE} =$	152.08	120.18
$M_{r,LE} =$	0.5766	0.4964

25% Span	TE			
	FV	HV #1	HV #2	HV #3
$\Delta\beta =$	23.69	34.74	41.78	33.98
$\alpha_{TE} =$	-51.96	-57.31	-59.29	-57.67
$\beta_{TE} =$	26.82	10.50	3.46	11.26
$v_{TE} =$	199.38	232.12	245.44	229.74
$v_{u,TE} =$	-157.03	-195.36	-211.01	-194.14
$v_{z,TE} =$	122.85	125.35	125.35	122.85
$U_{TE} =$	-219.13	-218.60	-218.60	-218.60
$w_{TE} =$	137.65	127.49	125.58	125.26
$w_{u,TE} =$	62.10	23.24	7.59	24.46
$M_{r,TE} =$	0.3907	0.3683	0.3648	0.36

50% Span	LE	
	FV	HV
$\sigma_s =$	53.56	48.83
$\alpha_{LE} =$	-15.00	-14.27
$\beta_{LE} =$	59.68	58.46
$v_{LE} =$	129.78	135.99
$v_{u,LE} =$	-33.59	-33.52
$v_{z,LE} =$	125.36	131.79
$U_{LE} =$	-247.97	-248.22
$w_{LE} =$	248.34	251.93
$w_{u,LE} =$	214.38	214.70
$M_{r,LE} =$	0.7265	0.7380

50% Span	TE			
	FV	HV #1	HV #2	HV #3
$\Delta\beta =$	12.24	19.25	15.93	18.55
$\alpha_{TE} =$	-46.68	-53.07	-50.87	-52.64
$\beta_{TE} =$	47.44	39.21	42.53	39.91
$v_{TE} =$	179.08	204.48	194.67	202.47
$v_{u,TE} =$	-130.30	-163.46	-151.01	-160.94
$v_{z,TE} =$	122.85	122.85	122.85	122.85
$U_{TE} =$	-264.09	-263.69	-263.69	-263.69
$w_{TE} =$	181.64	158.55	166.70	160.15
$w_{u,TE} =$	133.79	100.23	112.68	102.75
$M_{r,TE} =$	0.5155	0.4536	0.4754	0.46

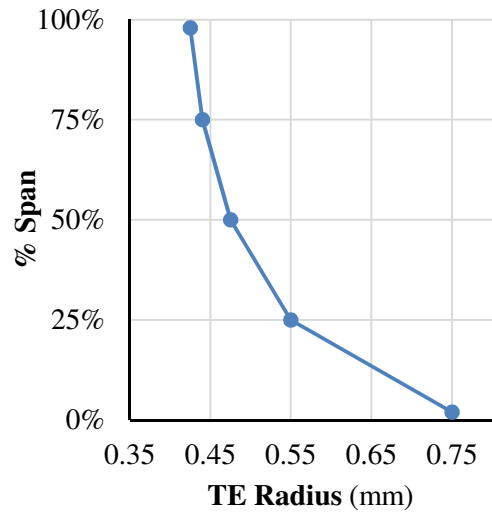
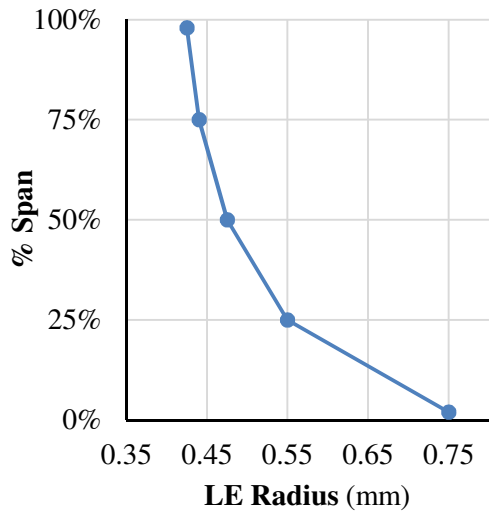
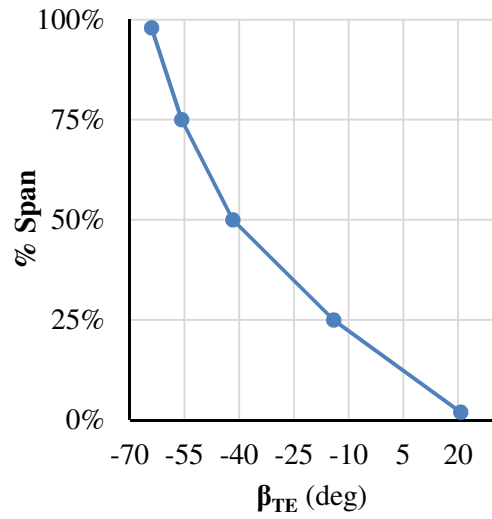
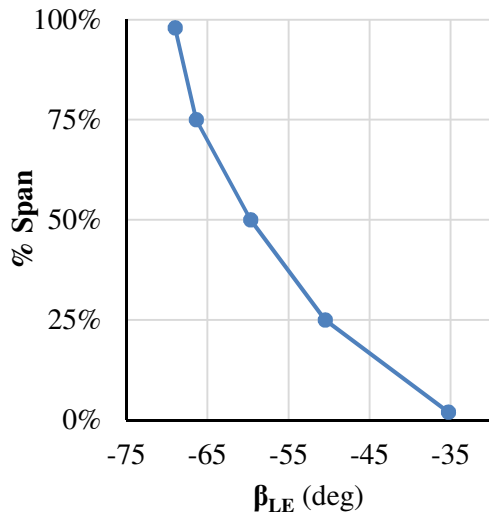
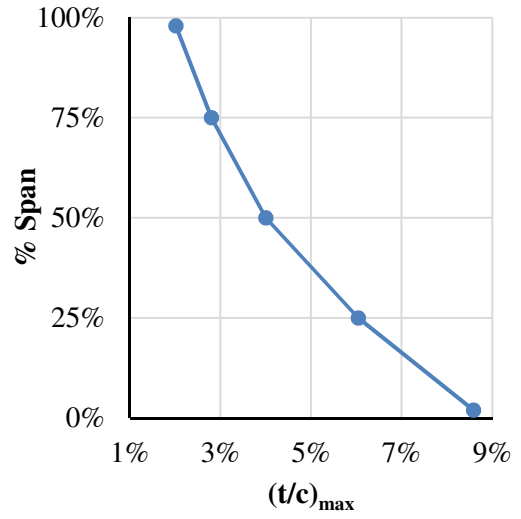
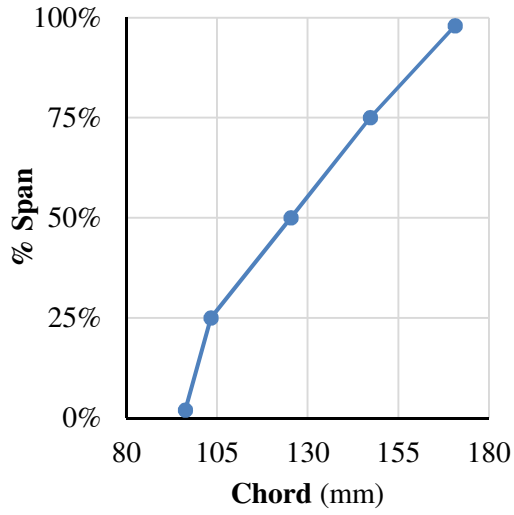
75% Span	LE	
	FV	HV
$\sigma_s =$	61.76	59.22
$\alpha_{LE} =$	-12.44	-12.70
$\beta_{LE} =$	65.37	64.20
$v_{LE} =$	128.37	134.62
$v_{u,LE} =$	-27.66	-29.59
$v_{z,LE} =$	125.36	131.33
$U_{LE} =$	-301.11	-301.31
$w_{LE} =$	300.81	301.79
$w_{u,LE} =$	273.45	271.72
$M_{r,LE} =$	0.8800	0.8838

75% Span	TE			
	FV	HV #1	HV #2	HV #3
$\Delta\beta =$	7.23	9.96	8.32	9.85
$\alpha_{TE} =$	-42.19	-49.56	-47.36	-48.21
$\beta_{TE} =$	58.14	54.24	55.88	54.36
$v_{TE} =$	165.80	185.81	177.92	184.34
$v_{u,TE} =$	-111.34	-141.42	-130.88	-137.44
$v_{z,TE} =$	122.85	120.52	120.52	122.85
$U_{TE} =$	-309.05	-308.78	-308.78	-308.78
$w_{TE} =$	232.77	206.24	214.88	210.83
$w_{u,TE} =$	197.71	167.36	177.89	171.34
$M_{r,TE} =$	0.6606	0.5865	0.6097	0.60

98% Span	LE	
	FV	HV
$\sigma_s =$	66.50	65.13
$\alpha_{LE} =$	-10.75	-19.46
$\beta_{LE} =$	68.98	67.66
$v_{LE} =$	127.60	133.26
$v_{u,LE} =$	-23.80	-44.39
$v_{z,LE} =$	125.36	125.65
$U_{LE} =$	-349.99	-350.14
$w_{LE} =$	349.45	330.56
$w_{u,LE} =$	326.20	305.75
$M_{r,LE} =$	1.0223	0.9678

98% Span	TE			
	FV	HV #1	HV #2	HV #3
$\Delta\beta =$	4.95	5.06	5.54	5.86
$\alpha_{TE} =$	-38.64	-48.67	-49.61	-44.60
$\beta_{TE} =$	64.03	62.60	62.12	61.80
$v_{TE} =$	157.28	172.99	176.33	172.55
$v_{u,TE} =$	-98.20	-129.89	-134.31	-121.16
$v_{z,TE} =$	122.85	114.25	114.25	122.85
$U_{TE} =$	-350.41	-350.26	-350.26	-350.26
$w_{TE} =$	280.54	248.22	244.31	259.95
$w_{u,TE} =$	252.21	220.36	215.95	229.09
$M_{r,TE} =$	0.7962	0.7033	0.6928	0.80

### D. Free Vortex Geometric Trends



## E. NASA GRAPE Sample Input

```
&grid1 jmax=300 kmax=60 ntetyp=3 nairf=5 nibdst=7 nobshp=7
jairf=121 jtebot=30 jtetop=271 norda=0 3 maxita= 0 3000 nout=4
dsi=8.41e-6 xle=0.0 xte=0.2716 xleft=-.1213 xright=.425 rcorn=0.0
&end
&grid2 nobcas=0 nle=40 nte=22 dsra=.49 dsle=.0004 dste=.0005
pitch=0.2425 yscl=1. xtfrac=1. dsobi=.002 dswex=.0051
aaai=0.45 bbbi=0.45 ccci=0.35 dddi=0.35 jwakex=1 kwakex=0 csmoo=1.
jcap=28
&end

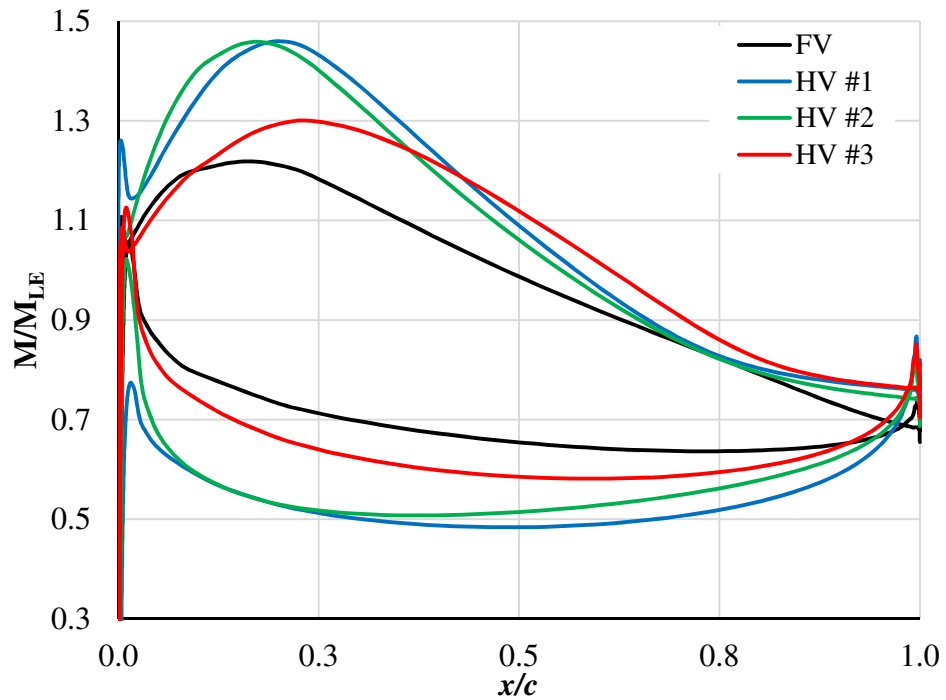
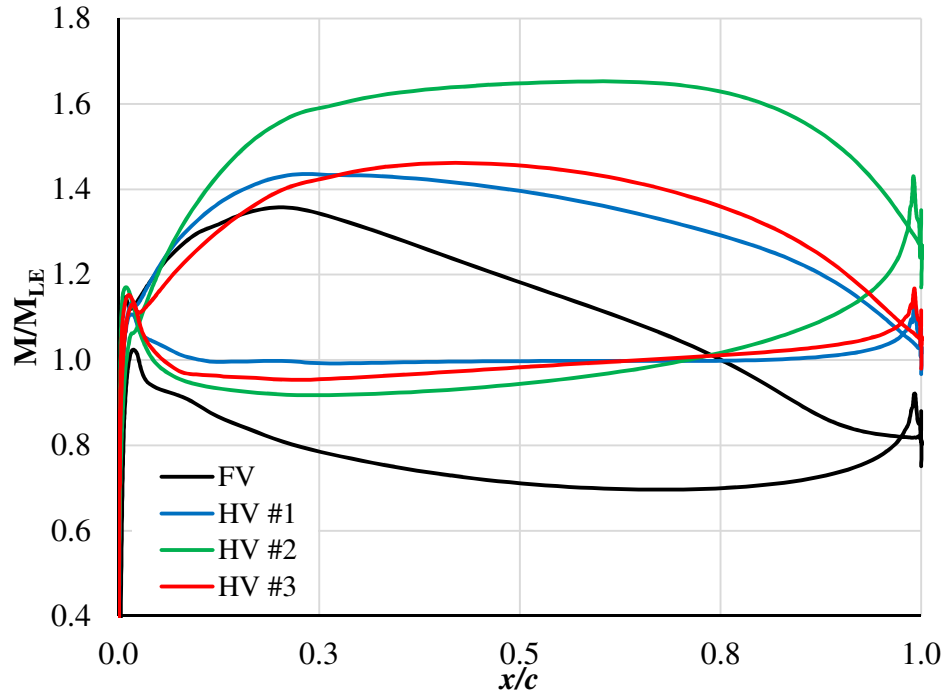
&grid3 airfx=
9.449174E-01 9.448845E-01 9.448103E-01 9.446964E-01 9.445454E-01
9.443609E-01 9.441471E-01 9.439087E-01 9.436512E-01 9.433804E-01
9.431025E-01 9.418931E-01 9.398222E-01 9.369034E-01 9.331562E-01
9.286064E-01 9.232866E-01 9.172349E-01 9.104908E-01 9.030984E-01
...
(some lines excluded for conciseness)
...
9.286697E-01 9.332589E-01 9.370287E-01 9.399594E-01 9.420360E-01
9.432476E-01 9.435243E-01 9.437904E-01 9.440397E-01 9.442666E-01
9.444659E-01 9.446330E-01 9.447643E-01 9.448566E-01 9.449080E-01
9.449174E-01
airfy=
2.321169E-02 2.292413E-02 2.264467E-02 2.237964E-02 2.213503E-02
2.191637E-02 2.172857E-02 2.157587E-02 2.146170E-02 2.138862E-02
2.135827E-02 2.131909E-02 2.124426E-02 2.112237E-02 2.093848E-02
2.067348E-02 2.030444E-02 1.980595E-02 1.915002E-02 1.830714E-02
...
(some lines excluded for conciseness)
...
2.640675E-02 2.607052E-02 2.576202E-02 2.550231E-02 2.530745E-02
2.518954E-02 2.514026E-02 2.504854E-02 2.491649E-02 2.474713E-02
2.454435E-02 2.431278E-02 2.405773E-02 2.378501E-02 2.350084E-02
2.321169E-02
&end
```

## F. NASA RVCQ3D Sample Input

```
'25% Span - Hybrid Vortex #3'  
&nl1 m=300 n=60 mtl=30 mil=137 &end  
&nl2 nstg=4 ivdt=1 irs=1 eps=1.0 ndis=2 cfl=5.6 avisc2=0 avisc4=.5  
  ipc=0 pck=.1 refm=0.7 hcuspk=.10 ausmk=0.6 icdup=0 &end  
&nl3 ibcinu=1 ibcinv=2 ibcex=1 itmax=6000 iresti=0 iresto=1 ires=10  
  icrnt=50 ixrm=0 ibcext0=1 &end  
&nl4 amle=0.4129 alle=-32.2 bete=11.26 prat=1.06 p0in=1. t0in=1. g=1.4 &end  
&nl5 ilt=5 jedge=35 renr=6.74e6 prnr=.7 tw=0. vispwr=.667  
  itur=2 cmutm=14. &end  
&nl6 omega=-0.663 nblade=22 nmn=22 &end  
&nl7 tintens=.01 tlength=2.29e-4 hrough=0. &end  
-0.1213 -0.0970 -0.0728 -0.0485 -0.0243 0.0000 0.0251 0.0502 0.0753  
0.1004 0.1255 0.1505 0.1756 0.2007 0.2258 0.2509 0.2760 0.3295  
0.3829 0.4364 0.4898 0.5433  
0.8584 0.8522 0.8487 0.8481 0.8502 0.8550 0.8630 0.8730 0.8827  
0.8919 0.9007 0.9092 0.9172 0.9247 0.9319 0.9387 0.9450 0.9571  
0.9674 0.9757 0.9822 0.9868  
1.0000 1.0053 1.0082 1.0088 1.0070 1.0029 0.9961 0.9874 0.9788  
0.9704 0.9622 0.9543 0.9467 0.9393 0.9322 0.9255 0.9164 0.9040  
0.8933 0.8844 0.8774 0.8749
```



## G. 2D Blade Design



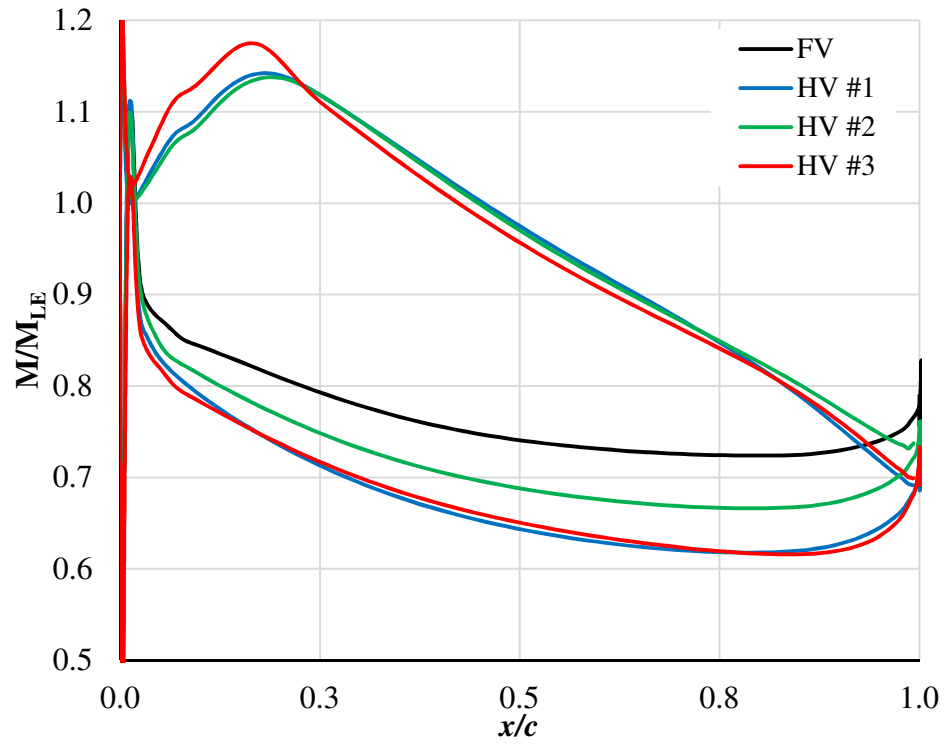


Figure G.3 Mach distribution for 75% span, all four designs.

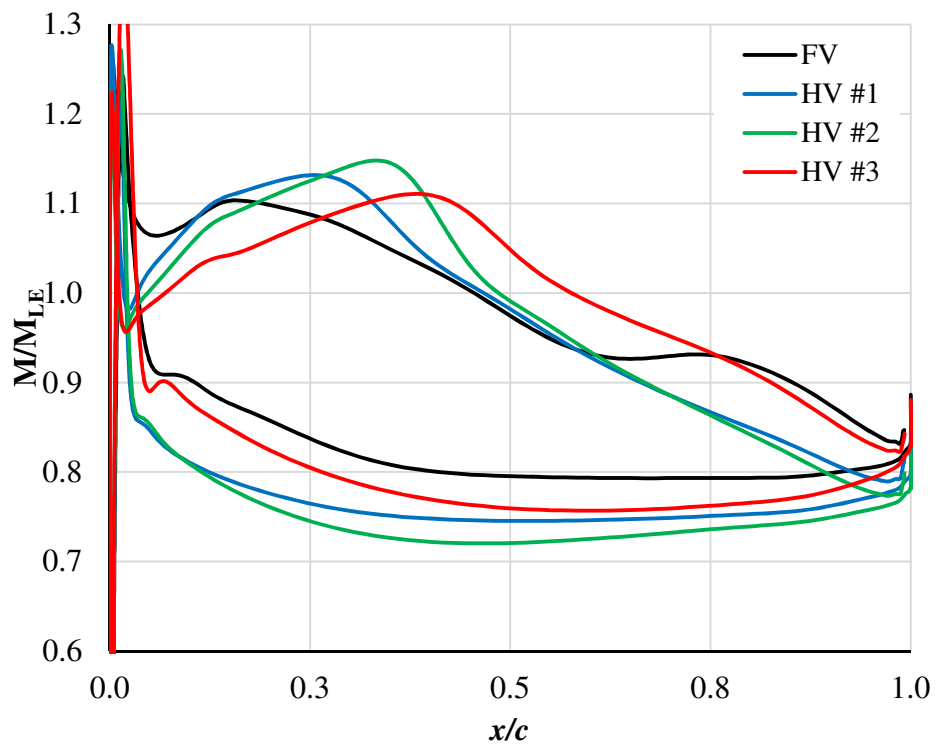


Figure G.4 Mach distribution for 98% span, all four designs.

## 2D Section Comparisons

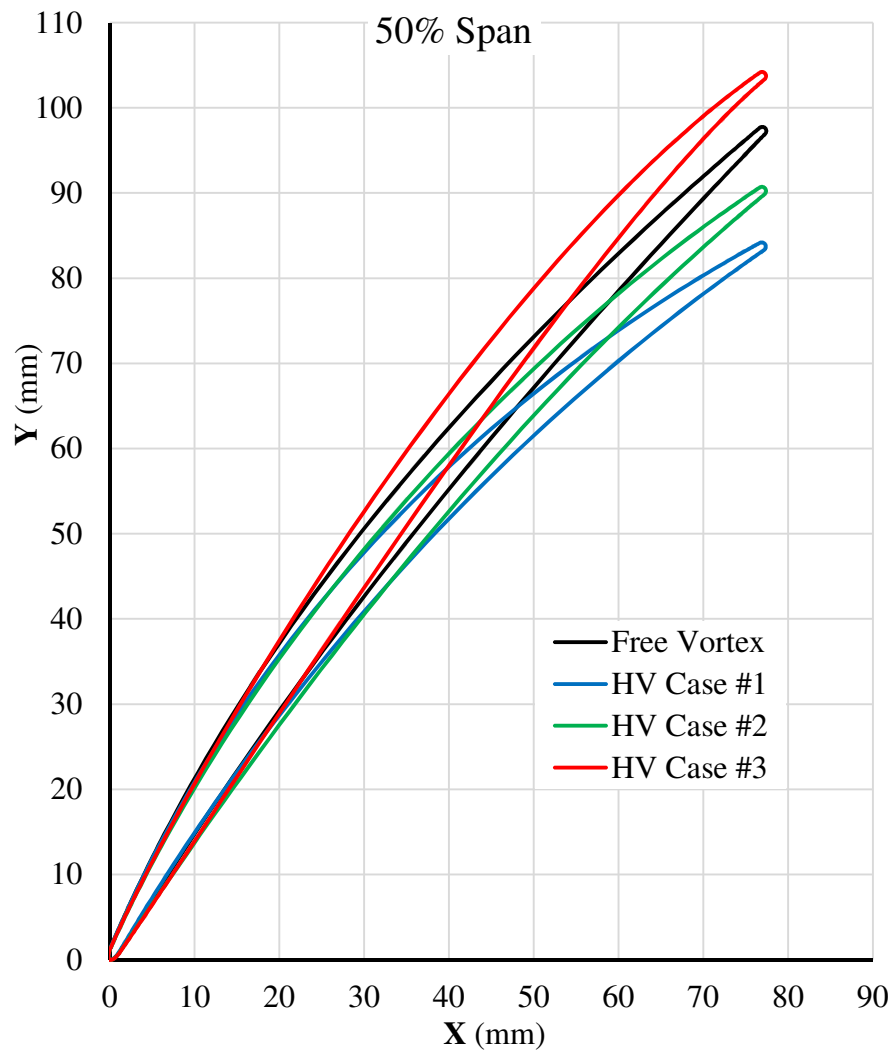


Figure G.5 Airfoil sections at 50% span.

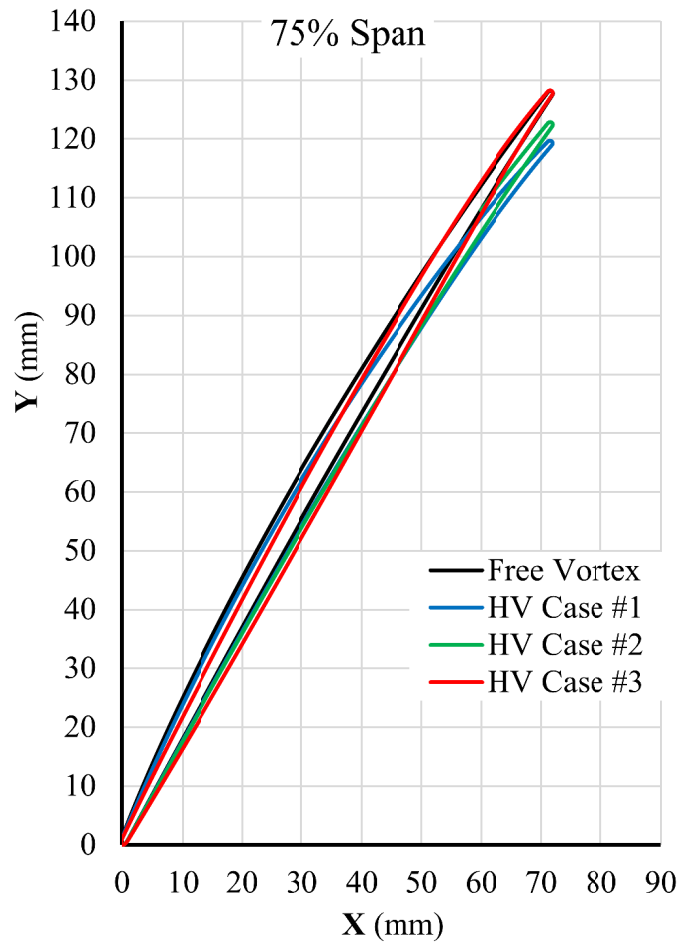


Figure G.6 Airfoil sections at 75% span.

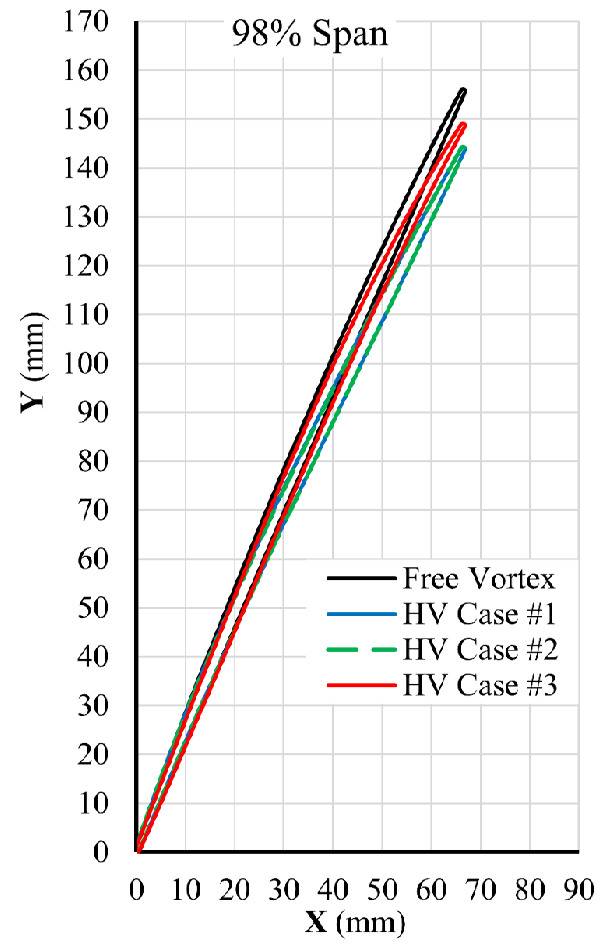
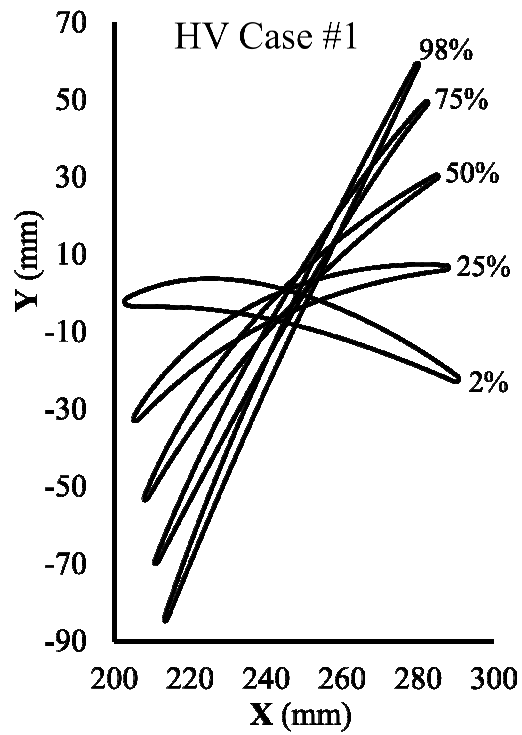
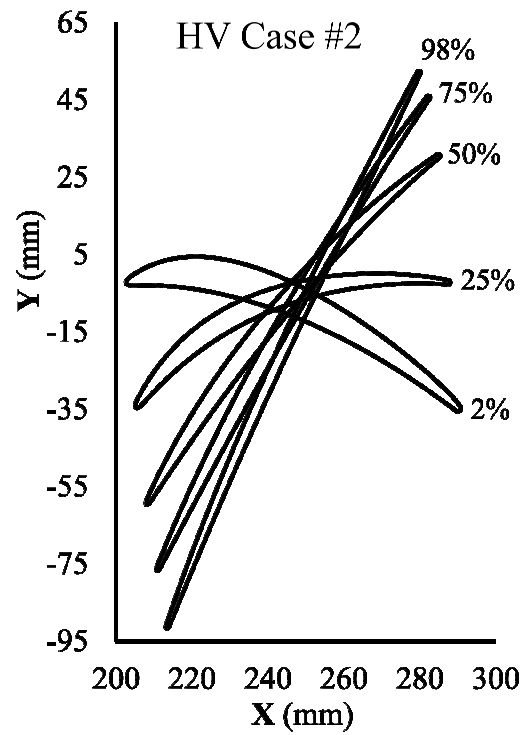


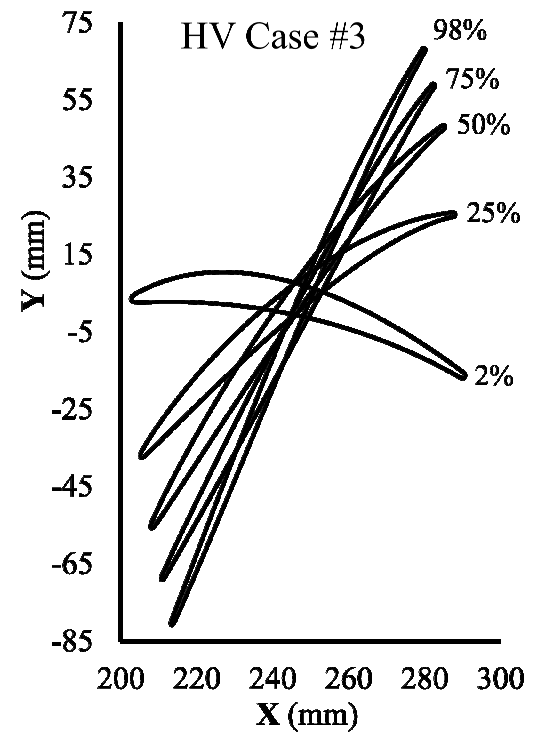
Figure G.7 Airfoil sections at 98% span.



(a)



(b)



(c)

Figure G.8 Hybrid Vortex 2D sections on their stacking lines for design Case #1 (a), #2 (b), and #3 (c).

## H. Sample CFX® Inlet Velocity Profile File

The following file is a sample of the inlet velocity direction profile used for the boundary conditions in the 3D simulations. The file is in a ‘.csv’ format and gives the location of the boundary condition along with the unit vector magnitude of each component for the velocity direction.

[Name]

R1 Inlet

[Spatial Fields]

x            y            z

[Data]

x [ m ]	y [ m ]	z [ m ]	Velocity Direction in Stn Frame u	Velocity Direction in Stn Frame v	Velocity Direction in Stn Frame w
0.1889	0.0000	0.1875	0.0000	0.8736	0.4867
0.1946	0.0000	0.1875	0.0000	0.8530	0.5219
0.2002	0.0000	0.1875	0.0000	0.8308	0.5565
0.2058	0.0000	0.1875	0.0000	0.8071	0.5904
0.2114	0.0000	0.1875	0.0000	0.7820	0.6233
0.2170	0.0000	0.1875	0.0000	0.7556	0.6551
0.2227	0.0000	0.1875	0.0000	0.7280	0.6856
0.2283	0.0000	0.1875	0.0000	0.6993	0.7148
			...		
			<i>(some lines excluded for conciseness)</i>		
			...		
0.4250	0.0000	0.1875	0.0000	0.2412	0.9705
0.4306	0.0000	0.1875	0.0000	0.2499	0.9683
0.4363	0.0000	0.1875	0.0000	0.2601	0.9656
0.4419	0.0000	0.1875	0.0000	0.2718	0.9624
0.4475	0.0000	0.1875	0.0000	0.2849	0.9585
0.4531	0.0000	0.1875	0.0000	0.2996	0.9541
0.4588	0.0000	0.1875	0.0000	0.3156	0.9489
0.4644	0.0000	0.1875	0.0000	0.3331	0.9429
0.4700	0.0000	0.1875	0.0000	0.3518	0.9361

## I. 3D Meshing and Independency

ANSYS  
R16.0  
Academic

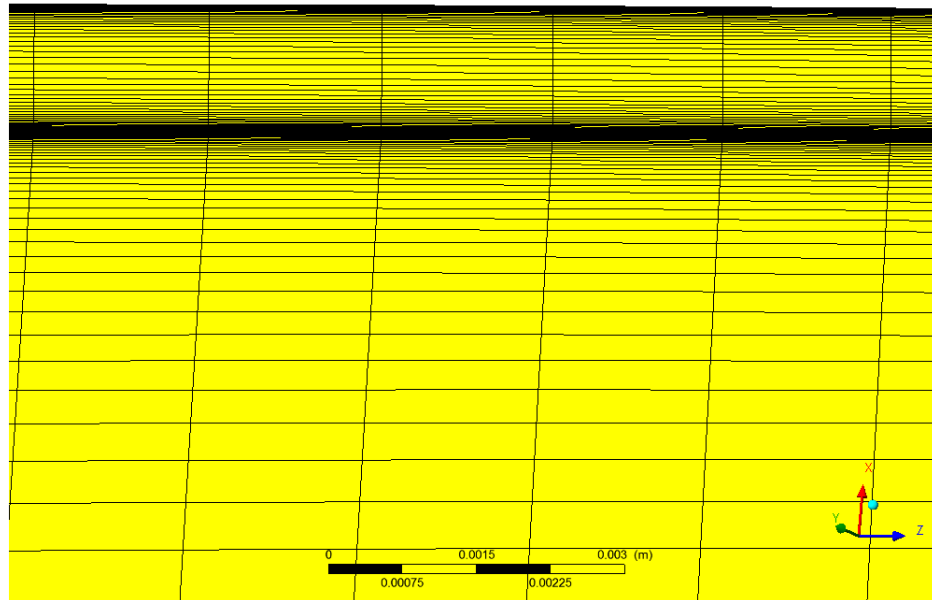


Figure I.1 Tip gap refinement for the medium mesh (2.5M elements).

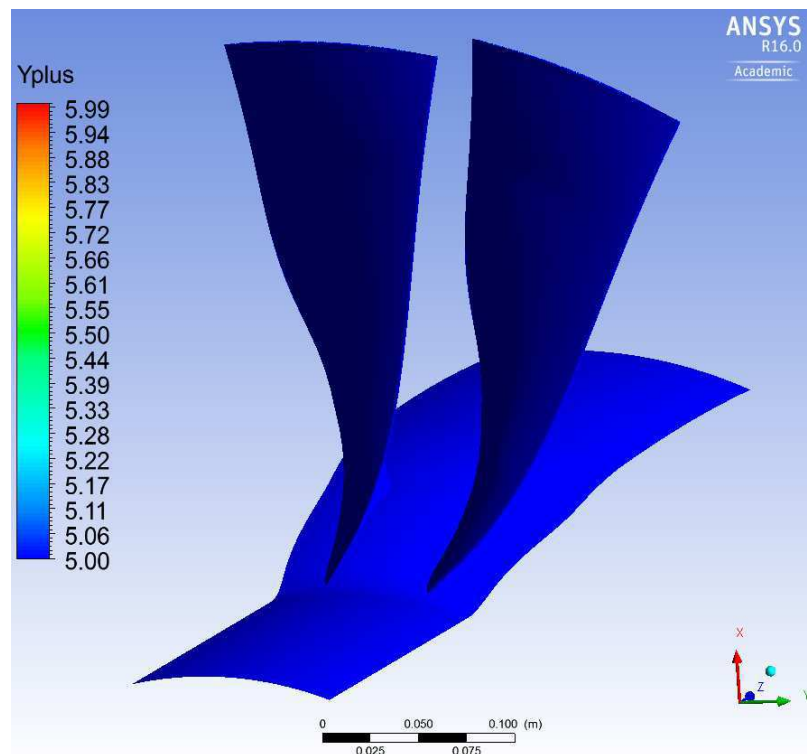


Figure I.2 Y+ contour of the medium mesh (2.5M elements).

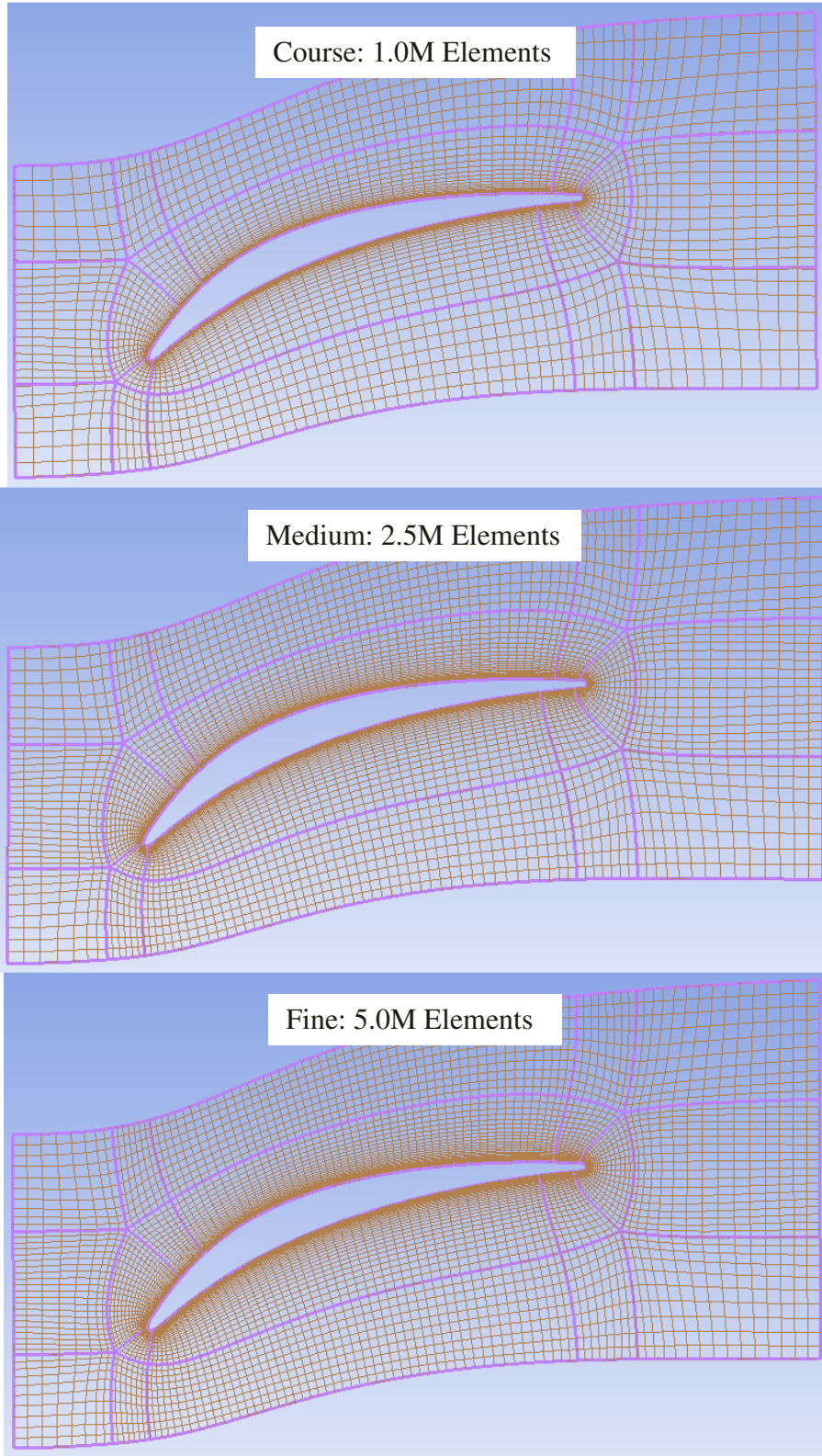


Figure I.3 Sample of mesh refinements used for independence study.



## J. Hybrid Vortex 3D Design

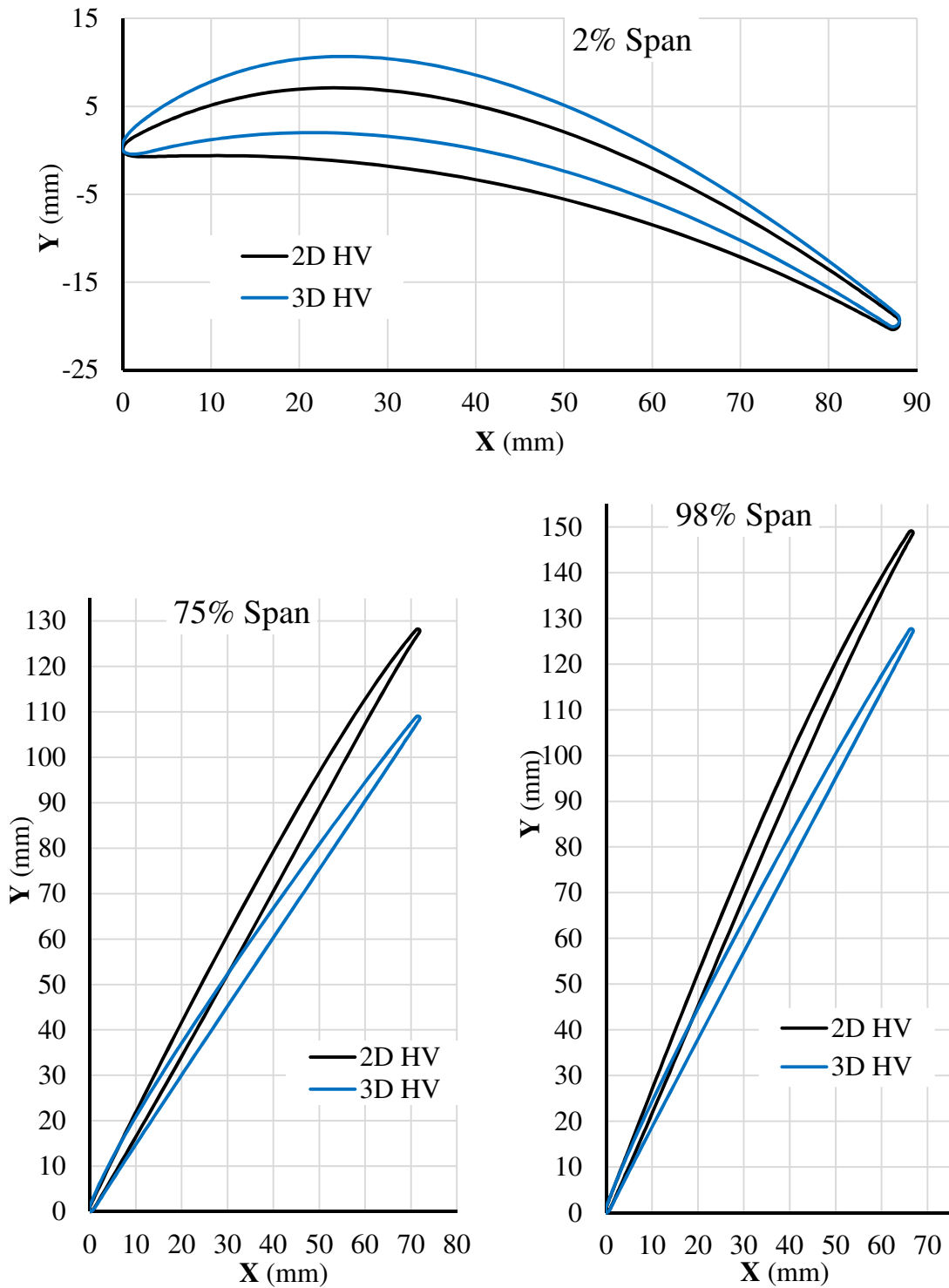


Figure J.1 Airfoil comparison between the 2D and 3D designed Hybrid Vortex blades.

## K. BladeGen™-to-RVCQ3D flow automation

### NAME

b2r – BladeGen™ to RVCQ3D flow automation

### SYNOPSIS

b2r [options] <curve file>

### DESCRIPTION

b2r is a Perl script which automates various processing steps to support 2D blade design. It accepts as input a “curve” file which has been generated by the ANSYS® BladeGen™ program, and for one or more selected profiles contained in this file, b2r:

- Creates an input file suitable for use with the NASA GRAPE program, based on template file(s) and blade geometry extracted from the BladeGen™ curve input file.
- Runs the NASA GRAPE program
- Extracts the output from GRAPE, and based again on template file(s) converts it into a form suitable as input to the NASA RVCQ3D program.
- Runs the NASA RVCQ3D program
- Extracts the output from the RVCQ3D program
- Plots the results both visually and into a file

### OPTIONS

*-e | --enable <profiles>*

*<profiles>* is a text string indicating which blade profile(s) to process, in the order that they appear in the BladeGen™ input file. Any of the characters “YyTt1” indicate that the corresponding profile is to be processed, any other character (typically “NnFf0”) indicates that the profile is not to be processed. The first character in *<profiles>* corresponds to the first profile in the BladeGen™ “curve” input file, the second character corresponds to the second profile etc. The corresponding profile percent span is read from the BladeGen input file.

Examples:

*-e TTFFF*                      *Process the first two profiles*

*-e 00100*                      *Process only the third profile*

In BladeGen™ “curve” files used for this thesis, there are five profiles, corresponding to 2%, 25%, 50%, 75% and 98% span.

*-p | --profile <percent>*

Search the BladeGen input file for a profile with a percent span of *<percent>*, and process that entry.

*-g | --grape <path>*

*<path>* is the full path to the NASA GRAPE executable.

The default path is operating system dependent. If the detected environment is native Windows, then the default path is:

nasa\NASA\_GRAPE\src\grape

Otherwise, the default path is:

nasa/NASA\_GRAPE/src/grape

*-r | --rvcq3d <path>*

<path> is the full path to the NASA RVCQ3D executable.  
The default path is operating system dependent. If the detected environment is native Windows, then the default path is:

nasa\NASA\_RVCQ3D\rvcq3d\_403\src\rvcq3d

Otherwise, the default path is:

nasa/NASA\_RVCQ3D/rvcq3d\_403/src/rvcq3d

*-d | --debug*

Print debug information

*-h | --help*

Print usage information

*-v | --verbose*

Print more descriptive information as processing occurs

## FILES

There are a large number of user provided and program generated files used in the processing that b2r performs, and a file naming convention is used to bring some order to this chaos. All file names are derived from the name of the BladeGen™ generated “curve” file, which represents the primary blade geometry input file for the system. If the BladeGen™ input file is “<name>.curve”, then the following file(s) may exist or be generated:

<name>\_PP.gtpl A grape template file, specific to the PP percent profile  
<name>.gtpl A grape template file, used if no <name>\_PP.gtpl file exists

<name>\_PP.gin A derived grape input file for the profile PP percent  
<name>\_PP.gout Grape output file, specific to the profile PP percent  
<name>\_PP.grid Saved "fort.1" file, specific to the profile PP percent

<name>\_PP.rtpl An rvcq3d template file, specific to the PP percent profile  
<name>.rtpl An rvcq3d template file, used if no <name>\_PP.rtpl file exists  
<name>\_PP.rin A derived rvcq3d input file  
<name>\_PP.rout The rvcq3d output file for the profile PP percent

<name>\_PP.pressure X-Y data file for the pressure curve for the PP profile  
<name>\_PP.suction X-Y data file for the suction curve for the PP profile  
<name>\_PP.gpl Gnuplot command file to create the curves for the PP profile  
<name>\_PP.png Graphical output file from Gnuplot for the PP profile

where the letters “PP” in the above names correspond to the profile percent.

In addition, a working directory called “<name>” will be created, if it does not already exist, to contain all generated files and results for a given run, and a directory called “plots” will be created under this level to contain generated plot files.

The user must provide, at minimum, a master template file for the NASA GRAPE program, and a master template file for the NASA RVCQ3D file. The meaning of most terms in these files can be gleaned from the associated NASA documentation.

The user provided master GRAPE template file, “grape.gtpl” might typically contain:

```
&grid1 jmax=200 kmax=35 ntetyp=3 nairf=5 nibdst=7 nobshp=7  
jairf=201 jtebot=25 jtetop=176 norda=0 3 maxita= 0 1500 nout=4
```

```

dsi=5.0e-5 xle=0. xte=0.26 xleft=-.11 xright= 0.4 rcorn=0.02
&end
&grid2 nobcas=0 nle=14 nte=8 dsra=.49 dsle=.0006 dste=.005
pitch=0.1974 yscl=1. xtfrac=1. dsobi=.004 dswex=.0055
aaai=0.70 bbbi=0.70 ccci=0.35 dddi=0.35 jwakex=1 kwakex=1 csmoo=1
jcap=8
&end

```

The user provided master RVCQ3D template file, “rvcq3d.rtpl” might typically contain:

```

'Subsonic compressor cascade'
&nl1 m=MMM n=NNN mtl=xxxMTLxxx mil=xxxMILxxx &end
&nl2 nstg=4 ivdt=1 irs=1 eps=1.0 ndis=2 cfl=5.6 avisc2=1. avisc4=.5
ipc=0 pck=.15 refm=.9 hcuspk=.10 ausmk=0.6 icdup=0 &end
&nl3 ibcin=1 ibcex=3 itmax=2500 iresti=0 iresto=1 ires=1
icrnt=50 ixrm=0 ibcext0=1 &end
&nl4 amle=.38 alle=13. bete=26. prat=1.02 p0in=1. t0in=1. g=1.4 &end
&nl5 ilt=5 jedge=20 renr=5.5417e5 prnr=.7 tw=0. vispwr=.667
itur=2 cmutm=14. &end
&nl6 omega=-0.4795 nblade=1 nmn=0 &end
&nl7 tintens=.01 tlength=2.e-4 hrough=4. &end

```

In each case, users may provide template files for a specific profile percentage, which override the use of the above master template files. For example, if a the input BladeGen™ file is called “2g1.curve”, and there exists a file called “2g1\_50.gtpl”, then for the fifty percent profile, this file will be used as the template for b2r to construct an input file for the GRAPE program, rather than the master “grape.gtpl” template. The odd looking strings in the above RVCQ3D template file are reserved for values which b2r derives from the grape output. Refer to the b2r source code for more details on this matter.

## **PLOTTING**

Apart from creating output result files, b2r will plot the results in the form of pressure and suction curves, both to the user’s screen and to a file. The gnuplot program is used internally to make these graphics, and must be available. If the native environment is MS Windows, the crude Microsoft Paint program is launched to view the created “png” plot file. Otherwise, in more sensible environments, gnuplot is used to launch an X11 window directly. In all cases a saved “png” graphics file is created.

## **BUGS**

There are no options to control the plotting, and there should be. If the Y axis scale needs to be changed, the user has to change it directly in the b2r code b2r tries to advise the user if either of the NASA programs produces NaN’s in their output. The behavior of these underlying programs can be confounding when bad input parameters lead to numerical implosions, and the user’s only choice when this happens is to go back to fundamentals and examine the input and output of each program individually.

## L. CFX<sup>®</sup> Definition File Generation Code

### NAME

mkdef – Make CFX<sup>®</sup> input file(s) and driver script from a template file

### SYNOPSIS

mkdef [options] <relative pressure ratios>

### DESCRIPTION

mkdef is a bash shell script which automates the process of performing multiple CFD runs in ANSYS<sup>®</sup> CFX<sup>®</sup>. It can derive CFX<sup>®</sup> input files (“def” files) from a master template file, adjusting parameters for different runs, and create a variety of different script types that can be executed to perform those runs on different systems. Batch script files for the SLURM and PBS queues on Rigel can be created, or scripts that can be directly executed on Linux or Windows systems.

The user creates a master “template” file, usually using ANSYS<sup>®</sup> CFX<sup>®</sup>-Pre, and a naming convention is used to help mkdef create derivatives, in the form “blade-mesh-speed-template.def”. A typical template file might be named:

*fv-2500000-100-template.def*

where “fv” is an arbitrary user specified name that refers to the blade design, “2500000” is an arbitrary user specified identifier for the blade version, which usually contains a count of the mesh nodes, “100” is the nominal rpm in percent for the template file. The “-” separators are mandatory, as is the string “template” and the file type “.def”. Internally, the template file must have a relative pressure set to 111.1234 kPa in order to provide a match point for mkdef to derive modified versions.

Derivative files are created based on a list of relative pressure ratios given on the command line. For example,

*mkdef 110 112 114 116*

will create four def files, whose names are in the form blade-mesh-speed-pressure-cfxruntype.def, so in the case of the previously cited template file example, the derived files for the above command would be:

*fv-250000-100-110-auto.def*  
*fv-250000-100-112-auto.def*  
*fv-250000-100-114-auto.def*  
*fv-250000-100-116-auto.def*

Each derived file is a valid ANSYS<sup>®</sup> CFX<sup>®</sup> input file, with all other conditions the same as the template file. The “auto” in the above filenames refers to the default simulation type of automatic timescale. In some cases, following up an automatic timescale run with the use of “local timescale” and/or “physical timescale” CFX<sup>®</sup> options is required to reduce oscillating residuals to an acceptable level. Mkdef allows specification of these

with the following syntax:

*RRR@A,L,P*

Where RRR is the relative pressure in kPa, and numeric A, L, P are the number of iterations to perform in auto, local and physical timescale respectively. A “def” file will be created for each case, and command scripts will automatically use CFX<sup>®</sup>’s “continue from” option to cascade the two or three separate runs. When there are multiple pressure settings, a specification of this type will alter the defaults and carry on through each successive run. For example:

*mkdef 110@2000,500,1000 112*

Will create six “def” files, as follows:

*fv-250000-100-110-auto.def*  
*fv-250000-100-110-local.def*  
*fv-250000-100-110-physical.def*  
*fv-250000-100-112-auto.def*  
*fv-250000-100-112-local.def*  
*fv-250000-100-112-physical.def*

Other examples of legal syntax:

*mkdef 110@3000 112@2000,500*

One def file is created for 3000 iterations in auto timescale @ 110 kPa relative pressure, and two def files are created for relative pressure 112 kPa, one auto timescale at 2000 iterations, followed by one local timescale at 500 iterations.

*mkdef 115.5@2000,,1000*

Two def files are created for relative pressure of 115.5 kPa, one auto timescale at 2000 iterations, one physical timescale at 1000 iterations.

mkdef runs on any Linux system, or under the Cygwin system on Windows. mkdef can be run on the head node of Rigel, if the user first performs a “module load” command for the appropriate CFX<sup>®</sup> release (since mkdef uses the cfx5cmds program).

mkdef has various options to control more complex behaviors, as described in the following section.

## OPTIONS

- c Cascade results. Used in conjunction with the -w, -P or -S flags, when multiple simulation runs are created in a command script. Each simulation result file will be used as initial conditions for the subsequent run.
- f FAKE run, just show what files would be created.

-h Print a usage message.

-i *<file>*

Normally, an initial conditions file will be sensed automatically by the presence of a result file beginning with the string “init” in the local directory. A user may instead manually specify the initial conditions file to be used for the first (or every if no `-c` flag present) CFX<sup>®</sup> run using the option.

-l *<local timescale>*

If CFX<sup>®</sup> input files operating in local timescale mode are to be created, the default local timescale value is 5. This flag allows the user to specify a different local timescale.

-n *<num>*

Make generated command file use *<num>* local CPU's, rather than the default value which is the number of logical CPU's sensed on the current host system. This flag does not affect batch scripts created for the PBS or SLURM queues on Rigel. For other systems, this flag for example allows a batch script to be created on a laptop, and then transferred to the gas turbine lab cluster which has more CPU's available.

-p *<physical timescale>*

If CFX<sup>®</sup> input files operating in physical timescale mode are to be created, the default physical timescale is 0.0001 seconds. This option allows specification of a different physical timescale to be used.

-s *<speed>*

Create def files for a different rpm percentage than the template file (assumed to be 100%). For example “-s 115” would cause all created def files to correspond to 115% rpm.

-w *<file>*

Create a simple script file, which contains CFX<sup>®</sup> command line commands to perform all generated runs. If the filename specified ends in “.bat” or “.cmd” (case insensitive), then the generated script will be Windows BATCH script, and CFX<sup>®</sup> pathnames will be absolute. Otherwise, the generated script will be a Linux bash script.

-P *<file>*

Create a PBS batch script, suitable for queuing to the PBS system on Rigel. The default PBS header information is built into the mkdef script, and the only way to modify it is to edit the script directly. The default is:

```
#!/bin/bash

#PBS -l walltime=24:00:00
#PBS -l nodes=32
#PBS -N ${write_file_base}
```

```

#PBS -M portd@my.erau.edu
#PBS -m ae

#PBS -l mem=5000mb
#PBS -e `pwd`/pbserr
#PBS -o `pwd`/pbsout

module load ANSYS_inc/CFX/v162

```

and the user would obviously want to change at least the E-mail address. The script also contains commands which derive a suitable NODEFILE, and a string variable that can be passed to the cfx5solve command to specify the number of CPU's to use.

### -S <file>

Create a SLURM batch script, suitable for queuing to the SLURM batch system on Rigel. The default PBS header information is built into the mkdef script, and the only way to modify it is to edit the script directly. The default is:

```

#!/bin/bash

#SBATCH --job-name      ${write_file_base}
#SBATCH --account      portd                # Project
account
#SBATCH --time         24:00:00            # wall time
#SBATCH --ntasks      4                   # number of
tasks
#SBATCH --cpus-per-task 28
#SBATCH --mem-per-cpu 7G                  # memory/cpu
#SBATCH --output      ${write_file_base}_%j.out # Include the
job ID in the names of the
#SBATCH --error       ${write_file_base}_%j.err # output and
error files

cpus_per_node=28

threads=`srun hostname | sed -e ":a; \${!N;
s/\n/\*\"$cpus_per_node,/; ta" | sed -e
"s/\$/\*\"$cpus_per_node/"`
echo "Threads: \${threads}"

module load ANSYS_inc/CFX/v162

```

and the user would obviously want to change at least the project account name. The threads term above derives a suitable string for passing to the cfx5solve command to specify the distributed parallel CPU node(s) to use, and how many CPU's on each node. Modify this at your own peril.

Typically, only one of the -w, -P or -S flags would be used at any one time.

### FILES

The following files will be recognized by mkdef, and used if present in the local directory:



- Any file ending with the string “template.def”. If such a file is present, there can be only one and it must be in the form “blade-mesh-speed-template.def” as described previously.
- Any file beginning with the string “init” and ending with the string “.res”. If present, there can only be one and it will be used as the initial values file in any generated cfx5solve command, unless the user has over-ridden this feature by specifying the `-i` option.

mkdef will create as many “.def” files as the user specifies, together with a script file containing the CFX<sup>®</sup> commands for execution of these files.

## EXAMPLES

From the usage message printed by “mkdef -h”

Relative pressure setting examples

110	110 kPa
110 114.5	110 and 114.5 kPa
112@1000,750,500	112 kPa, with iteration counts of: 1000 in Autoscale mode 750 in Local timescale mode 500 in Physical scale mode
112@1000,0,500	Same as above, but no Local mode created/run
112@500,0,0 114	Autoscale only, for both 112 and 114 kPa
all	Generate def files for all the built-in cases

Example - Make def's and a slurm script:

```
mkdef -s 85 -c -S slurm.sh 118 119@1000 120
```

Makes 3 sets of def files, for 118, 119 and 120 kPa relative pressure, speed 85%, cascade results, create script "slurm.sh" for running in the slurm queue. The iteration count in the template file will be used for 118, 1000 iterations will be used for 119 and 120, auto-scale only.

Example - make def's and a batch script to run on the cluster:

```
mkdef -s 115 -n 16 -c -w run.bat 113@1000,500,0 114 115
```

Makes three sets of def files, for 113, 114 and 115 kPa relative pressure, speed 115%, 16 logical cpu's, cascade results, create command file "run.bat" for windows system. Runs are auto timescale for 1000 iterations, local timescale for 500 iterations, and no physical timescale run.

## BUGS

There should be command line arguments or environment variable options to allow specifying PBS or SLURM parameters, rather than requiring a user to edit these within the script itself.

mkdef -h to print a usage message won't work unless there is a template file present.